INFLUENCE OF BUILDING NEIGHBORS ON WIND FLOW AROUND A TALL BUILDING

BY

EJIRO COLLINS MOWARIN

A THESIS SUBMITTED IN PARTIAL FULFILMENT OF THE REQUIREMENTS FOR THE DEGREE OF MASTER OF SCIENCE

DEPARTMENT OF MECHANICAL ENGINEERING

LAKEHEAD UNIVERSITY

ABSTRACT

This thesis focuses on how building neighbors influence wind flow around a tall building. The wake dynamics and flow structures around a tall building are first explored using Large Eddy Simulations (LES). Following this, wake topology, flow structures, and vortical structures are investigated when a small building is placed downstream and upstream of a tall building. The wake and flow structures formed from the building neighbors' effects around the tall building were compared with the wake features and flow structures observed for the single tall building case.

The study of the wake was first investigated when a building neighbor (small building) was present downstream of a tall building. The influence a small building has on wind flow around the tall building was investigated by examining how wake and flow structures change when a small building was introduced. A weaker downwash flow shown by the decrease in vorticity was observed as opposed to when the tall building was isolated. This is primarily due to the presence of the small building downstream which subsequently reduced the wake effects from the tall building. Pedestrians will therefore experience better comfort at the wake region as opposed to when the tall building was isolated. Different flow structures were observed. First, a reverse-c shaped type of vortex was formed at the near wake which develops into hairpin type of vortices at the far wake. When upwash, downwash, and shear layers interact, hairpin vortices form, creating an increase in wake instabilities. A horseshoe vortex forms in the wake, with its legs extending into the wake, interacting with the wake structure formed behind the buildings and having an immediate effect on wake dynamics. At the windward face of the small building, which lies in the aerodynamic wake of the tall building, the mean pressure coefficient decreased even more, reaching $\overline{C_p} \approx 0.07$. The progressive decrease in mean pressure coefficient (82.5%) shows how the mean wind load reduces downstream due to the presence of the small building downstream. This further shows how aerodynamic wake effects decrease considerably more quickly.

Wake dynamics and flow structures were further investigated to study the influence of building neighbors on a tall building by considering when a small building is upstream of the tall building. Similar flow features and wake flow structures from the case when the small building was upstream of the tall building were observed. The upwash flow was significantly stronger than in the single tall building and small building downstream cases. It was observed that the small

building upstream was unable to dampen the strong turbulent flow in the tall building's leeward direction. Because of the suppressing effects of the flow separation from the small building, a strong recirculation zone was formed. This zone produces unfavorable wind conditions for pedestrians in this region at the ground level in this area (i.e., interface between the small and tall building). Effects of vortex shedding was much weaker on the windward face of the small building which led to a drop in mean streamwise velocity on the windward face of the tall building. Due to interference effects of the small building's windward walls, the mean streamwise velocity at the interface between the two building decreases. Wind flow towards the tall building was thereby shielded by the small building upstream, resulting in a minimal drop in the mean pressure coefficient (35.5%) surrounding the tall building's walls. The change in $\overline{C_p}$ on the front wall of the tall building downstream is caused by the wake created behind the first building (small building upstream).

ACKNOWLEDGEMENTS

My heartfelt gratitude goes to God Almighty who led me this far and made this research a success.

I would like to thank my supervisor, Dr. Ali Tarokh for his guidance during this research and for giving me the opportunity to work in his research group. My sincere gratitude goes to him for patiently guiding me up the Computational Fluid Dynamics ladder. I would like to extend my gratitude to Arash Zargar for his scientific pieces of advice and support during this research.

My profound gratitude goes to my beloved family and my parents (Dr. & Mrs. Mowarin) for their love, support, and prayers towards making this research work a success. I also extend my gratitude to my sister, Eguono Mowarin and my friends in Canada for their support and encouragement during this research.

Contents

List of Tables

List of Figures

LIST OF ABBREVIATIONS, SYMBOLS AND NOMENCLATURE

ρ	density of the fluid/air density
u	velocity scale
c	characteristic length scale
μ	fluid dynamic viscosity
υ	kinematic viscosity
Ω_{ij}	rate-of-rotation tensor (vorticity tensor)
R_{ij}	rate-of-strain tensor
u_i	velocity component in the x_i direction
u_i^g	filtered velocity component in the x_i direction
u_j	velocity component in the x_j direction
u_{ij}^g	filtered velocity component in the x_j direction
T	time
p	pressure

The superscript g - filtering at the grid scale

S_{ij}	filtered rate of strain
B_{ij}	Subgrid-scale (SGS) stress
C_s	Smagorinsky constant
f_v	Van Driest's damping function

$\acute{\phi}$	Filtered flow variable
ϕ	Original unfiltered flow variable
x	Global coordinate frame
G	Filter function
ξ	Cell local axis
Δ	Computational grid scale/filter's cut-off width
ν_{sgs}	SGS viscosity
u_{sgs}	velocity scale
k_{sgs}	Subgrid turbulent kinetic energy
l_{sgs}	Subgrid length scale
$\overline{D}_{ij}$	Filtered rate of strain tensor
V	volume of the computational cell
u_*	friction velocity
z	height r vertical displacement
z_0	aerodynamic roughness length
d	ground-normal displacement height
κ	Von Karman constant
C_l	Lift coefficient
C_d	Drag coefficient
U_x	Instantaneous distribution of the streamwise component of velocity
ω_y	Vertical distribution of streamwise velocity vector and spanwise vorticity
$\overline{C_p}$	Mean pressure coefficient

$\bar{p}$ mean pressure at the wall

$\overline{p_0}$ reference mean static pressure

$\overline{U}$ reference mean wind velocity in undisturbed flow

Abbreviations

LES Large Eddy Simulation

CFD Computational Fluid Dynamics

2D 2 dimensional

3D 3 dimensional

DNS direct numerical simulation

ABL Atmospheric boundary layer

CAARC Commonwealth Advisory Aeronautical Council

RANS Reynolds-averaged Navier-Stokes Equation

OpenFOAM Open -Source Field Operation and Manipulation

SGS Subgrid-scale stress

N-S Navier-Stokes

PISO Pressure Implicit with Splitting of Operators

SIMPLE Semi-Implicit Method for Pressure-Linked Equations

GS Grid size scales

G filter function

Cvs control volumes

Tr(B) trace of the tensor B

I identity matrix

V	volume of the computational cell
C_S	Smagorinsky constant
HPC	High performance computing
WT	Wind tunnel
b	breadth
STL	Stereolithography
CFL	Courant- Friedrichs-Lewy
FWMCs	Finite Wall-Mounted Cylinders
AR	Aspect ratio

Chapter 1

INTRODUCTION

Building neighbors give rise to interference effects on wind forces and create considerable changes on the wind loading of a tall building surrounded by building neighbors, such as low-rise buildings. Wind loads caused by interference from building neighbors can be modified by a variety of factors, including geometry and arrangement of buildings, terrain type, and approaching flow turbulence intensity. The number of conceivable combinations of these parameters are enormous, making it impossible to cover them all. As a result, a more physically based approach to solving the problem, such as researching the underlying mechanics of interference effect, might be worthwhile [1]. Furthermore, the aerodynamic interaction between building neighbors is essentially an unavoidable feature, as the surrounding environment for the tall building may change dramatically over time due to rapid expansion inside city centers, resulting in flow variation complexity. The presence of building neighbors can cause wind to deflect downwards as seen in Figure 1.1.

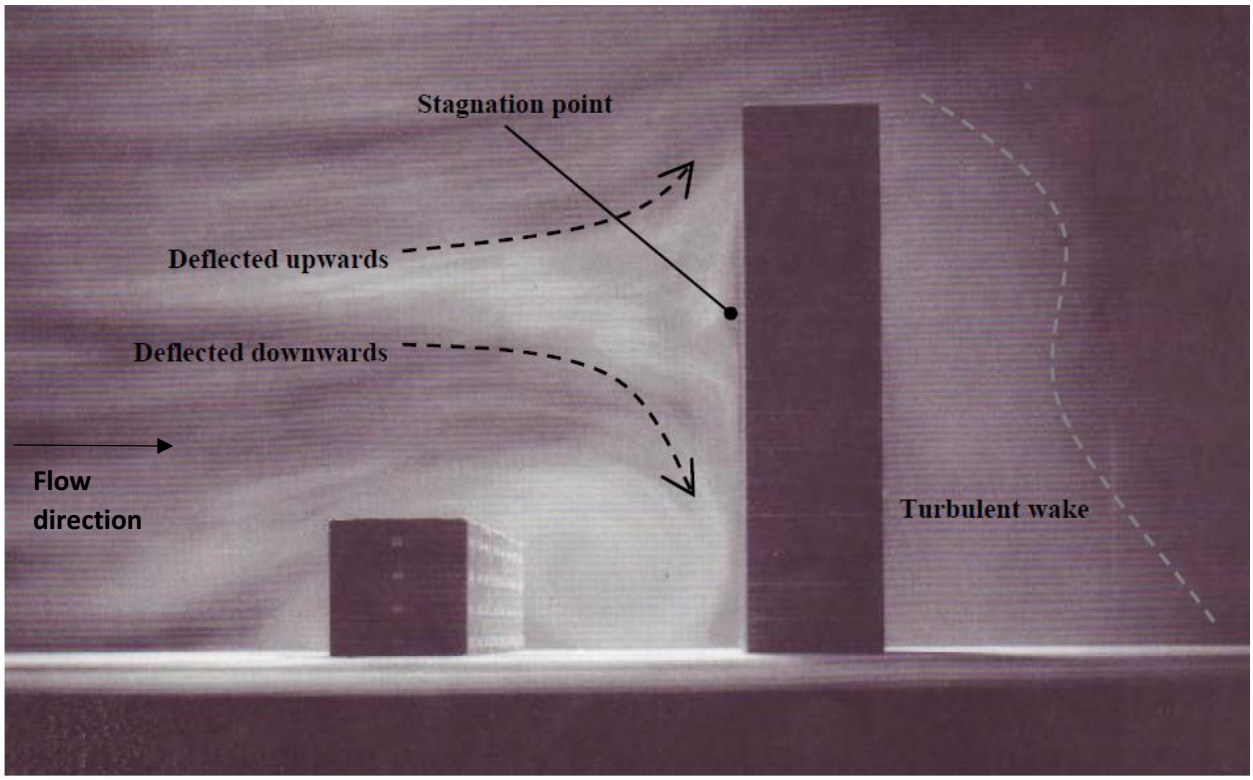

Figure 1.1: Flow around a slab block screened by a low building. Adapted from [2].

Every year, natural disasters such as cyclones, earthquakes, floods, and landslides occur in different parts of the world. Wind changes during high-wind events can have a significant impact on building envelopes, often resulting in major repercussions such as roof failures [3]. This is due to wind uplift pressure, which causes roof membranes to flutter or flap up and down quickly [4]. The interaction of wind flow with the building's surface determines the aerodynamic loads on the roof and walls of a building, and this interaction is principally determined by the building's geometry and flow characteristics [5]. Engineers consider wind load on their design. However, considering the effects of other building effects are very rare and uncommon. It is important to conduct a wind assessment to determine an in-depth understanding of the type and magnitude of wind loads buildings will be subjected to. Excessive wind-induced vibration and damage to roofs during windstorms are two of the negative consequences of the new generation of high-rise buildings.

Due to lack of space, sufficiently tall vertical structures are required to accommodate the growing population. However, in terms of height or number of floors, there is no proper categorization for the word "tall buildings" yet. Tallness is a subjective matter that is influenced by perception and situation. Though there is no specific classification, a tall structure can be broadly characterized as one that, due to its height, is subjected to lateral forces such as wind and earthquake to the point that they play a significant role in structural design.

Tall buildings are now seen as a symbol of urbanization. The key characteristic that distinguishes tall buildings from other low-rise buildings is lateral forces, with wind force being the most significant force on tall buildings. Different aerodynamic wind forces are acting on a typical structure [6]. One is extraneous-induced loading, which is created by buffeting from the inherently turbulent oncoming wind. Wake effects from an upstream structure can amplify this effect [6]. The other arises from unsteady flow phenomena such as flow separations, reattachments, and vortex shedding.

Most cities in North America are made up of rectangular prisms that act as a bluff body when there is wind. This has two advantages: it provides knowledge of expected flow structures from general bluff body aerodynamics research, and it allows the urban domain to be divided into simpler geometric blocks [7]. The rapid growth of high-rise buildings around the world has sparked interest in the optimization and development of more widely used techniques for determining wind-induced load effects for tall, slender structures. The main structure of a high-rise building, which is a tall building must be designed to safely withstand the extreme wind effects it will be subjected to throughout its expected lifetime, which is why determining the wind load effect, which encompasses all wind phenomena that occur for tall, slender structures, is critical. When inspecting high-rise buildings, wind phenomena such as vortex shedding, which causes building motion owing to crosswind excitations, and aerodynamic instability, both of which contribute to higher loading and occupant discomfort, are common.

At the pedestrian level, wind conditions around high-rise buildings in cities can cause adverse and dangerous environmental problems. Pedestrians and residents of low-rise buildings near tall buildings may be inconvenienced due to this situation. The level of disruption to pedestrians might vary depending on the wind’s characteristics, such as mean magnitude, uniformity, ambient

temperature, and so on. If wind characteristics are accurately assessed, remedial actions may be taken.

Most people find high winds and gusty winds uncomfortable, and pedestrians have been swept over because of sufficiently high winds because buildings cause the greatest relative changes in wind speed, pedestrians feel the full impact of these changes in wind speed at the ground level. People can be knocked over and become injured [8], and people's clothes are blown around and eyes are irritated due to these changes. Therefore, the impact of buildings on the comfort of those living nearby can range from risky to disastrous. To design comfortable public spaces, architects and city planners do not need to know the exact wind speed in a certain location, but they do need to know which areas are protected from the wind. They also need to be aware of those who will be exposed to artificial wind, particularly around areas where adjacent buildings are in proximity to each other, which would cause discomfort to pedestrians. Passages between buildings are always regarded as high-wind zones, resulting in a "channeling effect." This effect alters the local wind flow between buildings, which might result in hazardous wind conditions. Pedestrians are inconvenienced, and windows and doors around these passages can be damaged [9].

1.1 STATEMENT OF THE PROBLEM

The focus of this research work is to investigate the influence of building neighbors on wind flow around a tall building. Because of the increased height and usage of light-weight construction materials of tall buildings, lateral loads have become more important than gravity loads in the design of high-rise buildings. As a result, it is now required to factor in the effects of wind forces to assure the serviceability and stability of tall buildings and their building neighbors. This research is also important because it bridges the gap between architecture and engineering by providing an aerodynamic assessment during the design stage of a small building around a tall building, to minimize pedestrians' discomfort around both buildings and minimize roof damages of a low-rise buildings around a tall building. There is limited information about fluid dynamics and the knowledge obtained from this research will be essential in understanding the fluid dynamics, wake flow structures and vortex structures generation. This will assist building designers in determining the best location for constructing a small building close to a tall building. Numerical simulations are first conducted for a single tall building before numerical investigation for a small building

placed upstream and downstream of a tall building was conducted to study the influence of building neighbors around a tall building. LES (large eddy simulation) is applied in this study and is said to have progressed to the point where complex turbulent flow around actual buildings can be analyzed in an acceptable amount of time, and should be considered as a complementary technique for wind load evaluation [10].

1.2 OBJECTIVES OF THE STUDY

This research work involves the use of LES to study the effect building neighbors (small buildings) have on wind flow over a tall building. The main goal of this thesis is to identify, define, and model wake flow structures and wind flow fields over a twin-building arrangement (with a small building present both downstream and upstream of a tall building). Wind flow fields are thoroughly investigated by analyzing pressure and velocity distributions around the buildings to study fluid dynamics and flow features formed. Wake dynamics is examined using flow structural analysis of the wakes, while vorticity distribution is used to show the effects of vortex shedding due to the presence of a small building around a tall building. Finally, to further investigate the pressure distribution on the faces of the buildings, mean pressure coefficients around the faces of the buildings are studied to show how a small building can have an impact on the mean wind load of a tall building. This provides an in-depth understanding of how a small building can alter wake effects and how vortex shedding effects significantly change when a small building is in proximity to a tall building. The impact a small building will have on pedestrian comfort when placed downstream and upstream of a tall building will also be investigated in this research.

1.3 STRUCTURE OF THE THESIS

The thesis is divided into 6 chapters. Chapter 2 gives a brief background of the research topic which includes a literature review on wind flow around tall buildings, fluid dynamics, wake dynamics, atmospheric boundary layer flow, and computational fluid dynamics modelling of wind flow over buildings. Chapter 3 is the research methodology and illustrates the governing equations, numerical methods, computational domain, boundary conditions, and wake refinement used in this research. Chapter 4 discusses the effect of wind flow over a single tall building. Chapter 5 evaluates the wind effects on a small building when it is placed downstream and upstream of a tall building. Chapter 6 summarizes the compelling findings from the research and provides recommendations for further research.

Chapter 2

BACKGROUND

2.1 Wind Flow around Tall Buildings

The exhaust from heating and ventilation systems, kitchens, and incinerators contributes to pollution in most buildings. They contribute to air pollution that is generated elsewhere, such as by vehicles. The wind around the building can aid or hinder the dispersion of these airborne pollutants, making it vital in determining the levels of pollution experienced by those within or near the buildings [11]. For lowering fire dangers, adequate smoke dispersion is also critical. High winds at ground level help in dispersing air pollution created by automobiles, therefore if vehicles and pedestrians must share a road, the requirement to reduce air pollution and the need to increase pedestrian comfort may conflict [12].

The wind speed is reduced, and the gustiness is increased on a building's leeward side. This makes landing aircraft and helicopters near buildings difficult and risky, which is why pilots and civil aviation officials are concerned about structures near airports [13]. The importance of these effects of the wind around a building demonstrates that the way a building's shape and size or a group of buildings encourages the wind to flow around or through it is as much a part of the building's operation as its heating, ventilation, or lighting. As a result, being able to forecast wind flow near buildings may be just as significant as being able to predict any other component of its performance for the architect and planner.

The development of more realistic estimations of wind effects on buildings has been a focus of recent efforts to prevent damage caused by high winds. For instance, flow and pressure fields around three types of bluff bodies such as a 2D square rib, a cube, and a low-rise building model with 1:1:0.5 shape were studied [14]. In 2002, Tutar & Oguz researched numerical measurements of flow conditions of turbulent wind around two parallel buildings with distinct wind directions and building arrangements [9]. The impact of wind loading on a variety of main factors associated with the design of tall buildings was investigated [15]. The translation from the complex dynamic

load effects on a 350 m high-rise building influenced by extreme wind loading to the static floor-by-floor loadings was investigated in 2015 [16]. The influence of trees on wind distortions above the roof of a 15m high building was analyzed [17]. In 2017, the turbulent flow around a bluff body for various wind velocities using two- and three-dimensional models were studied numerically [18].

2.2 Fluid Dynamics

Thesaurus dictionary defines a fluid as a substance (such as a liquid or gas), that can flow and changes its shape at a steady rate when pushed upon by a force tending to change its shape. According to Encyclopedia Britannica, dynamics is a discipline of physical science and a subdiscipline of mechanics concerned with the motion of fluid material objects in relation to physical elements such as force, mass, momentum, and energy. Fluid dynamics is a branch of fluid mechanics that deals with the flow of fluids (liquids and gases). It is divided into various sub-disciplines, one of which is aerodynamics (the study of air and other gases in motion). A fluid dynamics problem is often solved by calculating various fluid characteristics as functions of space and time, such as flow velocity, pressure, density, and temperature. Most fluid dynamics problems are too complex to be solved through direct calculation. Problems must be tackled using numerical approaches and computer simulations in those circumstances. This field is known as numerical or computational fluid dynamics (CFD), which is defined by Southard as "a branch of computer-based science that provides numerical predictions of fluid flows."

Experts in aerodynamics provided various classes for the precise characterization of a fluid condition. Viscosity, compressibility, stability, steadiness, and randomness of fluid flow are the most useful classifications. As a result, the Reynolds number, Re is defined as the fluid state's fundamental non-dimensional controlling parameter [19].

$$Re = \frac{\rho u c}{\mu} = \frac{u c}{v} \tag{2.1}$$

where ρ represents the density of the fluid, u represents the velocity scale, c represents the characteristic length scale, μ and v represent the fluid dynamic and kinematic viscosities, respectively. The Reynolds number identifies the ratio of inertial to viscous forces, which translates to which of the two fundamental flow characteristics dominates in the wake.

A fluid dynamics condition in which the velocity and pressure of a fluid flow change over time due to changes in system state is known as transient flow. A flow's transient nature is also significant, particularly in terms of wake dynamics. The flow is referred to as a steady flow if the properties are independent of time and only alter with spatial variations [20].

2.3 Wake Dynamics

The flow around bluff bodies is a basic fluid mechanics subject that has captivated researchers for more than a century. The wake is defined as the recurring flow system formed behind a bluff body, such as a flat plate, sphere, cylinder, or disc as seen in Figure 1.1. The transient nature of vortex formation and interactions dictates a wake's organization. To model urban dispersion, it is necessary to account for the wake effects of buildings, whether high-rise or low-rise buildings.

The wake flow structures/dynamics and visualization of vortical structures formed behind the building can be visualized in 3D using Q-criterion, a physical model of vortex shedding. The wake features and flow features around the building are thoroughly examined using two models below in Figures 2.1 and 2.2 respectively [9], [21].

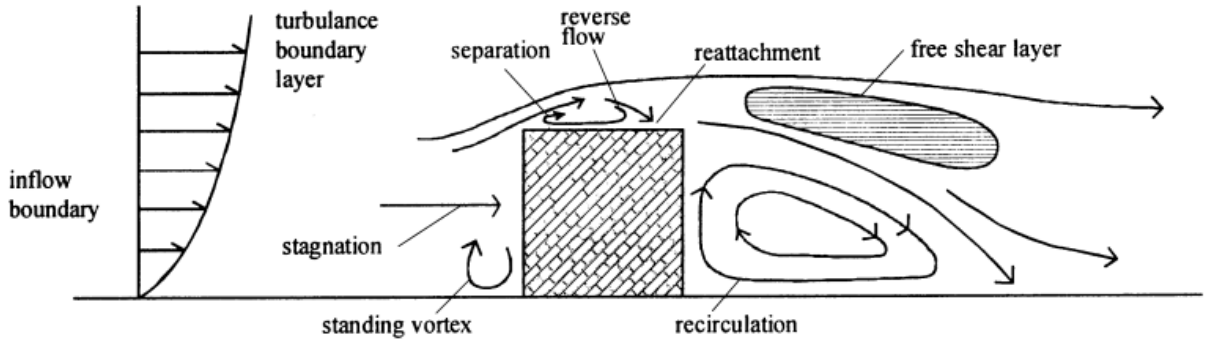

Figure 2.1: Flow structures around a building. Adapted from [9]

A vortex is defined as a connected fluid region with a positive second invariant of the velocity gradient tensor ($\nabla . V$). When Q is positive, it represents locations in the flow where rotation dominates the strain and shear. The Q criterion provides the ability to visualise vortical structures

as isosurfaces. It has proven to be more effective than other typical markers of vortices (e.g., pressure minimum, closed or spiralling streamlines and pathlines, and isovorticity surfaces) in identifying vortex cores, and is thus commonly utilised in the literature. It is applied to effectively track vortical structures. The Q-criterion, proposed by Hunt [22] was used to represent the mean streamwise vortex structure in the wake because it accurately defines vortex cores while simultaneously capturing the pressure minimum in a plane perpendicular to the vortex axis. Q is defined as,

$$Q = \frac{1}{2}(\Omega_{ij}\Omega_{ij} - R_{ij}R_{ij}) \tag{2.2}$$

where Ω_{ij} is the rate-of-rotation tensor (vorticity tensor) and R_{ij} is the rate-of-strain tensor, which are the antisymmetric and symmetric parts of $\nabla.V$ respectively. R_{ij} and Ω_{ij} are defined as,

$$R_{ij} = \frac{1}{2}(\frac{\partial u_i}{\partial x_j} + \frac{\partial u_j}{\partial x_i}) \tag{2.3}$$

$$\Omega_{ij} = \frac{1}{2}(\frac{\partial u_i}{\partial x_j} - \frac{\partial u_j}{\partial x_i}) \tag{2.4}$$

Figure 2.2 shows the wake models for wall-mounted cylinders which is like the building model used in this research to analyze flow structures.

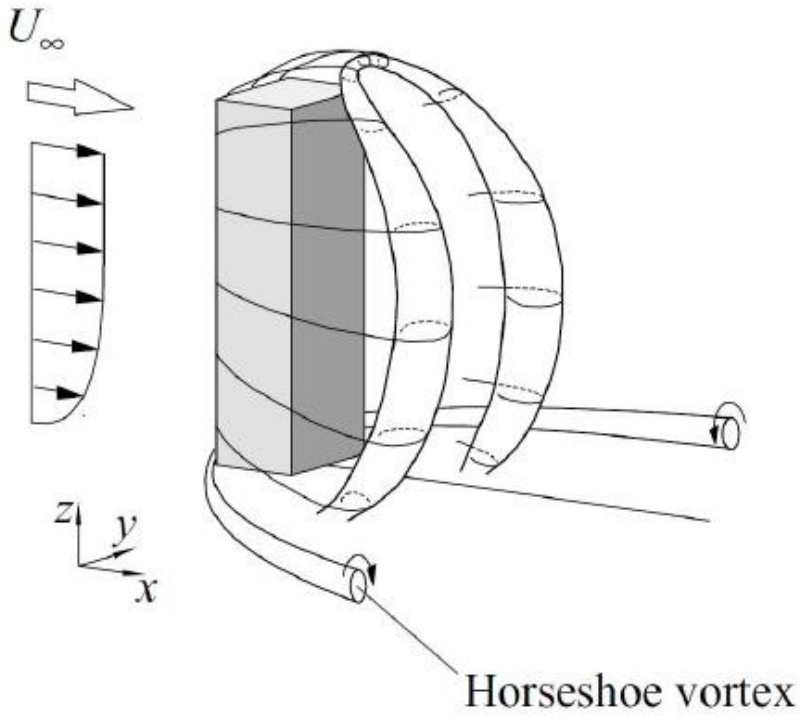

Figure 2.2: The wake models for wall-mounted cylinders. Adapted from Wang et al. [21]

Wake models for the flow around wall-mounted circular cylinders have been created since 1952 [23]. The flow structure around a square prism of finite length in a closed-circuit low-speed wind tunnel was experimentally investigated [24]. When the cylinder aspect ratio is 3 or less, the near wake structure is defined by vigorous interactions between the base and tip vortices, but at an aspect ratio of 5 and higher, it is characterised by vigorous interactions among spanwise vortices, tip vortices, and base vortices. Close to the prism base, counter-rotating base vortices dominate the near wake, reaching maximum vorticity at 1d (prism width) downstream of the prism and rapidly decaying downstream. Due to a weakening interaction between the tip and base vortices, the maximum strength and size of these vortices grow with increasing aspect ratio. Wang & Zhou [25] experimentally investigated the near wake of a finite-length square cylinder with one end placed on a flat plate and the other free. The interactions of three types of vortices, namely the tip, base, and spanwise vortices, were detected, and the near wake is defined by their interactions. Rastan et al. [26] investigated the three-dimensional unsteady flow past a finite wall-mounted square

cylinder with an aspect ratio of 7 using direct numerical simulation (DNS). To assess the onset of vortex shedding, the wake flow structure, and global quantities, seven separate Reynolds numbers (40, 75, 85, 100, 150, 200, and 250) were used. The findings indicate that the inception of vortex shedding occurs in the Re range of 75 and 85. They also found that the mean wake topology and integral parameters are significantly affected by Re. As the flow goes from steady to unsteady, the wake flow transforms from a dipole to a quadrupole. At Re = 150-200, a transition flow begins, in which the wake instabilities become more pronounced as Re increases, and the force signal oscillation shifts from sinusoidal to chaotic. At Re > 200, the wake flow starts to become turbulent. Zargar [27] studied the wake dynamics of long depth-ratio wall-mounted rectangular cylinders at Reynolds numbers ranging from 250 to 1000 with varying incidence (yaw) angles of 0 to 45 degrees, with respect to the free stream flow. Using Large Eddy Simulations, the influence of a large depth-ratio on flow parameters and vortex generation was first investigated for steady and unsteady wakes of wall-mounted cylinders at zero incident angle using LES. The unstable wake evolution by large incident (yaw) angles are examined at similar Reynolds numbers after the fundamental wake characterisation at zero incidence angle has been analyzed. Wang et al. [28] analyzed the impact of building form on the wake flow wind potential. The results showed that the building length L, width W, and rear distance D have no effect on the rear wind when the measured altitude, z is 2.5 times the building height H. The wind speed at the building's rear varies just marginally with its width. The effect of a building's height, H is usually greater than the impact of its length, L. They discovered a correlation between the rear distance at which the winds become stable and the building height, H.

2.4 Atmospheric Boundary Layer (ABL) Flow

Regional (100 -200 km), city (10 -20 km), neighborhood (1-2 km), and street level (100 -200 m) are the four major length scales employed in defining flow in urban environments [29]. The flow around individual buildings are averaged out at the regional and city scales, and the structure's drag results in flow like that over a rough surface, resulting in an ABL. The ABL is divided into two sections: the outer and surface layers, with the latter being further segmented based on the flow-surface interactions that arise as shown in Figure 2.3 [7].

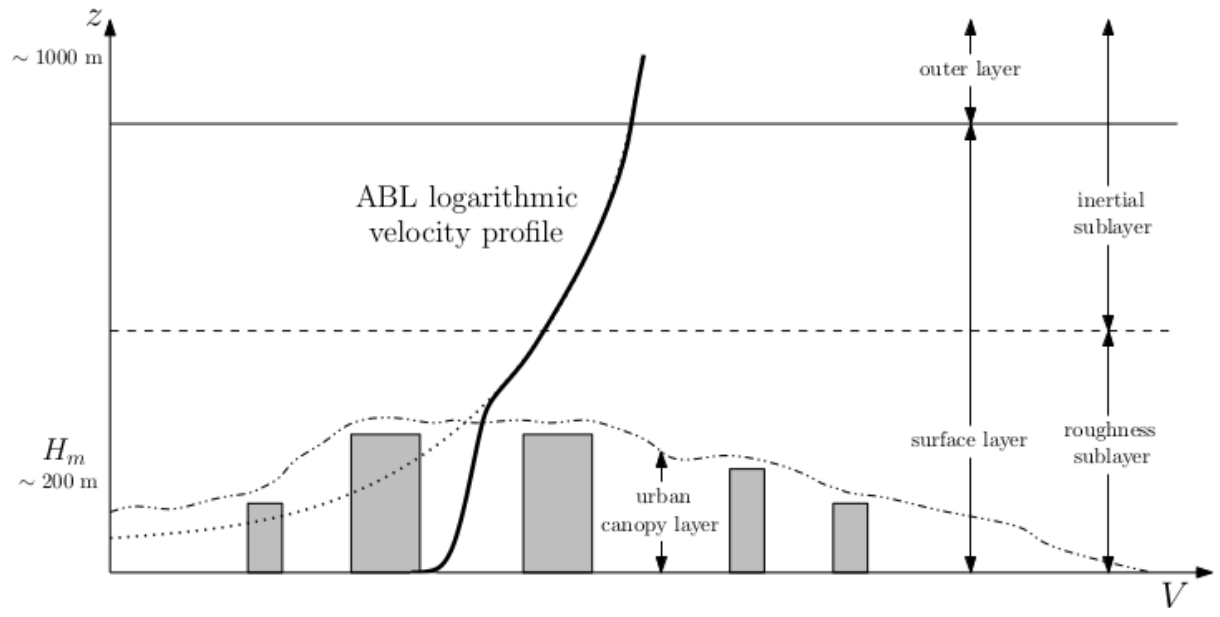

Figure 2.3: Spatially averaged mean atmospheric boundary layer velocity profile near an urban area. Adapted from [29] and [30].

Because the atmospheric boundary is affected by friction, the layer's height varies with the roughness of the surface, resulting in a lower height of the boundary layer at smooth sea terrain and a higher height at high-density housing. Strong turbulence is formed near the earth's surface as a result of friction, with turbulence prevailing at the bottom of the boundary layer and diminishing with height [16].

The velocity profile within the inner surface layers is greatly reliant on the surface roughness and the building geometry. Buildings can only be found inside this layer. At the street level scale, the urban canopy layer is found at the bottom of the roughness sublayer, where the flow is strongly influenced by the size and orientation of local objects such as buildings [29].

2.5 CFD modelling of wind flow over buildings

Computational fluid dynamics (CFD) has evolved and is widely applied in wind engineering, encompassing a growing number of topics such as flow over complex topography, pedestrian-level wind conditions, air pollution dispersion, and wind loads on buildings and structures [31]. Since the 1990s, the advancement in computers enabled researchers to use Large Eddy Simulation (LES) to analyse the highly time-dependent wind flow and wind loads of building structures.

2.5.1 LES of wind flow fields over a single isolated building

LES has been used successfully used to study wind flow around single tall buildings and Frank & Mauch in 1993 [32] studied the principle of large-eddy-simulation (LES) to practical building aerodynamic problems. Some special cases for experimental investigation of the flow around building models in a wind tunnel were illustrated by using numerical calculations. LES was used to investigate the mechanism of natural ventilation driven by wind force over "building-like" cubic bluff bodies with openings. Meanwhile, extensive airflow fields, such as mean and fluctuating velocity and pressure distribution inside and around building-like models were calculated for model validation via wind tunnel tests and compared with LES results [33]. Sohankar [34] studied the uniform approach flow over a square section building with different Reynolds numbers, ranging from 10^3 to 5 x10^6, using large eddy simulation (LES). Large-eddy simulation (LES) was applied to model urban dispersion problems that includes a new dynamic sub-grid closure and boundary treatment. The numerical model was developed, validated, and expanded to include a realistic urban layout [35]. Penttinen [36] compared a simple structure with two different LES models, described by a square channel with unchanged boundary conditions at the inlet. The effects of wind over a building from the point of view of installing small wind turbines were investigated using LES around a rectangular prism-shaped structure [37]. Bazdidi-tehrani et al. [38] investigated the impact of grid resolution on the accuracy of large eddy simulation (LES) dispersion predictions around an isolated cubic building. Cheng & Porté-Agel [39] analyzed four subgrid-scale (SGS) models which were tested with large-eddy simulations of flow past a two-dimensional (2D) block. Gousseau et al. [40] investigated the need for Validation and Verification (V&V) studies for LES of wind flow around an isolated high-rise building with an aspect ratio of 1:1:2. The numerical findings were compared with measurements from a reference wind-tunnel experiment in the first part of the analysis and the agreement was quantified using validation metrics. Joseph et al. [41] conducted a LES simulation of turbulent flow past a bluff-body. To solve the LES filtered transport equations governing the three-dimensional incompressible flow in the wake of the body. LES was implemented to generate urban wake fields to study the effects on autonomous quadrotor's flight performance [7]. Ai & Mak [42] explored the factors affecting the LES modelling of flow and dispersion around an isolated building. Two wind tunnel experimental datasets were used to validate the LES model. Large-eddy simulations for the flow field around an isolated building and within a cubic building array were carried out to explain the effect of several

numerical conditions on turbulent statistics [43]. Ricci et al. [44] researched how large Eddy Simulations (LES) are conducted on an isolated high-rise building to test the wind loads. The findings were evaluated in terms of both pressure distributions and internal forces on the structural elements to test the capabilities of LES for adoption as a design tool.

2.5.2 CFD analysis of wind flow around two buildings

Tall buildings are frequently built in clusters rather than alone in a true metropolitan area. Various benchmark studies of LES on buildings have been conducted with satisfactory agreement to validate numerical results with wind tunnel experiments. For instance, research on the numerical evaluation of wind pressures on tall buildings using the Commonwealth Advisory Aeronautical Council (CAARC) building model was conducted. The CARRC model has been widely used in wind tunnel studies to study wind loading on tall buildings and is typically adopted for experimental techniques. RANS (Reynolds-averaged Navier-Stokes) and LES simulations were conducted in this study for some cases [45]. Gnatowska [46] evaluated the use of numerical calculation (steady and unsteady RANS) to forecast wind-induced pressure loads on tandem buildings in the built-up area. The essential task was to estimate the effect on their surfaces, the distance between barriers on the pressure loads. It was found that the pressure distribution on the downstream object differs significantly by changing the distance between buildings.

The interference effect has been shown to significantly alter the wind loading of a building that is surrounded by neighboring buildings. The effect of neighbouring buildings has a significant impact on the aerodynamic response of buildings. Attempts have been made experimentally and numerically to comprehend various interference mechanisms between building neighbors. A few experimental studies have been conducted to predict wind environmental conditions around two parallel buildings. Gandemer [47] conducted a fundamental study with the goal of generalising and codifying wind environmental conditions and their effects around buildings of various geometries in the context of aerodynamic concepts. Ishizaki and Sung [48] measured wind speeds in a passage between two buildings of equal height. In a wind tunnel, they took measurements for only one wind direction. Melbourne and Joubert [49] reported on the results of wind tunnel velocity measurements in building passages. Wiren [50] conducted an experimental study to determine wind velocities in passages between and through block-type rectangular building models of equal height. In a boundary layer wind tunnel, Stathopoulos and Storms [51] conducted an extensive

experimental study of wind environmental and turbulence conditions around two buildings with varying passage widths, heights, and wind azimuths.

The velocity spectrum in the wake of a tall building model with and without an identical upstream building in a tandem arrangement was measured and it was discovered that the periodic vortex shedding was visible for the isolated building but completely disappeared for the building with an upstream building [52]. They concluded that the upstream building interfered with the downstream building's vortex shedding. Using a smoke visualisation technique, Sakamato and Haniu [53] observed the reattachment of an upstream building's shear layer to the side surface of a downstream building in a variety of staggered arrangements. Gowda and Sitheeq [54] visualised the flow pattern between two tandem buildings and discovered that as the spacing between two buildings increased from small to large values, the downstream building went through three stages: submergence in the shear layers, being attacked by the shear layer directly on the windward surface, and insusceptibility to interference. Hui et al. [55] observed the flow pattern between two rectangular-section high-rise buildings and discovered that the shear layer from the upstream building was the source of peak pressure on the downstream building.

Chapter 3

METHODOLOGY

3.1 Introduction

This chapter explains the mathematical model and numerical methods used in the study. Further, it provides a discussion of the underlying governing equations, numerical approach, the turbulence modelling approach employed, tools for the analysis, computational domain, boundary conditions and wake refinement for the three cases (single tall building, small building downstream, and small building upstream).

Wind tunnel tests and full-scale measurements have traditionally been used to collect this information. However, these approaches can be time-consuming and expensive. Computational Fluid Dynamics (CFD) approaches are becoming increasingly commonly regarded as an alternative tool for predicting turbulent flow over buildings. In this research, CFD approach is taken to solve the problem and used in this research because they can simulate the flow field around a building and predict important characteristics like velocity, pressure, and temperature fields [56].

3.2 Governing equations

The flow field around an individual building and two twin-building layouts (small building placed downstream and upstream of a tall building) is estimated using Large Eddy Simulations (LES). The LES formulations are based on the spatial filtered incompressible Navier-Stokes (N-S) and continuity equations, with the smaller flow scales (relative to the smallest grid-size) being modelled and the larger scales being solved directly.

The governing equations for LES are the filtered continuity equation and the filtered Navier Stokes equation or momentum equation which are solved using OpenFOAM (Open-Source Field Operation and Manipulation).

$$\frac{\partial u_i^g}{\partial x_i} = 0 \tag{3.1}$$

and the filtered Navier-Stokes equations

$$\frac{\partial u_i^g}{\partial t} + \frac{\partial u_i^g u_j^g}{\partial x_j} = \frac{-1}{\rho}\frac{\partial p^g}{\partial x_i} + 2\nu\frac{\partial S_{ij}}{\partial x_j} - \frac{\partial B_{ij}}{\partial x_j} \tag{3.2}$$

$$S_{ij} = \frac{1}{2}\left(\frac{\partial u_i^g}{\partial x_j} + \frac{\partial u_j^g}{\partial x_i}\right) \tag{3.3}$$

$$B_{ij} = \left(u_i u_j\right)^g - u_i^g u_j^g \tag{3.4}$$

where u_i is the velocity component in the x_i direction, u_j is the velocity component in the x_j direction, t is the time, ρ is the density of air, p *is the* pressure, S_{ij} is the filtered rate of strain and ν is the kinematic viscosity. The superscript g denotes filtering at the grid scale.

The subgrid-scale (SGS) stresses, B_{ij} are computed using the standard Smagorinsky model [37].

$$B_{ij} = (C_s f_v \Delta)^2 \left(2S_{ij}S_{ij}\right)^{\frac{1}{2}} \tag{3.5}$$

where C_s is the Smagorinsky constant, f_v is Van Driest's damping function and Δ is the computational grid scale [37].

3.3 Discretization and Interpolation Methods

OpenFOAM, like many other modern CFD systems, uses the finite volume method to discretize partial differential equations. In a wide number of monographs devoted to numerical methods and fluid flow modelling, the method and its application to the Navier-Stokes equations are thoroughly described. The finite volume method divides the computational domain into many small non-

intersecting polyhedral known as control volumes (CVs) [57]. There are other techniques, however with OpenFOAM, all variables are kept at the centroids of the control volumes. The centroid value represents the entire CV. It is simple to demonstrate that this is a second-order accurate approximation. Integrating the original equations across a control volume and a time interval, *t* is the first step in obtaining the discretized form of the equations. The Gauss theorem is then utilised to convert volume integrals into surface integrals where it is applicable. The convection, diffusion, and pressure gradient terms in the momentum equation are discretized using the Gauss linear scheme, while the temporal discretization is done using the Euler implicit scheme.

3.4 Numerical Approach

The $(x_1, x_2, x_3) = (x, y, z)$ right-handed rectangular Cartesian coordinate system is employed, with x_3 being the vertical direction [37]. The OpenFOAM C++ libraries is used to integrate the governing equations. To solve the non-dimensional incompressible Navier-Stokes equations, the pimpleFoam solver, which is an incompressible solver and one of the standard solvers given by OpenFOAM is chosen. The PIMPLE Algorithm is a hybrid of the PISO (Pressure Implicit with Splitting of Operators) and SIMPLE algorithms (Semi-Implicit Method for Pressure-Linked Equations).

3.5 Turbulence Modelling

While RANS based methods are the most widely used in the engineering sector, existing turbulent models assume that the various turbulent scales behave in the same way [7]. Unlike RANS models, which use time-averaged equations, Large Eddy Simulations use volume-averaged Navier-Stokes equations.

Large eddy simulation can provide additional turbulence information on the resolved small scale eddies, which was applied in this study. Researchers in the past performed numerical simulations using both RANS and LES and found out that LES was superior to RANS in extracting turbulence information around bluff bodies such as buildings. Rodi [58] analyzed LES and RANS calculations of vortex-shedding flow past a square cylinder at Re = 22,000 and 3D flow past a surface-mounted cube at Re = 40,000 for two basic bluff body flows with simple geometries but complex flow behaviour. Turbulence fluctuations were severely underpredicted in all RANS calculations; the

relatively high value of these fluctuations in the experiment may be attributed to low frequency variations of the shedding motion due to 3D effects that are not accounted for in 2D RANS calculations. The flow characteristics around a high-rise building was investigated using RANS and LES by Vita et al. [59] in 2020 with variations of the turbulence characteristics at the inlet. The results were compared to wind tunnel tests. RANS produces reliable results in flow regions heavily influenced by the building model, but it is inaccurate in flow regions heavily influenced by atmospheric/ambient conditions. LES, on the other hand, is usually dependable if a suitable turbulent inflow is included in the simulation. When a turbulent inflow is included in the simulation, RANS correctly predicts the flow close to the leading edge. However, results do not agree with LES data, which were found to be more responsive and closely match wind tunnel experiments, downstream of the roof's surface as the separated flow reattaches and strong interaction with the turbulent inflow occurs. RANS over-predicts the magnitude of the separated flow in the wake region at all distances investigated, while LES shows a rapid decay of the wake [59]. RANS only performs correctly in a well-correlated and coherent portion of the flow pattern in this scenario, as the results do not align at any locations.

LES is, therefore, more accurate than RANS because LES entails spatial filtering of flow variables, primarily velocity and pressure, using the smallest grid size possible. Structures with grid size scales (GS) are resolved, while those with subgrid scales (SGS) are modelled. Small turbulent eddies are more universal and isotropic in nature than large energy containing eddies. While the effect of small eddies on the flow is important, resolving down to the Kolmogorov length scale is computationally expensive in terms of both spatial and temporal resolution [7]. LES was developed to directly resolve transient and geometry-dependent motions while modelling the energy-draining effects of small eddies on the resolved flow to computational cost. Since LES directly resolves large-scale unsteady motions, it is expected to be more accurate than RANS for modelling flow over bluff bodies, such as urban structures with large scale unsteadiness [7].

LES is a low-pass filter that is used to reduce high-frequency turbulent motions while keeping low-frequency motions unaffected. The resolved and modelled length scales are defined by applying a spatial filter with a cut-off width [7]. Separation of scales is performed through a filtering process, which is theoretically described as a convolution of the relevant flow field with a selected filter function [57].

$$\acute{\phi}(x,t) = \iiint_{-\infty}^{\infty} \phi(x,t) G\,(x-\xi,\Delta) d^3\xi, \tag{3.6}$$

where $\acute{\phi}$ is the filtered flow variable, ϕ is the original unfiltered flow variable, x is the global coordinate frame, G is the filter function, ξ is a cell local axis and Δ is the filter's cut-off width, which is a parameter that specifies the size of the filtered scales. Filtered variables are indicated by the over-bar sign. The flow field's unresolved part, which is left out after filtering, is defined as:

$$\phi''(x,t) = \phi(x,t) - \bar{\phi}(x,t). \tag{3.7}$$

where ϕ (total flow variables) are separated into filtered ($\bar{\phi}$) and subgrid scale components (ϕ''). Subgrid scales are typically used to describe the length scales connected with the unresolved part (SGS).

Despite the enormous number of filters, majority of them are challenging to implement in a general-purpose CFD-code. The top-hat filter is the most popular filter used with finite volume discretization.

$$G(x-\xi,\Delta) = \begin{cases} 1/\Delta^3, |x-\xi| \le \Delta/2 \\ 0, otherwise. \end{cases} \tag{3.8}$$

The filtering results in a value that is an average over a rectangular volume of Δ^3 [57]. The cubic root of the volume of the (local) computational cell is a popular choice for Δ.

$$\Delta = \sqrt[3]{\Delta x \Delta y \Delta z} \tag{3.9}$$

where Δx, Δy, Δz are the cell sizes along the respective coordinate axes.

The filter cut-off width, Δ chosen makes ϕ conveniently equal to the average value of ϕ in the computational cell. This means that during the computational procedure, no explicit filtering is required; instead, the filtering is integrated into the discretization method itself. The combination of the top-hat filter and the filter cut-off width, Δ described and used in LES simulations are due to this appealing filtering property above.

It is possible to establish conservation rules for the filtered flow variables by formally applying the filtering operation to the continuity equation and Navier-Stokes equations. When doing so, it is easier to utilise tensor notation, which results in shorter and compact expressions.

Here, the filtering is simple to apply because of the linearity of the continuity equation. The equation's form does not change.

$$\frac{\partial u_i^g}{\partial x_i} = 0 \tag{3.10}$$

This result implies that the SGS velocity field. When the Navier-Stokes equation is filtered, the equation results to:

$$\frac{\partial u_i^g}{\partial t} + \frac{\partial}{\partial x_j}(u_i u_j)^g = \frac{-\partial p^g}{\partial x_i} + \nu \frac{\partial^2 u_i^g}{\partial x_j \partial x_j} \tag{3.11}$$

However, the fundamental issue is that the advection term in the equation above cannot be stated in terms of u_i^g**.** The resolution to this problem is to introduce the so called SGS stress tensor B, where the components are defined by,

$$B_{ij} = (u_i u_j)^g - u_i^g u_j^g \tag{3.12}$$

Putting the equation 3.12 into equation 3.11 gives:

$$\frac{\partial u_i^g}{\partial t} + \frac{\partial}{\partial x_j}\left(u_i^g u_j^g\right) = \frac{-\partial p^g}{\partial x_i} - \frac{\partial B_{ij}}{\partial x_j} + \nu \frac{\partial^2 u_i^g}{\partial x_j \partial x_j} \tag{3.13}$$

B must be modelled to close this system of equations.

3.5.1 Subgrid Stress Modelling

There has been a wide range of ways to modelling B explored. Only a few of the models proposed have been implemented in general-purpose CFD software. The reason for this is that some models are difficult, if not impossible, to integrate into the code's overall framework or discretization methods the code uses [57]. The Boussinesq assumption, which states that the SGS-stress may be modelled structurally similarly to the viscous stress, is a typical method to SGS-modelling. Most RANS turbulence models use a similar concept. It can be expressed mathematically as:

$$B = \frac{1}{3}Tr(B)I + \nu_{sgs}(\nabla u + \nabla^T u), \tag{3.14}$$

where Tr(B) denotes the trace of the tensor B, I is the identity matrix, and ν_{sgs} is known as the SGS viscosity, which is to be computed from the filtered velocity field.

Assuming equation 3.14, the goal is to figure out how to calculate SGS viscosity [57]. To do so, one must accept the hypothesis that the subgrid scales may be described using only a characteristic length scale and time scale. The SGS viscosity can then be determined based on dimensionless grounds as:

$$\nu_{sgs} \sim \frac{l_{sgs}^2}{t_{sgs}} = u_{sgs} l_{sgs} \tag{3.15}$$

where u_{sgs} is the corresponding velocity scale. The filter cut-off width is a natural choice for l_{sgs}. The choice of u_{sgs} is less straightforward, and different models employ various strategies.

We employ a model that was proposed independently and is based on solving a transport equation for the subgrid turbulent kinetic energy, k_{sgs}. The typical velocity scale is a suitable choice for it is given by:

$$u_{sgs} = \sqrt{k_{sgs}} \tag{3.16}$$

The transport equation for k_{sgs} is,

$$\frac{\partial k_{sgs}}{\partial t} + \frac{\partial \bar{u}_i k_{sgs}}{\partial x_i} = 2\nu_{sgs}|\bar{D}_{ij}|^2 - C_e \frac{k_{sgs}^{3/2}}{\Delta} + \frac{\partial}{\partial x_i}\left(\nu_{sgs}\frac{\partial k_{sgs}}{\partial x_i}\right) + \nu \frac{\partial^2 k_{sgs}}{\partial x_i \partial x_i} \tag{3.17}$$

where $\bar{D}_{ij}$ is the filtered rate of strain tensor and C_e = 1.048 is a constant. The following is the expression for ν_{sgs}.

$$\nu_{sgs} = C_k \Delta \sqrt{k_{sgs}} \tag{3.18}$$

where, C_k = 0.094, is also another model constant.

The four terms on the right-hand side of the equation physically represent the production of turbulence by the resolved scales, turbulent dissipation, turbulent diffusion, and viscous dissipation, respectively.

3.5.2 Smagorinsky Model

Smagorinsky was the first to introduce the Smagorinsky model, which was related to the viscous stresses. The Smagorinsky model used in this research is one of the simplest and most dependable subgrid size models. The local grid size in this model is taken as the width of the filter. The following is the model's formulation [60].

$$\hat{t}_{ij}^{SGS} - \frac{1}{3}\delta_{ij}\hat{t}_{kk}^{SGS} = -\nu_{SGS}\left(\frac{\partial \hat{u}_i}{\partial x_j} + \frac{\partial \hat{u}_j}{\partial x_i}\right) = -2\nu_{SGS}\hat{S}_{ij} \tag{3.19}$$

The isotropic component of stresses is not modelled, but is added to the pressure term, and the remaining SGS viscosity, must be further modelled [31]. According to the dimensional analysis, ν_{SGS} is proportional to a length scale and a velocity, both of which are local subgrid scale characteristics. The filter width is utilised as the length scale, and the velocity is calculated from the magnitude of the resolved rate of strain tensor ($|\hat{S}|$), resulting in,

$$\nu_{SGS} = (C_S\Delta)^2\,|\hat{S}| \tag{3.20}$$

The filter width is computed by:

$$\Delta = (\delta V_{ijk})^{\frac{1}{3}} \tag{3.21}$$

where V is the volume of the computational cell; C_S is the Smagorinsky constant equal to 0.1. This model is also purely dissipative because it only allows for forward transfer of kinetic energy. The C_S value is assumed to be a constant in the Smagorinsky model. Further analysis of the model found that C_S ranges between 0.065 and 0.25 depending on the flow conditions [60].

3.6 Tools for the Analysis

OpenFOAM was chosen as the software library for running CFD simulations in this research and it was used because the source code is easily editable and accessible. In addition, simulations can be run in parallel using high performance computing (HPC) clusters with multiple processors. As a result, it can reduce simulation time for large projects with high number of grids.

The simulations were performed using Compute Canada HPC Clusters (Graham and Cedar), and the building geometry was created using FreeCAD (a free 3D CAD modeller). Using a

combination of Paraview, Tecplot, and WebPlotDigitizer, the simulation results were then processed. Transient PIMPLE algorithm was used in this research to solve the LES and the timestep is set such that the Courant-Friedrichs-Lewy (CFL) number in the smallest grid cells stays at an average of 0.8. This CFL range is employed to maintain stability while also allowing for resolving acceptable turbulent timescales. After specifying simulation specific details in the several setup files in OpenFOAM, such as the freestream wind velocity, geometry names, meshing densities, and parallel processors, the simulation is ready to run [7].

3.7 Computational Domain

Figure 3.1 illustrates the computational domain for the single tall building. This domain was created for benchmarking and validating wind tunnel results obtained from Meng & Hibi wind tunnel experiment [61]. The building's dimensions shown in Figure 3.2 and 3.3 are the same as those used in Meng & Hibi [61] wind tunnel (WT) experiment: the breadth is b, depth is b, and height is 2b, where b equals 0.08 m. The computational domain spans x = 6.5b to x = 15.5b in the streamwise direction, y = -6.875b to y = 6.875b in the spanwise direction, and z = 0 to z = 11.25b in the vertical direction, with the coordinate origin being the center of the building's bottom. The overall number of grids for the coarse mesh is estimated to be around 1.67M.

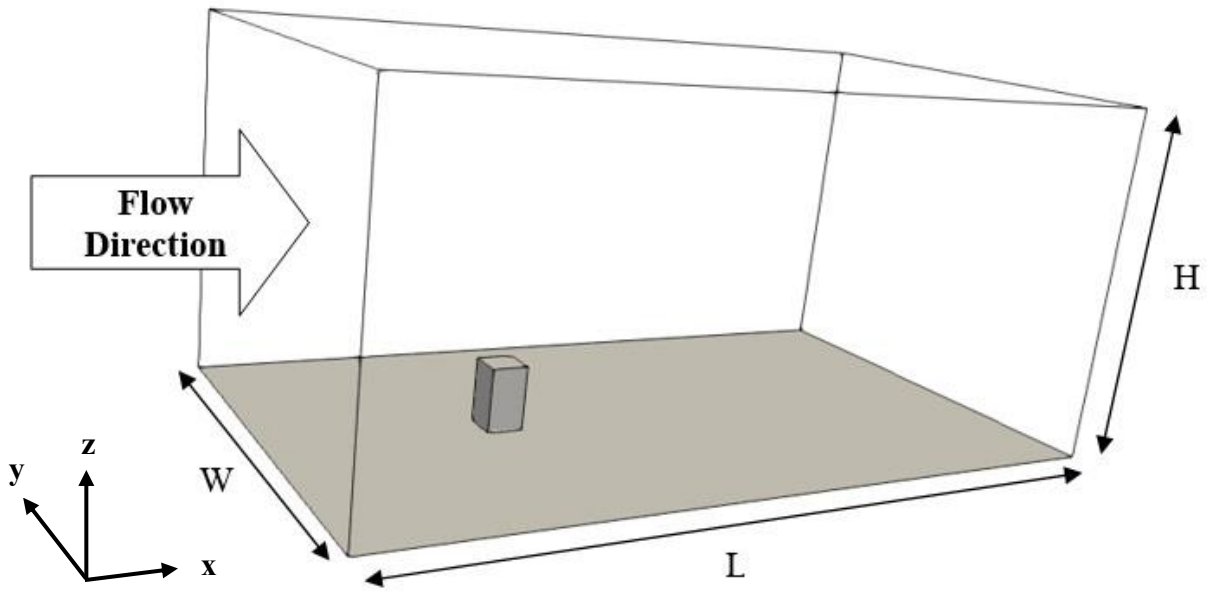

Figure 3.1: Schematic of the computational domain (Single tall building)

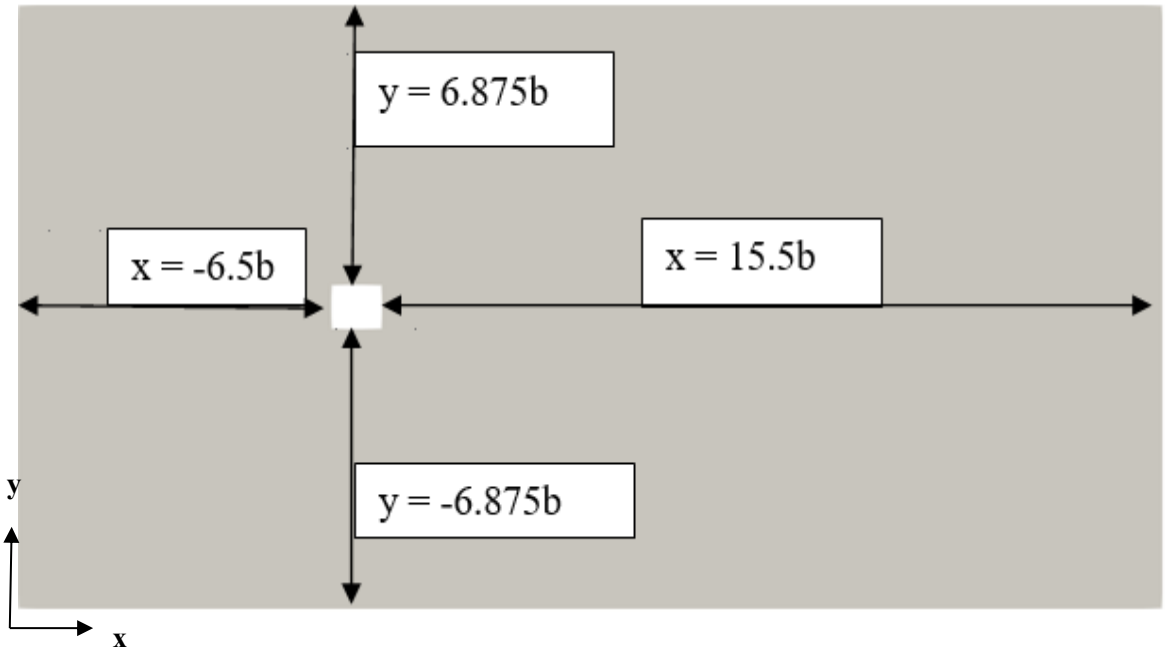

Figure 3.2: Computational domain with dimensions for the single tall building (Top view)

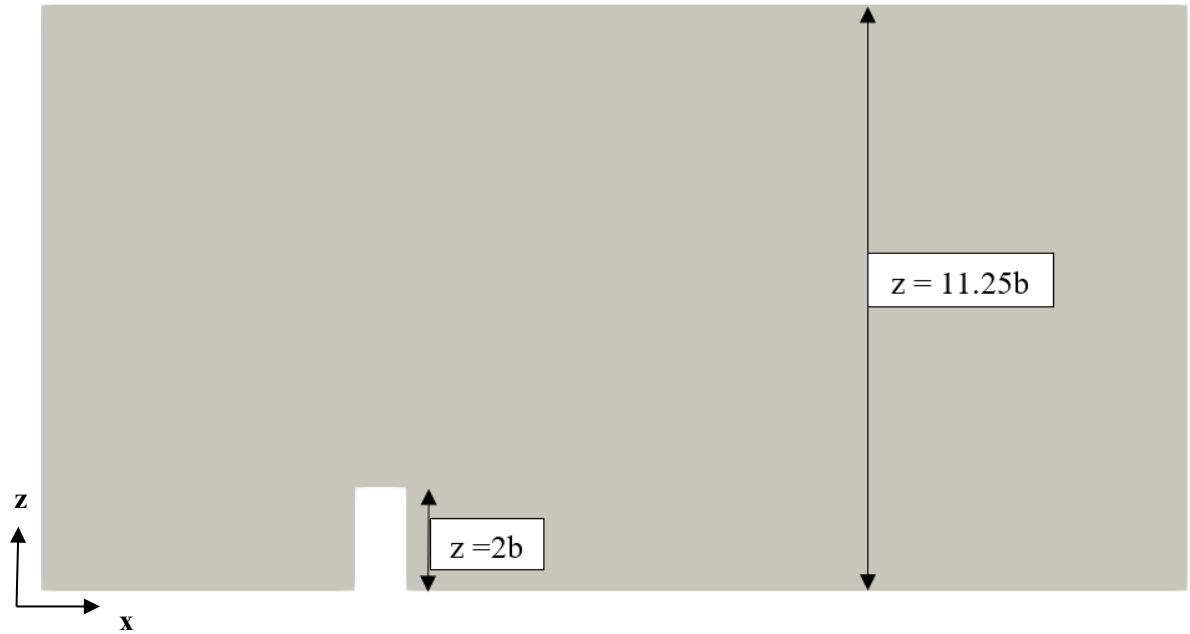

Figure 3.3: Computational domain with dimensions for the single tall building (Side view)

Figure 3.4 illustrates the computational domain for the twin building configuration, when a small building is placed downstream of a tall building. Figure 3.5 and 3.6 denotes the computational domain with dimensions. The breadth is b, depth is b, and height is 2b for the tall building and the height of the small building is b, where b equals 0.08 m. The computational domain spans x = -7.5b to x = 20b in the streamwise direction, y = -6.875b to y = 6.875b in the spanwise direction, and z = 0 to z = 11.25b in the vertical direction. The spacing between the buildings is 'b' and the overall number of grids is estimated to be around 1.73M for the coarse mesh.

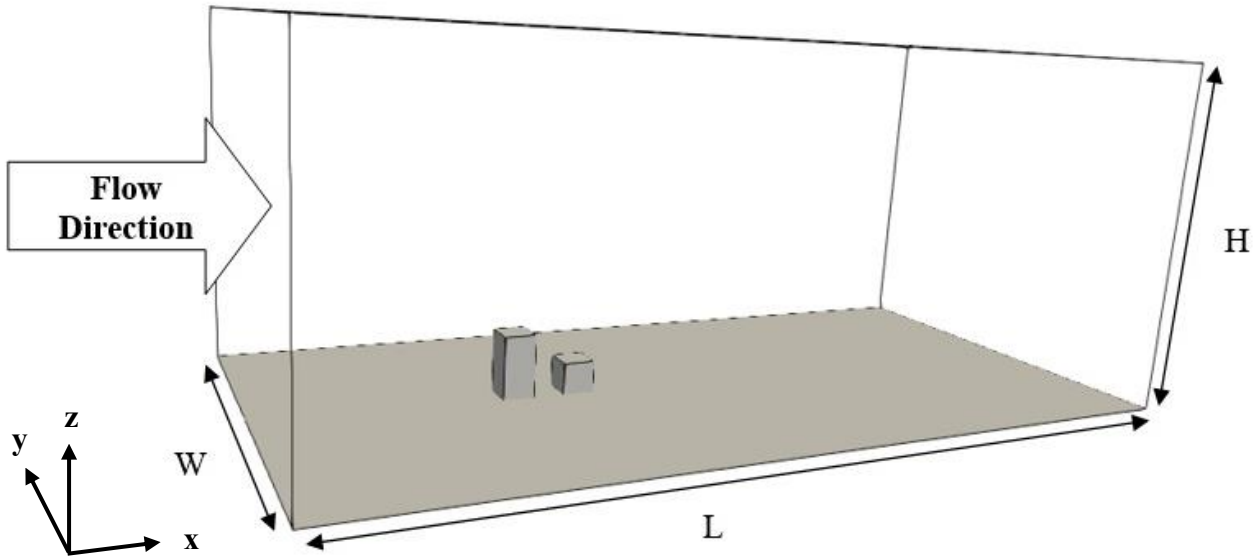

Figure 3.4: Schematic of the computational domain (Small building downstream)

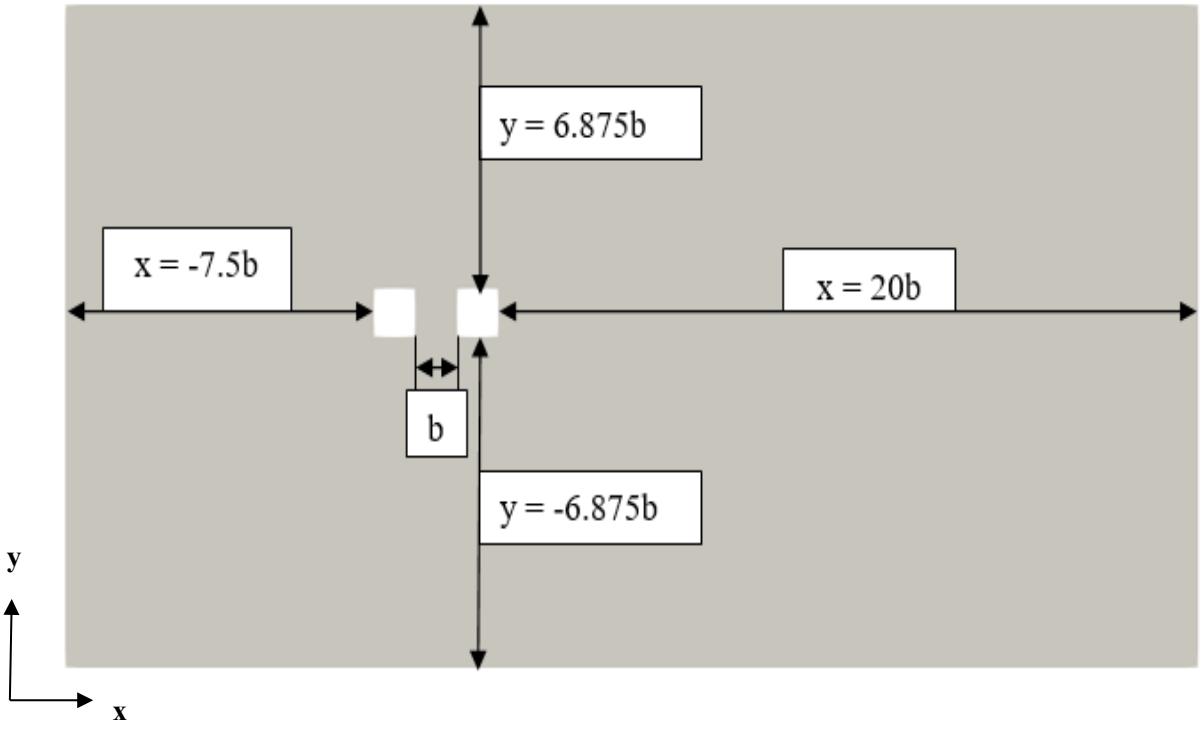

Figure 3.5: Computational domain with dimensions for the small building downstream case (Top view)

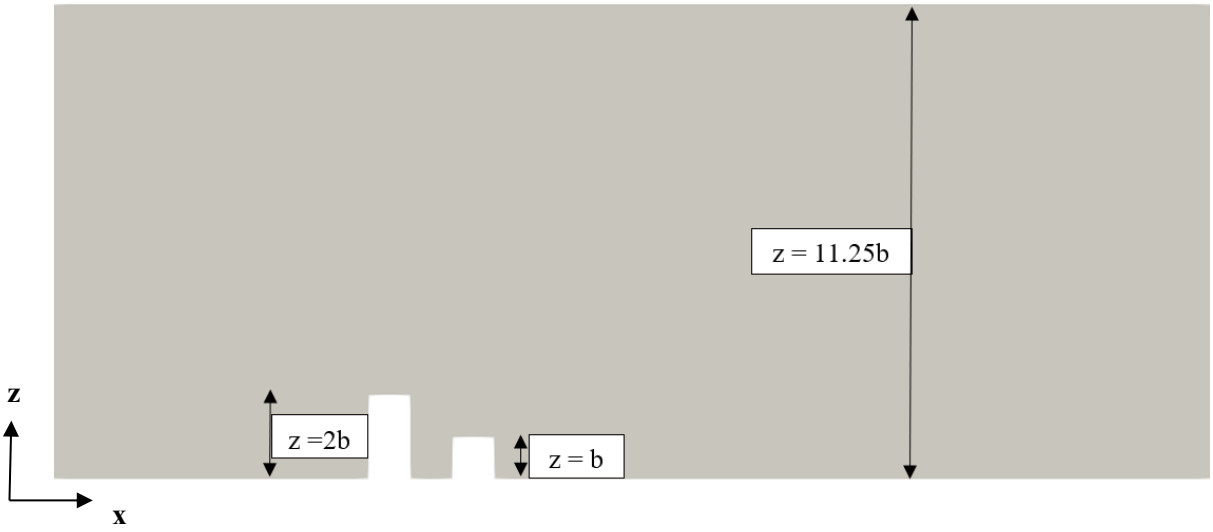

Figure 3.6: Computational domain with dimensions for the small building downstream case (Side view)

The computational domain in Figure 3.7 below, shows the small building placed in front or upstream of the tall building. Figure 3.8 and 3.9 illustrates the dimensions. The breadth is b, depth is b, and height is 2b for the tall building and the height of the small building is b, where b equals 0.08 m. The computational domain spans from x = -7.5b to x = 20b in the streamwise direction, y = -6.875b to y = 6.875b in the spanwise direction, and z = 0 to z = 11.25b in the vertical direction. The spacing between the two buildings is also denoted by 'b'. The overall number of grids is estimated to be around 1.72M for the coarse mesh.

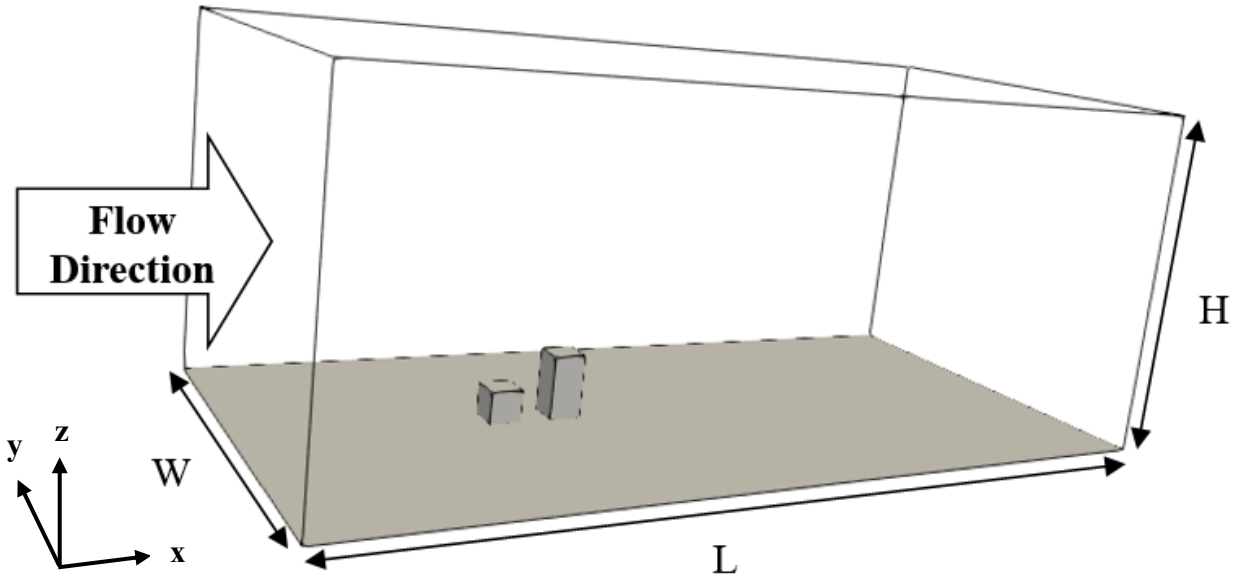

Figure 3.7: Schematic of the computational domain (Small building upstream)

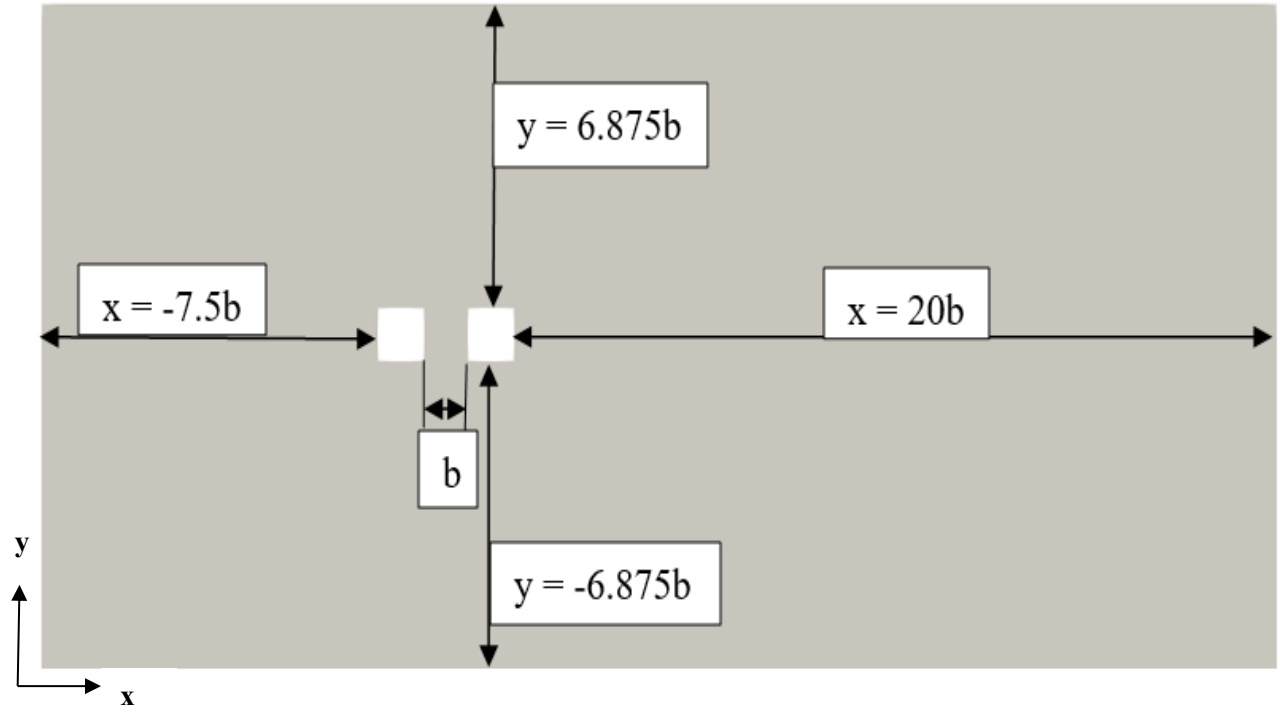

Figure 3.8: Computational domain with dimensions for the small building upstream case (Top view)

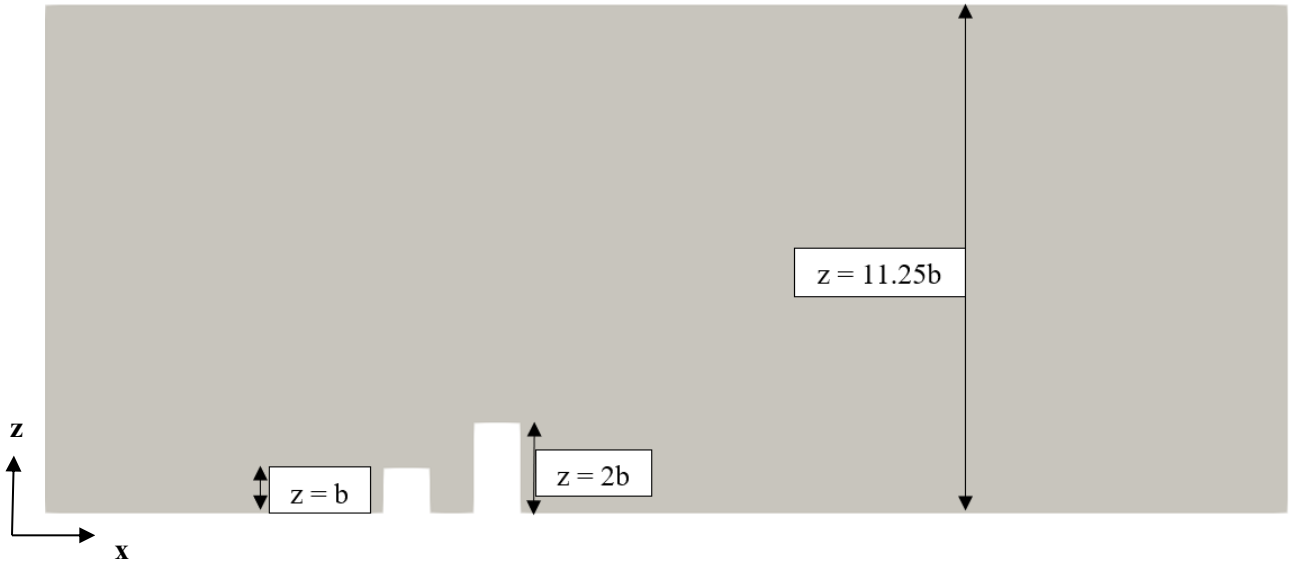

Figure 3.9: Computational domain with dimensions for the small building upstream case (Side view)

3.8 Boundary Conditions

Different boundary conditions set to a computational domain's boundaries allow fluid to flow in and out of the domain through the cells. Boundaries define the fluxes in a domain and control the movement of fluid within it [62]. Table 3.1 below depicts the boundary conditions of velocity and pressure. Atmospheric boundary layer (ABL) condition is used to handle the inlet boundary conditions, which provide log-law type ground-normal inflow boundary conditions for wind velocity and turbulence properties for homogeneous, 2D, dry-air, equilibrium, and neutral atmospheric boundary layer (ABL) modelling [63].

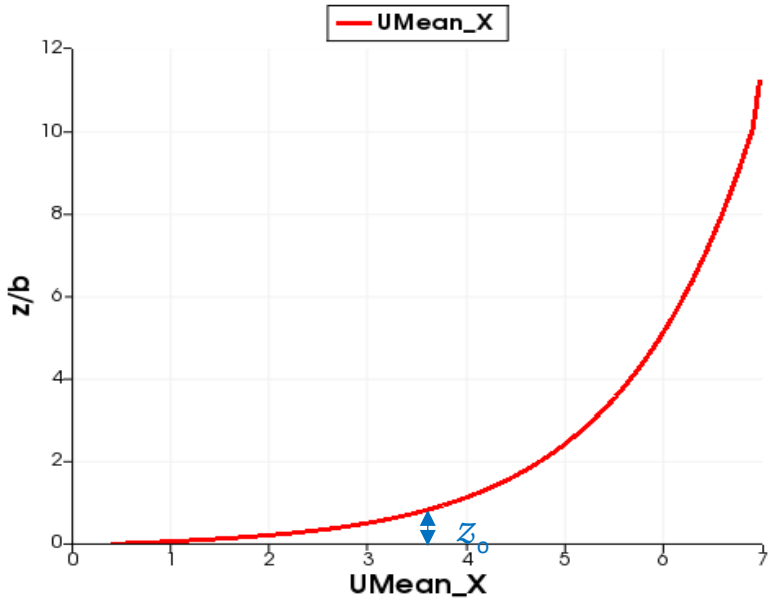

Figure 3.10: Inlet streamwise mean velocity

The time-averaged velocity profile using ABL inlet conditions is shown in the Figure 3.10, with z_0 being the roughness factor. The velocity profile agrees with the profile of Meng and Hibi's wind tunnel experimental setup. The reference for this study [37] implemented Kataoka et al. approach for setting up wind inflow conditions.

There are three forms of stratification in the atmospheric boundary layer: stable, unstable, and neutral. The first two represent the effects of temperature-related buoyancy, whereas neutral stratification is merely mechanical turbulence. Because neutral stability is associated with high wind speeds, buoyancy effects will not be considered in this research. In neutral conditions, the velocity profile follows the log law given by:

$$V(z) = \frac{u_*}{\kappa} \ln\left[\frac{z}{z_0}\right] \tag{3.22}$$

where u_* is the friction velocity, z is the height or vertical displacement, z_0 is the aerodynamic roughness length and κ is the Von Karman constant with range between 0.4 and 0.42. In this research, the value of z_0 is 0.005 m. The log law can be derived in a variety of ways, but the essential notion arises from the balance between the production of turbulent kinetic energy and the dissipation rate.

Another variant of the log law exists.

$$V(z) = \frac{u_*}{\kappa} \ln\left[\frac{z - d}{z_0}\right] \tag{3.23}$$

where d is the ground-normal displacement height. Other boundary conditions for the computational domain are sides, top, outlet and ground. Slip walls (zero normal velocity and zero normal gradients of all variables) are used to model the computational domain's sides and top. Neumann conditions are used on the outlet boundary, where zero static pressure is specified. Using the building height, H, and the velocity at z = H as reference values, the Reynolds number for the flow is 6.75×10^4. A rough wall was specified on the domain's bottom wall to model the effect of ground roughness.

Table 3.1 shows the boundary conditions for the three cases (single tall building, small building downstream and upstream of the tall building).

Table 3.1: Boundary conditions for the three cases

Boundary	**BC Type**	**Velocity**	**Pressure**
Stream-wise direction	Velocity Inlet	Atmospheric boundary layer inlet	Zero Gradient
	Pressure Outlet	Zero Gradient	$P_{gauge} = 0$
Sides (Span-wise direction	Slip (y = ±6.875b)	Free slip	Zero Gradient
Top	Slip (z =11.25b)	Free stream velocity	Zero Gradient
Bottom	No-slip (z = 0)	Wall boundary conditions	
Building/s wall	No-slip	Wall boundary conditions	Zero Gradient

Other parameters specified are υ and ρ, which are 1.54×10^{-5} m^2/s and 1.184 kg/m^3 at 25°C air. The numerical simulation was performed for the single tall building and twin building cases for 20 flow time. The simulation was run for four flow time so that flow can completely march the domain and then was later run for sixteen more flow time periods.

Figure 3.11 illustrates the computational domain with boundary conditions for the single tall building. Figure 3.12 illustrates the computational domain with boundary conditions for the small building downstream case while Figure 3.13 shows the computational domain with boundary conditions for the small building upstream case.

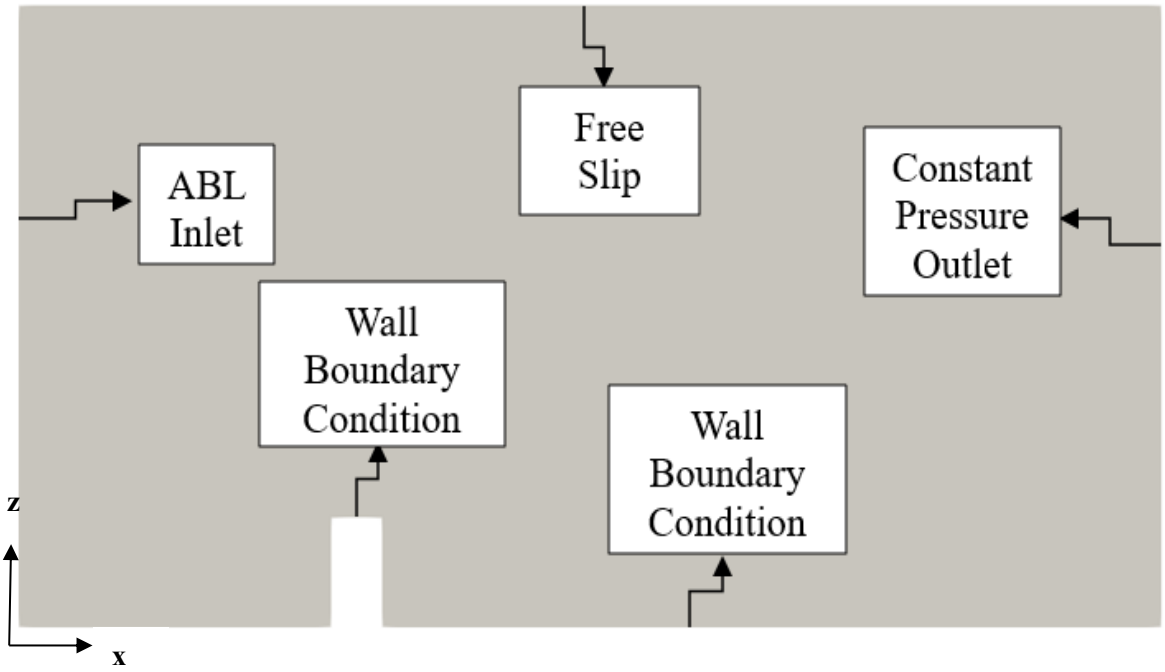

Figure 3.11: Computational domain with boundary conditions for single tall building (Side view)

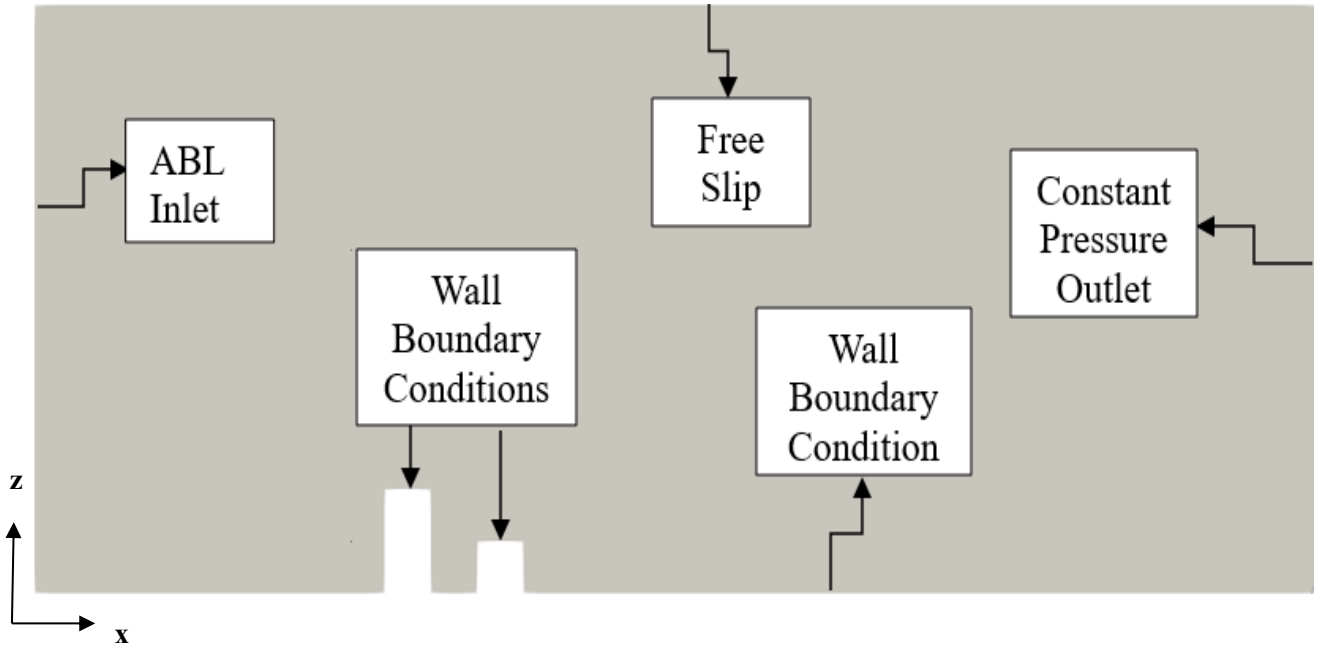

Figure 3.12: Computational domain with boundary conditions showing small building downstream (Side view)

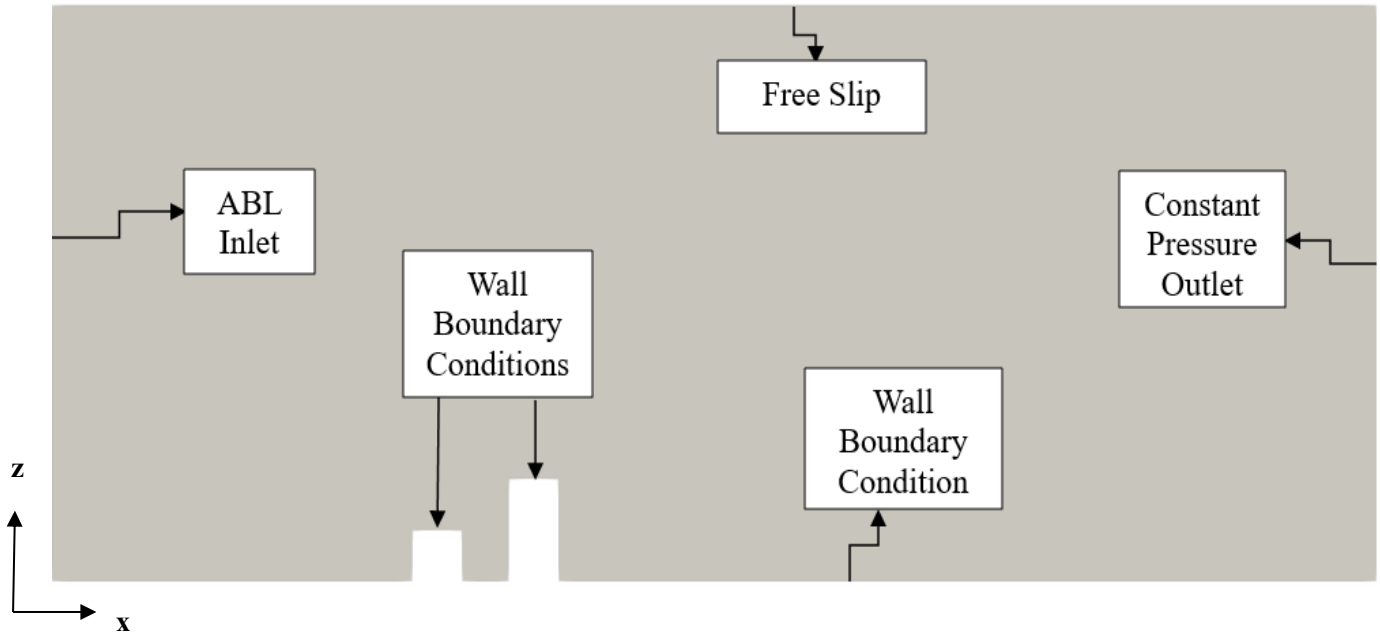

Figure 3.13: Computational domain with boundary conditions showing small building upstream (Side view)

3.8.1 CFD Modelling of ABL as an Inflow Boundary Condition

Roy & Bhargava [64] carried out investigation on CFD simulation of (ABL) atmospheric boundary layer wind flow around high-rise urban buildings with various configurations and wind incidence angles to observe the difference in wind velocity potential surrounding the buildings. Yan & Li [65] performed simulations of ABL flows using a novel method justifying the reduction of the atmospheric turbulence properties with height to avoid horizontal inhomogeneity. In addition, it is used to model the flows of ABL over a flat open terrain using comparisons with the experimental measurements, the numerical results were validated. Mohamed & Wood [66] defined a new eddy viscosity formulation for stagnating flows and to test its flow field prediction in a simulated atmospheric boundary layer (ABL) flow around a single rectangular tall building, including the downwind wake. Lamberti et al. [67] proposed a completely automated method for changing the turbulence generator's input parameters to get the desired turbulence statistics at the downstream position of interest. The specified inlet ABL develops through the domain, resulting in turbulence intensities that are sometimes too low.

3.9 Wake Refinement

To save computational cost, local grid refinement is employed to limit the most refined region to the wake as shown below [7]. Because of the changing filter width, which contradicts the commutation with differentiation assumption, this produces a commutation error that can produce errors on the order of the SGS stress (which requires a constant filter size). To mitigate the impact of this error, moderate levels of successive refinement are used to reduce abrupt filter width changes. The refinement boundaries are likewise placed away from the regions of direct interest (near the building and within the wake) because the error is highest at the refinement boundaries and decreases as the distance from the refinement boundaries increases.

OpenFOAM's native meshing application, snappyHexMesh was used to create a 3D mesh made up of hexahedra and split-hexahedra pieces. Using snappyHexMesh layering functionality, layers were added to the building walls and ground surface to make the mesh finer in these areas and for resolving near-wall gradients, keeping y^+ values between 0 and 1 for the mesh to capture wall effects.

Three different grids with hexahedral cells (1.67×10^6, 3.08×10^6 and 4.0×10^6) were used to simulate flow around the single tall building. The number of grids used for the small building downstream case are 1.73×10^6, 3.24×10^6 and 4.03×10^6. For the small building upstream case, the number of grids used are 1.72×10^6, 3.19×10^6 and 4.03×10^6. The grids are designed so that at the walls and the ground surface, the maximum value of y^+ is less than 1, allowing flow fluctuations associated with the separated flow to be captured. Using the grids above, grid independence study was conducted for the three cases in the results section.

Figure 3.14 shows the gradual wake refinement zones on cartesian hex mesh for the single tall building.

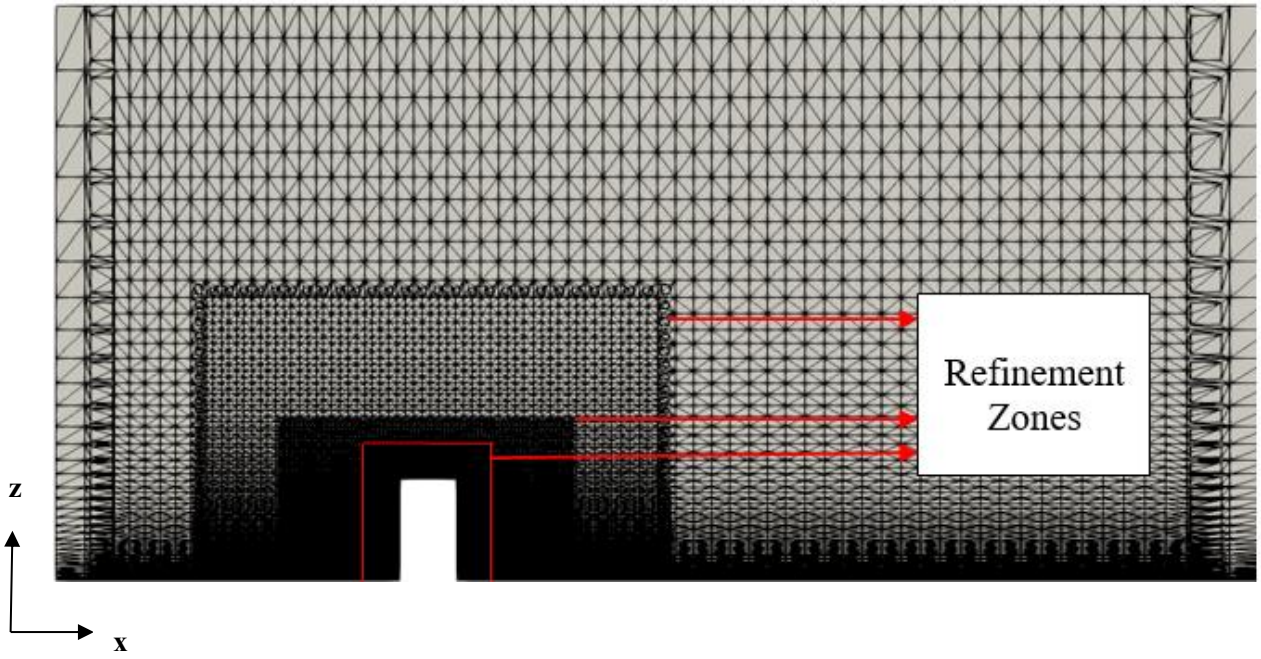

(a) Side view, x-z plane

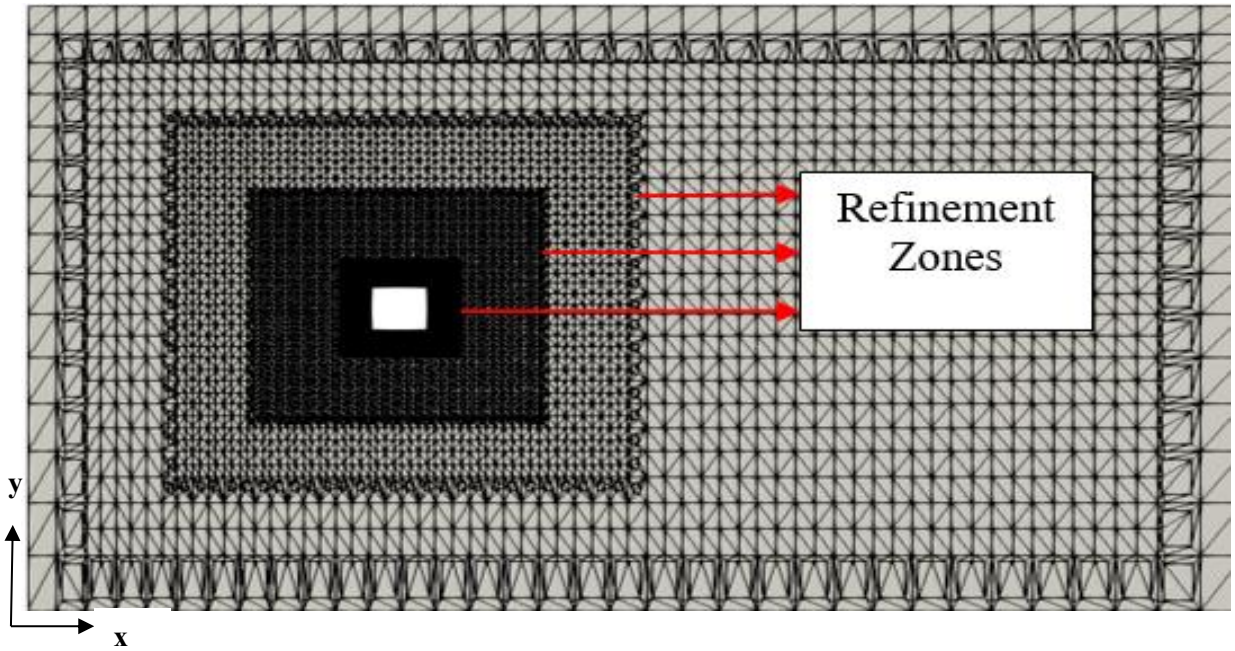

(b) Top view, x-y plane

Figure 3.14: Gradual wake refinement zones on cartesian hex mesh for the single tall building (a). Side view (b). Top view

Figure 3.15 shows the gradual wake refinements on cartesian hex mesh for the small building downstream case.

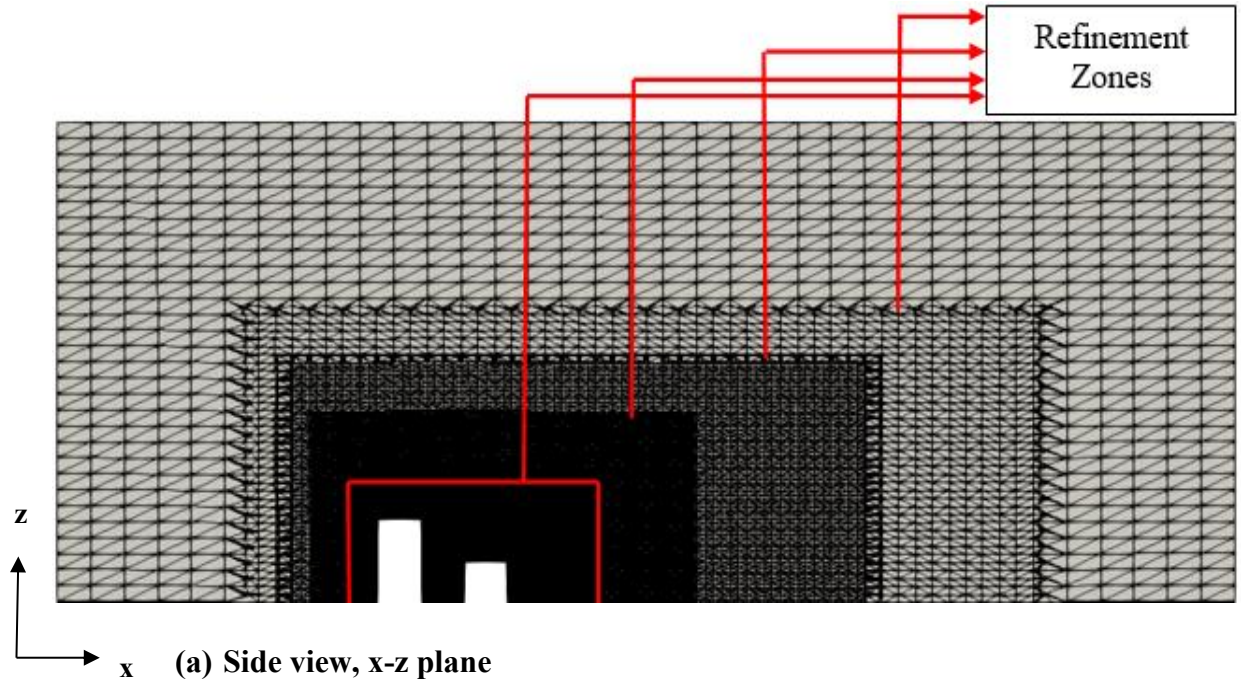

(a) Side view, x-z plane

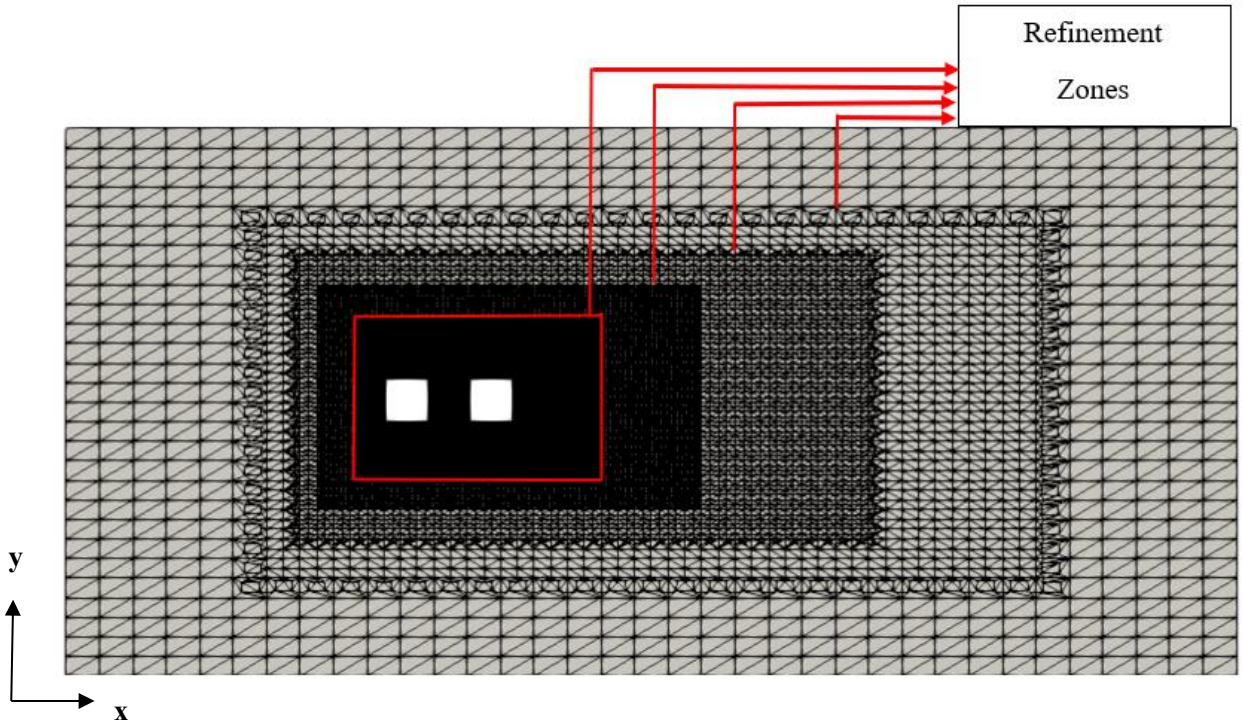

(b) Top view, x-y plane

Figure 3.15: Gradual wake refinement zones on cartesian hex mesh for the small building downstream case (a). Side view (b). Top view

Figure 3.16 shows the gradual wake refinements on cartesian hex mesh for the small building upstream case.

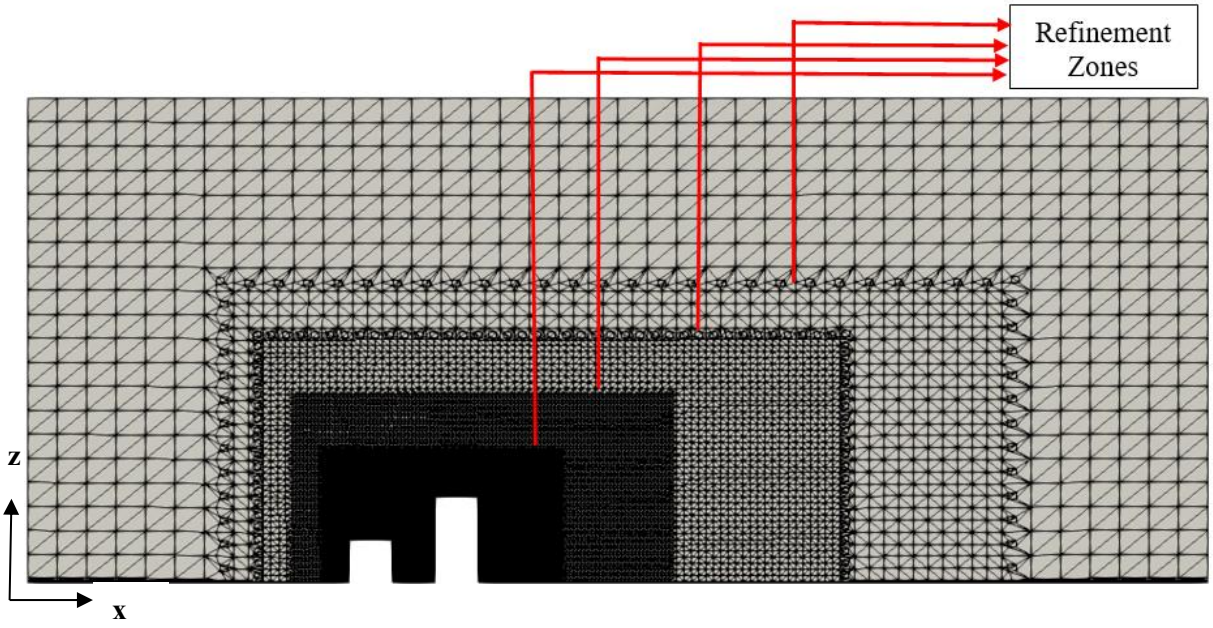

(a) Side view, x-z plane

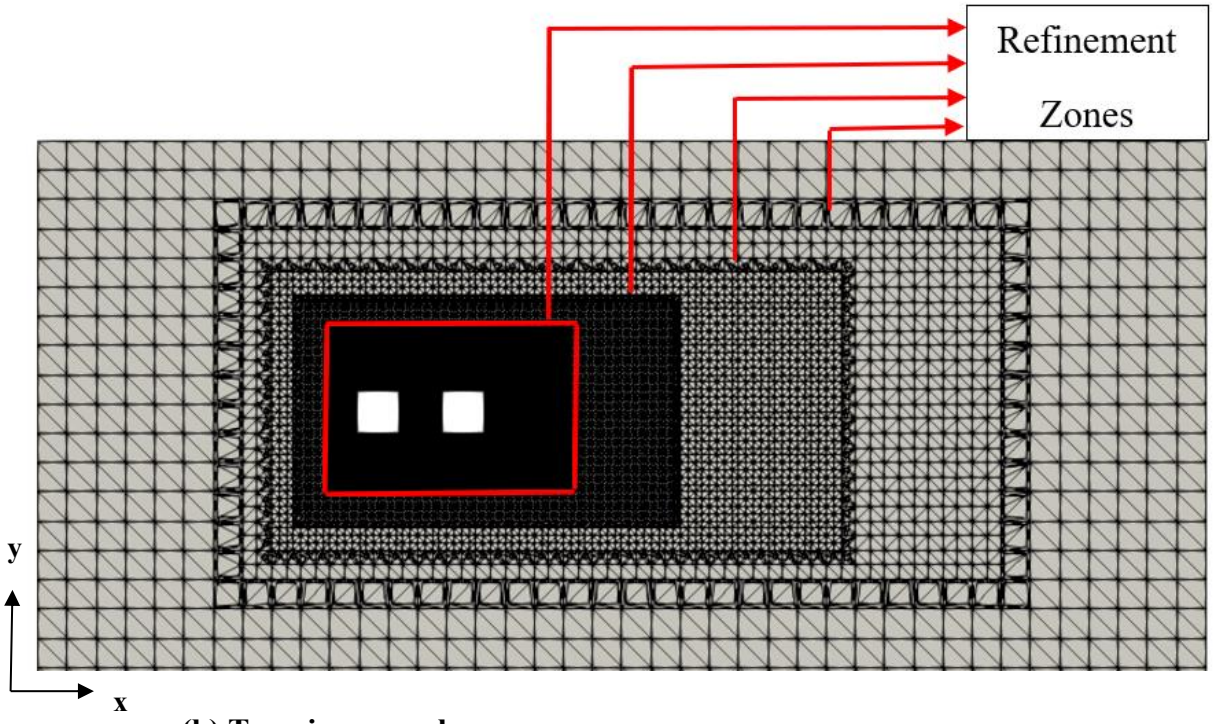

(b) Top view, x-y plane

Figure 3.16: Gradual wake refinement zones on cartesian hex mesh for the small building upstream case (a). Side view (b). Top view

Chapter 4

WIND CONDITIONS OVER A SINGLE TALL BUILDING

4.1 Introduction/Preamble

This chapter focuses on the study of wind conditions over a single tall building. Large eddy simulation is used to study the wind effects around the single tall building. In addition, the results obtained from the simulation is used for validation purposes with Meng and Hibi's wind tunnel experimental results [61]. The model and reference used for this chapter are obtained from Kono and Kogaki [37] to gain a better understanding of the fluid and wake dynamics around a single tall building. Wind flow around the single tall building is studied to better understand the fluid dynamics, wake dynamics, and flow structures around the tall building. To better understand the wake dynamics, models used by Tutar and Oguz [9] and Wang et. al [21] which illustrate wake flow structures around a building and the wake model of a wall-mounted cylinder respectively are used to compare wake dynamics and flow structures obtained in this chapter. It is important to study wind flow around a tall building because wind is extremely sensitive around tall buildings and wind flow changes continuously because of building corners, uneven surfaces, and high wind speeds. Therefore, LES can predict the effects of turbulence, vortex formation and measure the effects of wind pressure on the building's stability and safety. As a result, wind load assessments are required to design these tall buildings which also create a negative effect on the environment by disrupting the movement of pedestrians in the building's vicinity.

4.2 Numerical Validation for the Single Tall Building

Time-averaged velocity profiles are chosen to validate the LES results against the results of the Meng and Hibi [61] wind tunnel experiment. Time-averaged velocities are used for validation because LES generates results instantaneously and the results obtained from the wind tunnel experiment are average values. Velocity profiles at the mid-point of the building using three grids are chosen for the grid independence study. A grid independency study is conducted to analyze

the suitability of the mesh to obtain an estimate of the numerical error in the simulation. Grid independence study is first conducted to validate the LES results of the single tall building with results from Meng and Hibi's wind tunnel (WT) experiment to ensure the results are reliable and the numerical setup is correct. To ensure adequate grid resolution, a grid-dependency study also needs to be carried out. The grid-independency is checked using three levels of meshes, each having various grid points, as shown in Table 4.1. Three sets of meshes are denoted by level-1, level-2, and level-3 were used to illustrate grid-independency of the numerical results. With level-1 being the coarse mesh and level-3 being the most refined mesh. The greater the number of grids, the longer the simulation time as seen from Table 4.1.

Table 4.1 shows a comparison of the outcomes for the three meshes.

Table 4.1: Validation and grid independence study for the single tall building

Mesh name	**Number of nodes (x 10^6)**	**CPU Hours**	**Time step (Δt)**
Level-1 (Coarse)	**1.67**	**2 weeks**	**2e-5**
Level-2 (Medium)	**3.08**	**3 weeks**	**3e-4**
Level-3 (Fine)	**4.0**	**3 weeks 4 days**	**1e-4**

Table 4.1 shows the mesh resolution and increasing the cell number from meshes I to III, it is expected that the results will not change if the grid is increased. Different time steps are used for different grid resolutions to ensure that the maximum Courant- Friedrichs-Lewy (CFL) number is average of 0.8 in all cases. This improves both temporal accuracy and numerical stability.

A grid independence study is conducted for the three grids using the tip of the building's mid-point to the top of the fluid domain. Figure 4.1 shows the velocity profiles at the mid-point of the building with the three grids.

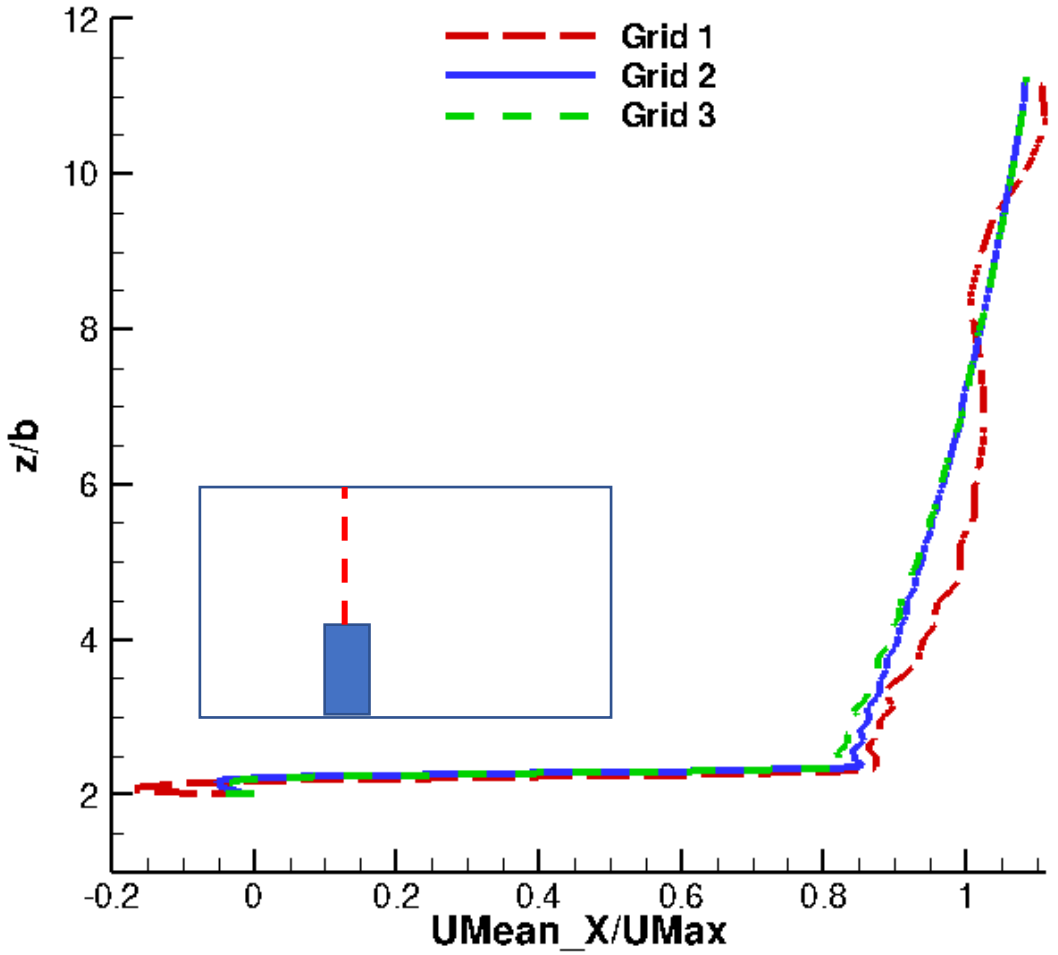

Figure 4.1: Velocity profiles showing grid independence study for the single tall building

The time-averaged or mean velocities of the LES data are compared to those of Meng and Hibi's wind tunnel (WT) experiment as shown in Figure 4.2 ad 4.3. All verification and validation comparisons are made using three vertical lines upstream of the building, one symmetry plane and two horizontal lines downstream of the building. The time-mean velocities are obtained using vertical profiles in the x-z plane, and these were first considered using vertical profiles denoted by the dashed line, in front or upstream of the building at a farther distance and then distances closer to the building were then considered. Distances downstream of the building are then considered by first extracting vertical profiles in proximity to the building and then farther away from the building.

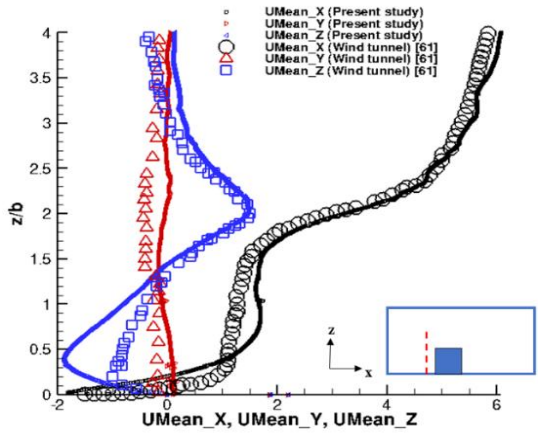

(a) x/b = -0.75

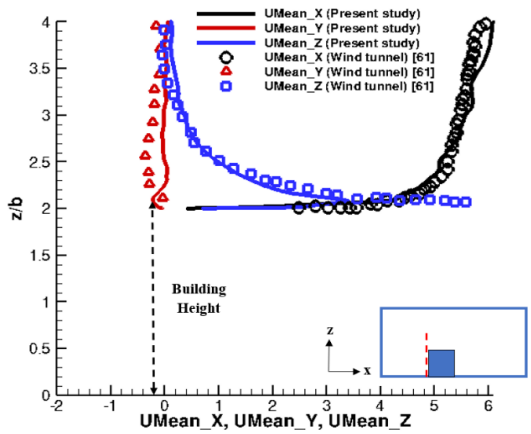

(b) x/b = -0.5

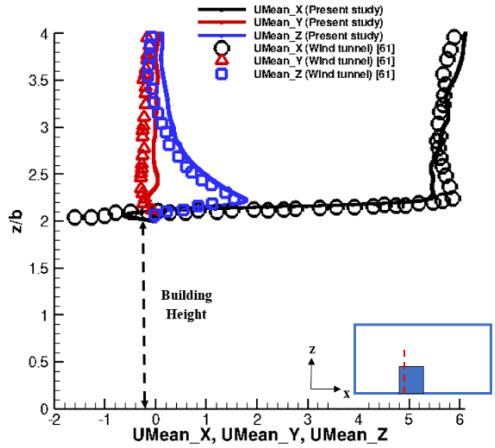

(c) x/b = -0.25

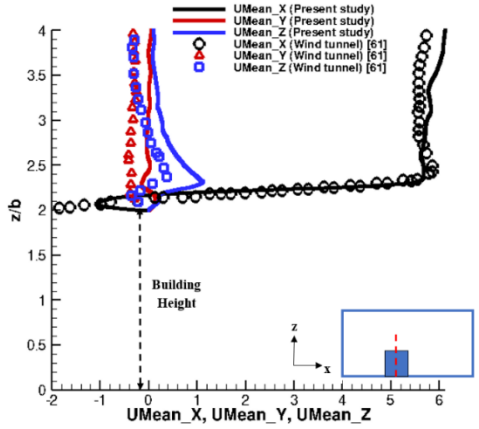

(d) x/b = 0

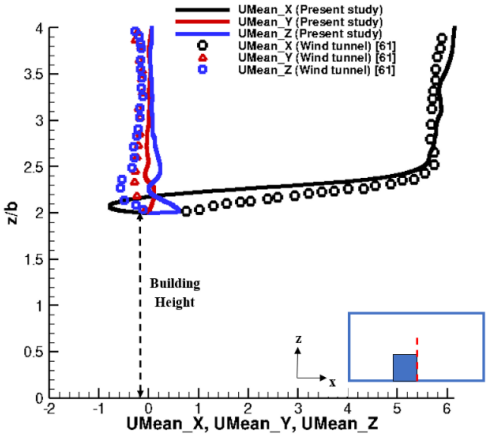

(e) x/b = 0.5

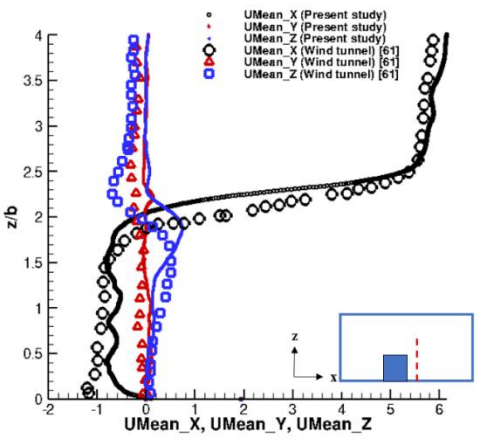

(f) x/b = 0.75

Figure 4.2: Vertical profiles of simulated and observed [61] time-mean velocities (y = 0).

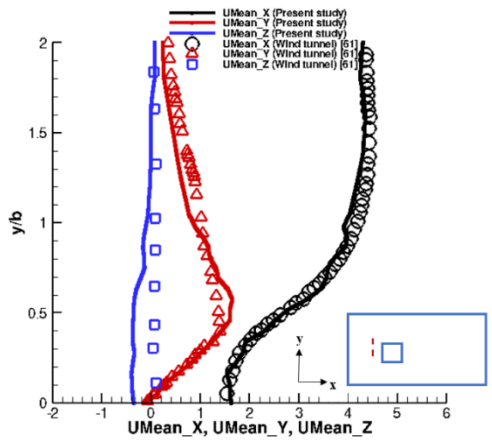

(a) x/b = -0.75

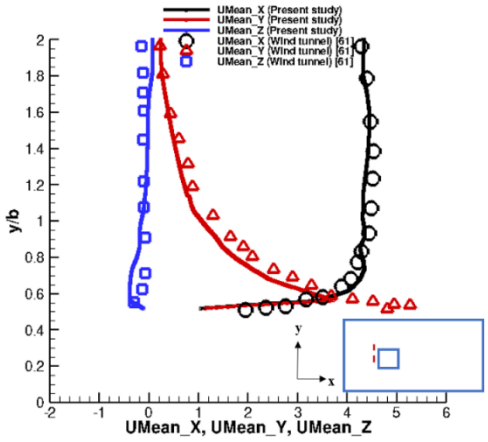

(b) x/b = -0.5

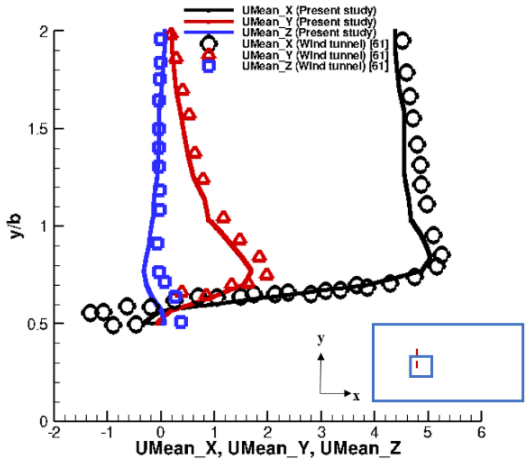

(c) x/b = -0.25

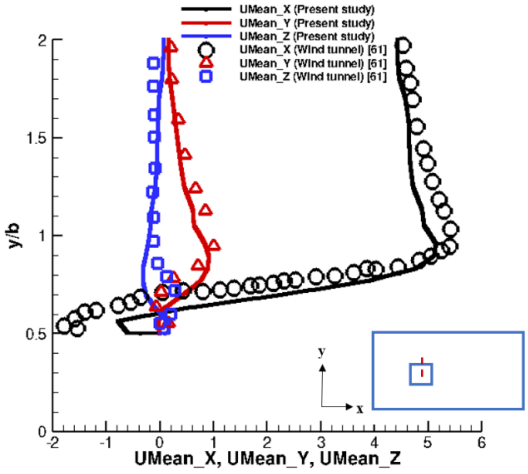

(d) x/b = 0

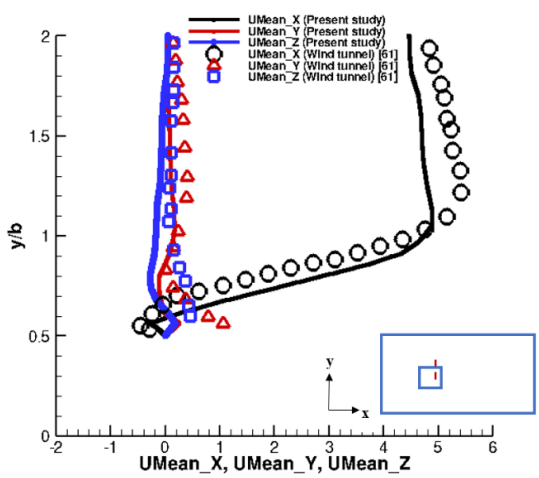

(e) x/b = 0.5

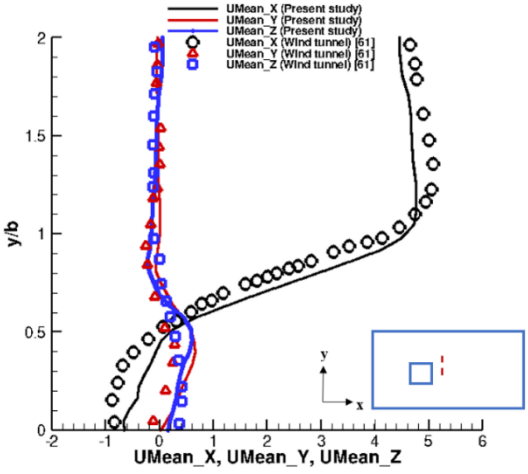

(f) x/b = 0.75

Figure 4.3: Horizontal profiles of simulated and observed [61] time-mean velocities (z = 1.25b).

The LES results over the building in the x-z plane at y = 0 closely matches with those of the wind tunnel experiment both qualitatively and quantitatively. These results are in good agreement with WT measurements in the x-z plane at x/b = 0.75 (inflow region) and 0.75 (wake region), and in the x-y plane at z/b = 1.25.

The simulation results match well the experimental data. As a result, the LES can be said to be successful in accurately replicating the turbulent flow field over the building. There were some deviations in the mean velocities, and this is because the simulation was conducted for a shorter time than the total duration used in the experiment. This was done due to a lack of computational resources and the time-consuming nature of LES.

4.3 Pressure and Velocity Distribution around the Single Tall Building

Wind flow produces velocity and pressure fields around buildings [68]. The pressure distribution around a building immersed in a moving fluid is a function of the velocity of the fluid around the body (air pattern), which is a function of the geometry of the body, the kinematic characteristics of the fluid (velocity-height distribution), and the fluid properties. Therefore, pressure distribution on building walls depends on the velocity distribution. When airflow strikes a building, it creates several distinct zones on the walls and in the surrounding area, which appear as vortices and local acceleration [69].

The mean pressure fields are used in illustrating the effect of wind flow over the building. The mean pressure fields show pressure distribution around the building while the mean streamlines are used in flow visualization to show various flow features such as stagnation at the leading edge of the building, flow separation, standing vortex, recirculation, reverse flow, and reattachment on the roof of the building which were captured using LES.

The mean pressure fields are investigated in this section by looking at time-averaged streamlines and pressure contours in two characteristic planes (symmetry plane and mid-span plane).

4.3.1 Pressure Fields on the Symmetry Plane

Figure 4.4 shows the pressure contours on symmetry plane (y/b = 0) plane.

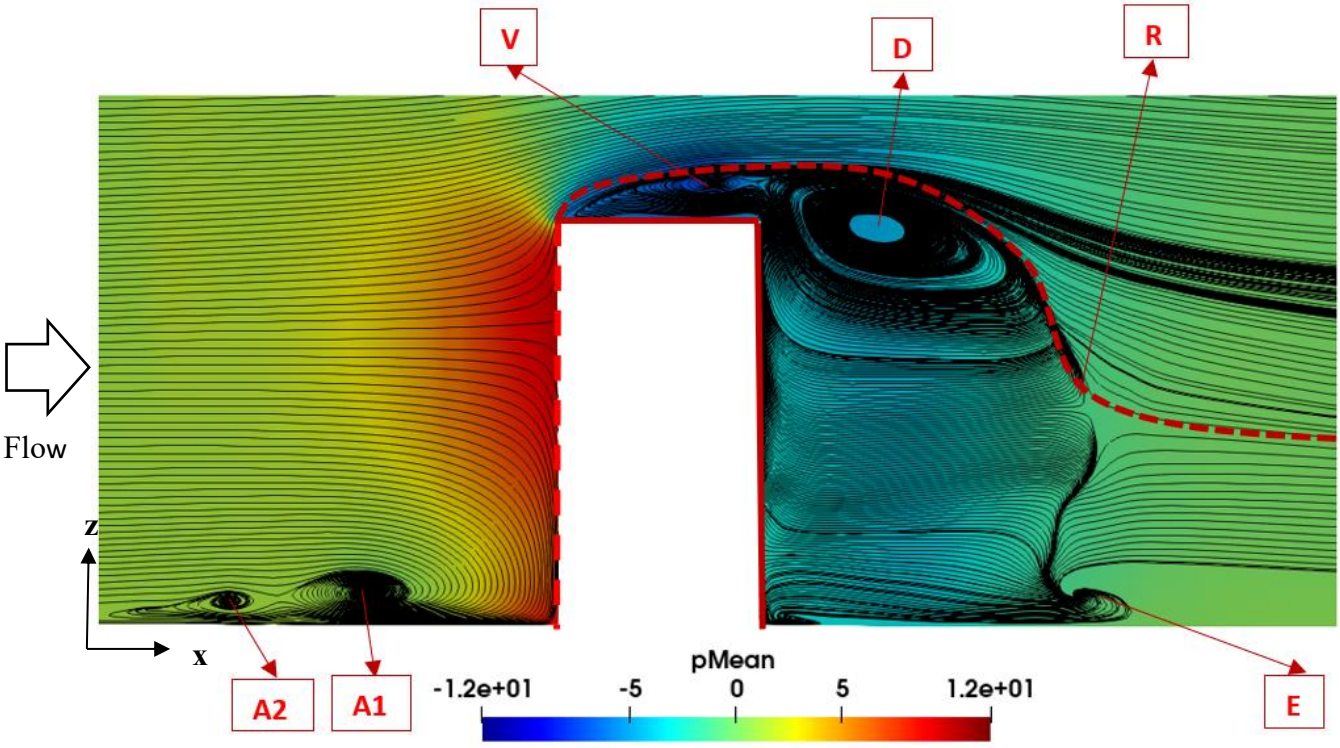

Figure 4.4: Pressure fields on the symmetry plane at y/b = 0 (V = Top-face bubble, D = Side-face bubble/downwash recirculation zone, R = Impingement point, A1 & A2 = Standing vortices /Horseshoe vortex spiral nodes, E = Upwash induced flow, Dashed red line = Separating line between the outer zone and the influence region of the backflow).

In Figure 4.4, a negative pressure is observed behind the building or downstream of the building in the wake region because of the high Reynolds number. The stagnation point at the leading edge of the building is observed [9], where the horizontally and vertically streamlines are separated. Both reverse and reattachment flows are observed on the roof of the building. Reverse flow occurs at the windward face of the building close to the ground (also known as standing vortices) denoted by A1 and A2. Because of the sharp edge of the building at the leading edge, flow separation occurs. The flow gets separated at the front corner of the building and this flow stagnation creates a reversed flow at the base of the building denoted by A1 and A2. The vortices appear near the corner of the building and the accumulation of these vortices results in a recirculation zone behind the building. The dashed red line at the wake represents the separating line between the outer zone

and the influence region of the backflow, which originates from the leading corner of the building. The separating line in the symmetry plane, in fact, directly reflects the strength of the downward flow from the tip (i.e., downwash) and so plays a significant role in the formation of flow structures [70]. It can be observed that because of the relatively weak downwash, the separation line cannot reach the ground. The impingement point (shown by capital R) is formed which occurs above the base. As a result, an obvious upward flow (defined as the upwash by Wang et al. [21]), which comes from the source point E and clashes with the downwash along the x- direction is formed. This upwash flow has a significant influence on several aspects of the flow field, including the mean streamwise vortices. A side separation bubble or downwash recirculation zone (D) close to the leading edge is formed on the building's mid-plane, which does not extend into the outer wake. According to Wang & Zhou [25] model, the reattachment on the building's upper or top face is stationary and does not contribute to the tip structure that forms on the building's rear. Top-face bubble denoted by "V" appears on the building's mid-plane (y/b = 0). In other words, bubbles are formed on both the top and side faces of the building.

Flow separation points, downwashes on windward walls, recirculation behind buildings are all flow features associated with wind flow around tall buildings. In addition, a separated shear layer from the upper junction of the leading edge indicated by the dotted line, produces downwash flow in the near wake region, while the horseshoe vortex and reversed flow in the wake leads to the upwash induced flow denoted by E. Two horseshoe vortex spiral nodes denoted by A1 and A2 were formed upstream of the building. The tip and base vortices were responsible for downwash and upwash flows. The downwash and upwash flows were also attributed to the special features of finite wall-mounted cylinders (FWMCs), such as lower drag when compared to infinite cylinders [26]. The spanwise flow is also highly influenced by Re. In the mean streamline in figure 4.4 above, the upwash flow has a major impact on the bottom recirculation region. Because of the significant upwash change, the flow is pushed closer to the wall by the increased downwash strength. The downwash has a penetration of around 0.08 m along the building's height.

4.3.2 Pressure Fields on the Mid-Span Plane

Figure 4.5 illustrates the pressure contours on the mid-span plane (z/b = 1). Two symmetrically distributed spiral nodes (A and B), which represent the time-averaged horseshoe vortex spiral

points on the symmetry plane (y/b = 0) are observed [70]. The streamlines are not perfectly symmetric because the flow is transient.

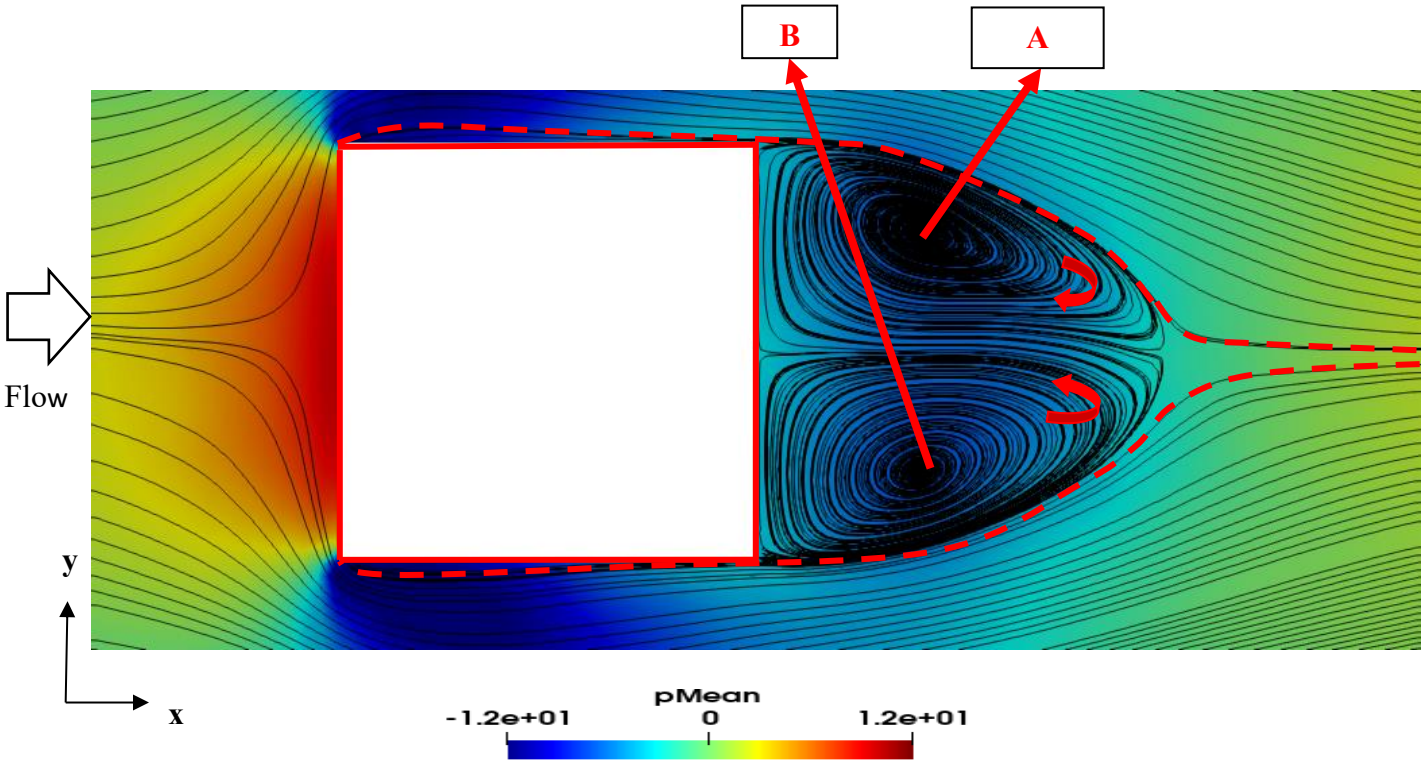

Figure 4.5: Pressure fields on the mid-span plane at z/b = 1 (A and B = Spiral nodes).

4.3.3 Velocity Fields around the Single Tall Building

Figure 4.6 shows the instantaneous distribution of streamwise velocity (U_x) at the symmetry plane (y/b = 0) while Figure 4.7 shows the streamwise velocity vector on the z-x plane at the symmetry plane (y/b = 0). Velocity vector is used to visualize wind flow direction and its effects around the building, and visualizing information of the wake structures.

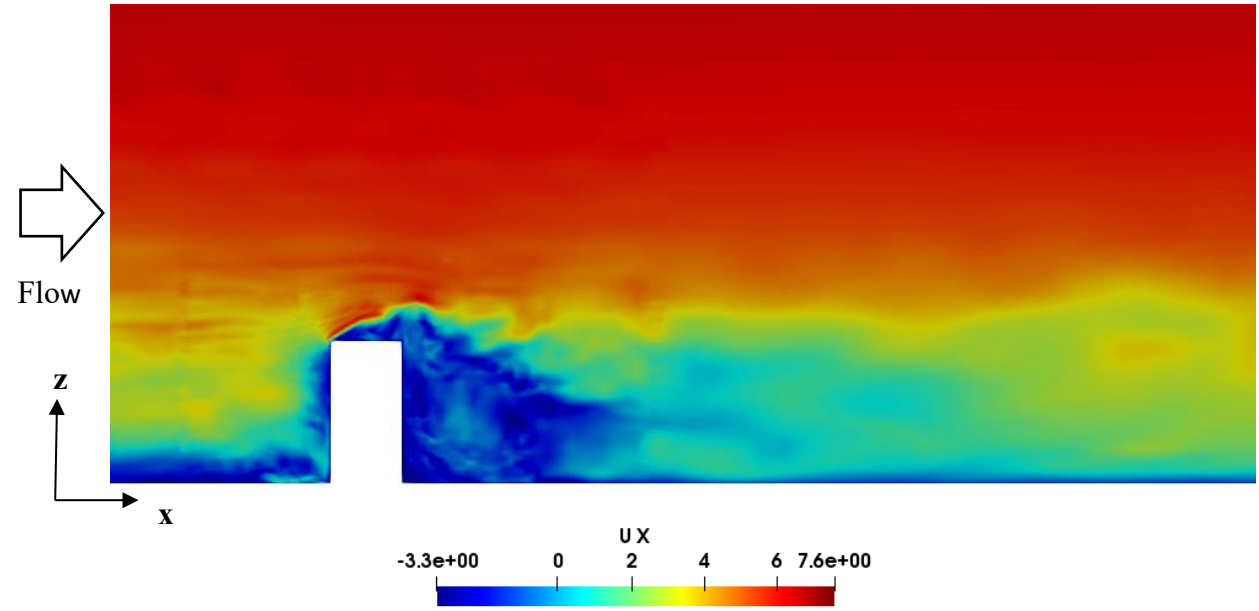

Figure 4.6: Instantaneous Streamwise Velocity (x-velocity, U_x)

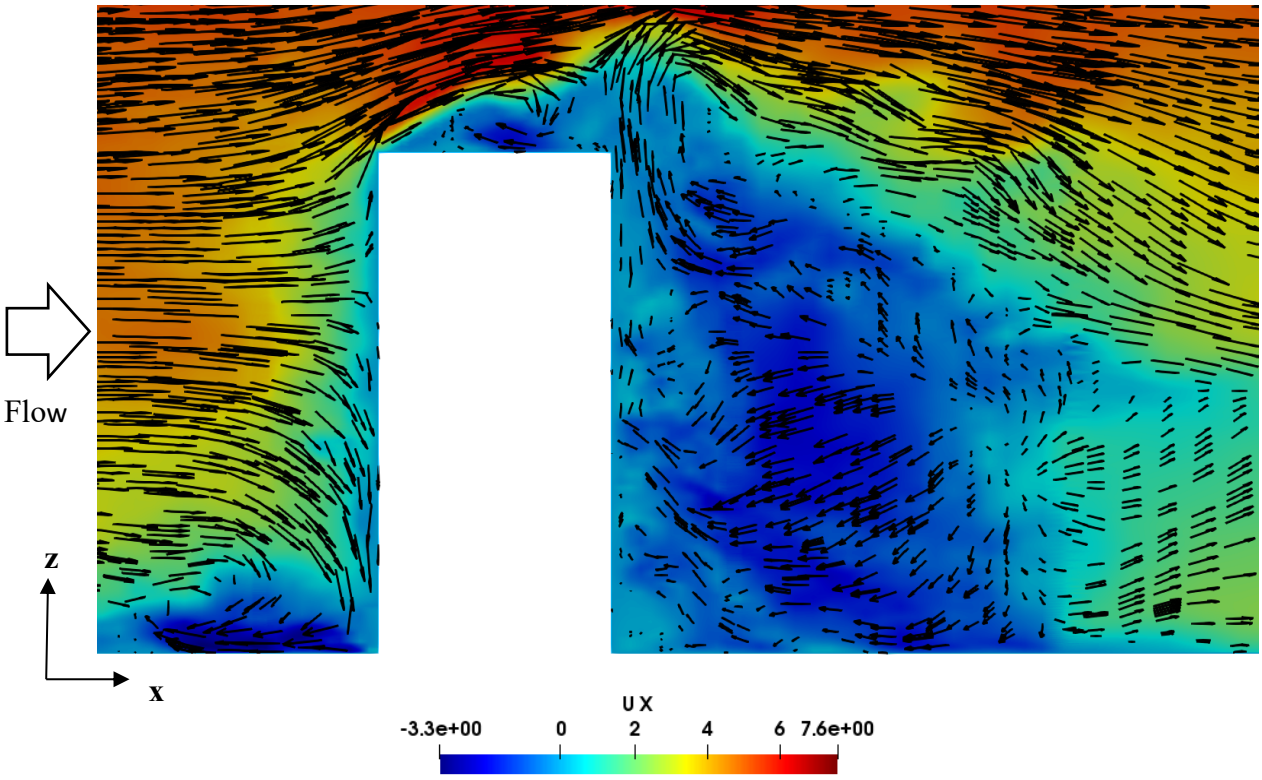

Figure 4.7: Vertical distribution of streamwise velocity vector

This illustrates how velocity from inflow wind conditions upstream of the building reduces as it approaches the building. We observe that the walls of the building in the windward and leeward

regions had negative velocity but further downstream when the effect of downwash flow becomes reduced, the velocity increases again. The ground effects are also visible as seen from the negative velocity on the ground level. From the tip of the building to the top of the domain, wind flow is uniform, and the velocity is at its peak. But wind flow becomes chaotic as it gets closer to the walls of the building. Lower streamwise velocity shows a stationary zone or a recirculation zone, which is commonly visible behind buildings.

4.4 Wake Flow Structures

Figure 4.8 illustrates the isosurfaces of Q-criterion in the far wake from the side and top faces of the building. The transverse instantaneous tip vortex, streamwise instantaneous tip vortices, mean streamwise tip vortices, and mean streamwise base vortices are not included in this model. From figure 4.8, the wake flow is unsteady and vortex shedding occurs at the flow's Reynolds number of 6.75×10^4.

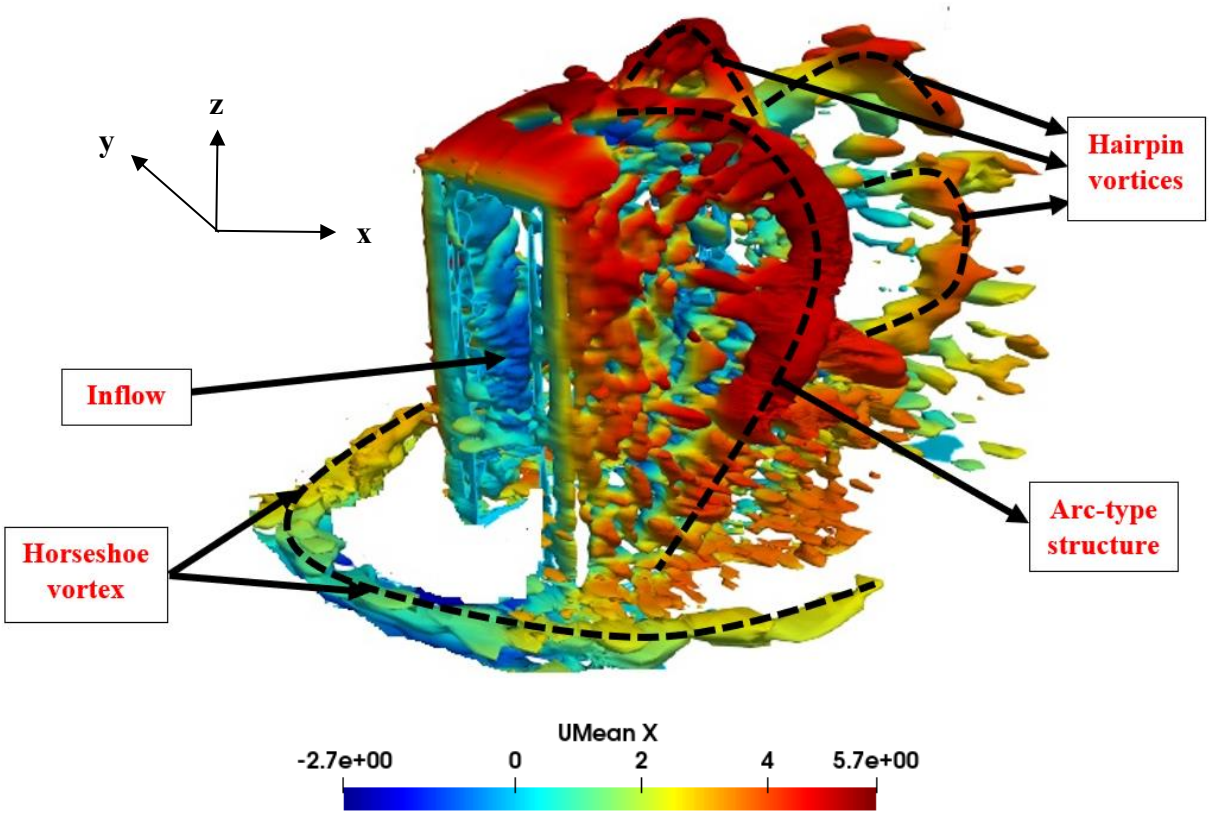

Figure 4.8: Isosurface of Q=10,000 colored with mean streamwise velocity (Side view).

The “legs” shed from the two sides of the building exhibit the “C” shape in the early stages of spanwise vortex development, so both the upper and lower parts of the vortex cores are inclined towards the downstream direction. However, when the distance from the building increases, the profile of the spanwise vortices transforms to a “Reverse-C” shape, which is defined by the inclination of the two ends of the vortex which rolls towards the upstream direction and then bends towards the center plane. Because of the turbulence caused by interactions between the downwash, the shear layer, and the boundary layer, the “Reverse-C” type of vortices transitions to the “Hairpin” type of vortices with the fragmentation of huge chunks of vortex structure in the further downstream region. In the mid- and far-wake of the building, hairpin vortices form and are shed periodically. The interaction of upwash, downwash, and shear layers causes an increase in wake instabilities, which causes hairpin vortices to form [26]. Because of the high Re, the degree of fragmentation increases further downstream [70].

More significantly, the separated shear layer from the building’s leading edge is connected to the wake structures, which is consistent with Wang’s existing model [25]. The legs of the horseshoe vortex are also extended into the wake, interacting with the structure generated behind the building. This can have a direct impact on the dynamics of the wake. The building’s wake structure, on the other hand, is only a short distance from the legs of the horseshoe vortex.

4.5. Structure of Vortices at Various Planes in the Streamwise Direction

Mean streamlines at the near-wake, mid-wake and far-wake are used in this study to gain an understanding of vortex structure evolution at the wake region of the building. The mean streamlines for several z-y planes (x/b = 1.25, 6.25 and 12.5) are illustrated in Figure 4.9 to gain a better understanding of the vortex structure evolution at the wake of the building.

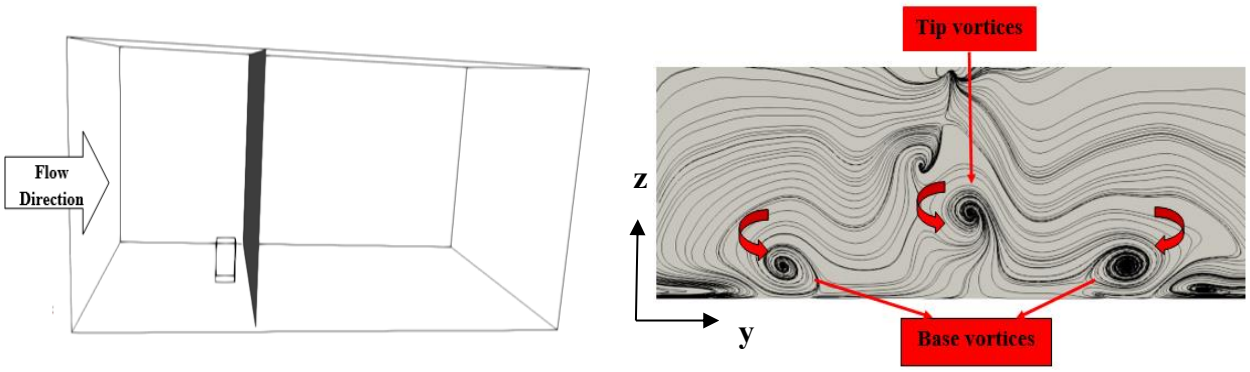

(a). x/b = 1.25

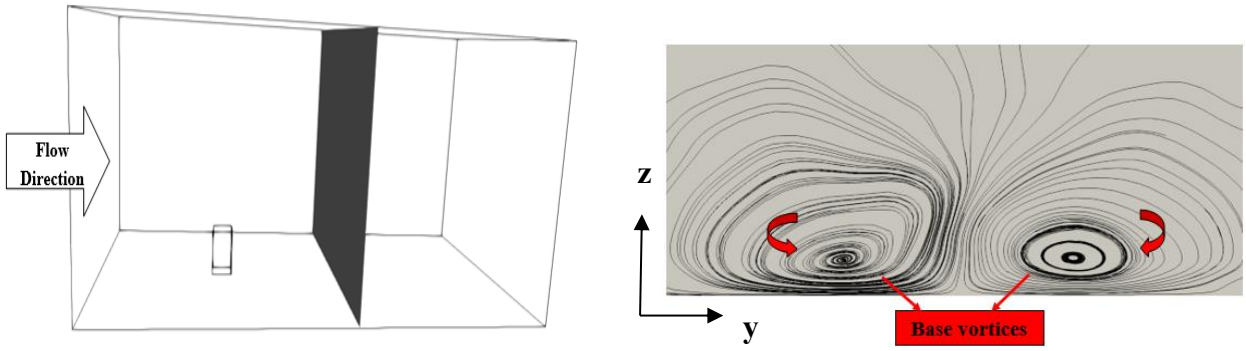

(b). x/b = 6.25

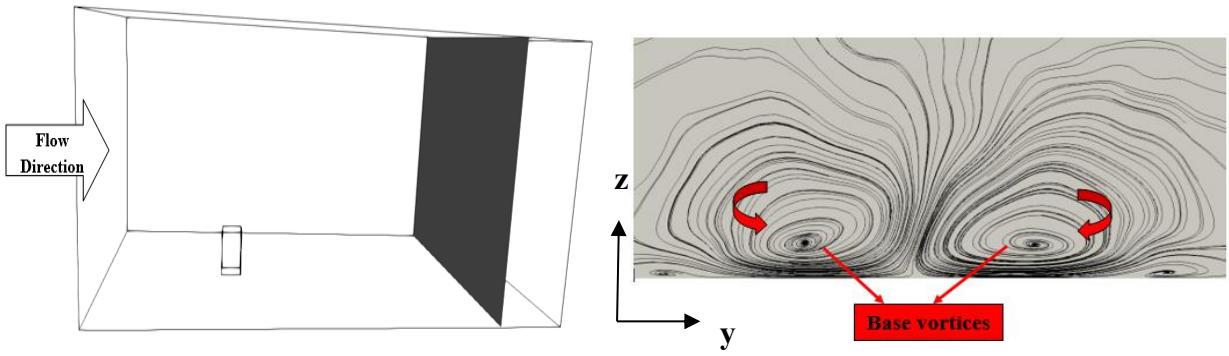

(c). x/b = 12.5

Figure 4.9: The evolution of time-averaged streamlines between the near and far wakes. (a) x/b = 1.25; (b) x/b = 6.25; (c) x/b = 12.5.

Figure 4.9 illustrates the mean/time-averaged streamlines vortices in the wake. The mean streamwise tip vortices are caused by the downwash flow from the building's tip. The mean streamwise base vortices caused by upwash flow from the base is also formed. The upward flow dominates the streamwise planes situated within this region, and two pairs of counter-rotating time-averaged base vortices are formed close to the ground of the building. The two pairs of counter-rotating vortices generated because of the bending of the mean streamlines in the lower part are induced by the upward flow from the base.

At the near wake region of x/b = 1.25, base vortices and tip vortices are formed. The base vortices have the opposite sense of rotation as the tip vortices, which decays as x/b moves further downstream. The tip vortices disappear further downstream of the building in the far wake region. In addition, the base vortices further downstream grow. At the far wake from x/b = 6.25 to 12.5, only one pair of vortices lead to the downwash flow, as shown in the streamlines above. Based on the Re effect on the presence of Karman vortex shedding, there is no Karman vortex shedding for $Re \leq 75$, but there is Karman vortex shedding for $Re \geq 85$. As a result, perhaps the wake type is determined by the existence or absence of asymmetric vortex shedding in a building's wake.

Further downstream, the strength of the upwash is large enough to counter the effects of the downwash, with the base vortices having the opposite direction of rotation. The mean streamwise base vortices dominate the plane. Also, the counter-rotating tip vortices earlier formed disappears. Although, the mean streamwise tip/base vortices which are respectively induced by the downwash from the building's tip and the upwash near the bottom wall serve as the constituent parts of several existing vortex models, they can only be observed at some distance from the buildings and are meant for the time-averaged flow field. The flow separation effect caused by the tall building is identified at the ground surface where the streamlines form a horseshoe vortex.

4.6 Spanwise Structures

Contours of spanwise vorticity at various spanwise locations (close to the ground surface, at the mid-span, and close to the tip of the building) are used to illustrate the effects of vortex shedding at the wake region of the building. Figure 4.10 shows different spanwise locations considered in

illustrating the effects of vortex shedding using spanwise vorticity at the wake, while Figure 4.11 shows the contours of the spanwise vorticity at various spanwise locations (z/b = 0.625, 1 and 1.875) of the building.

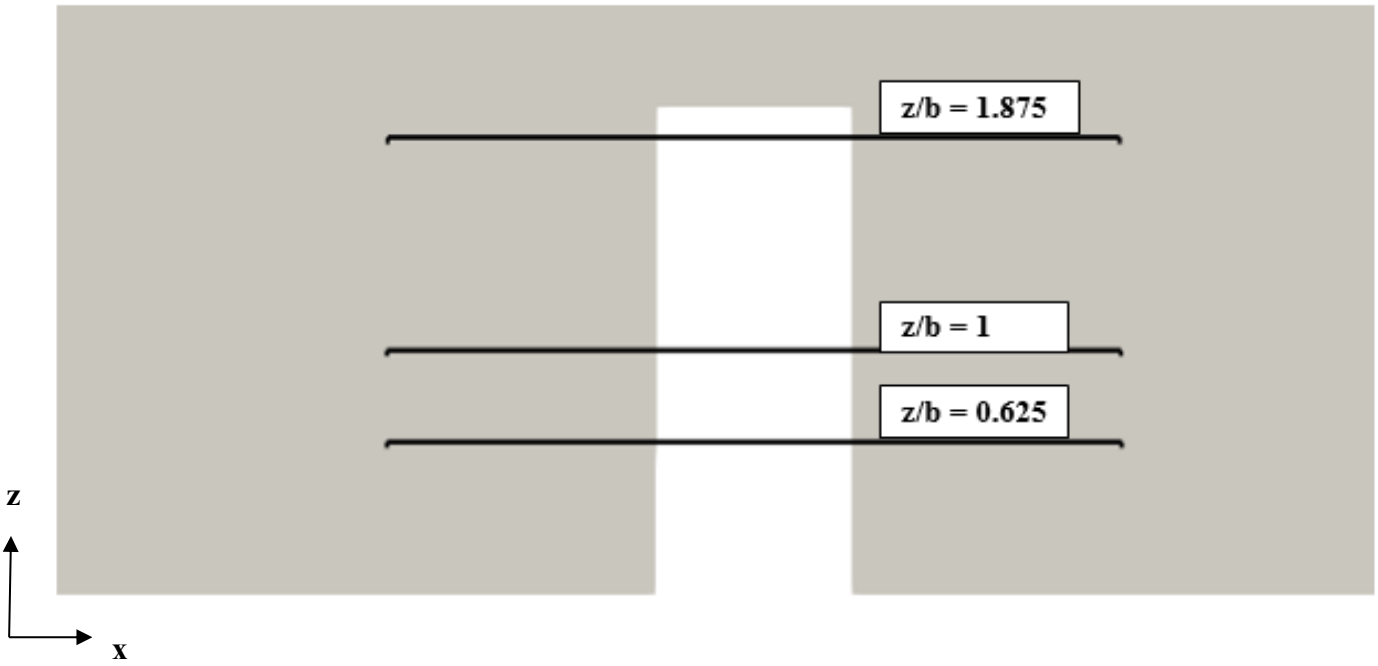

Figure 4.10: Spanwise locations

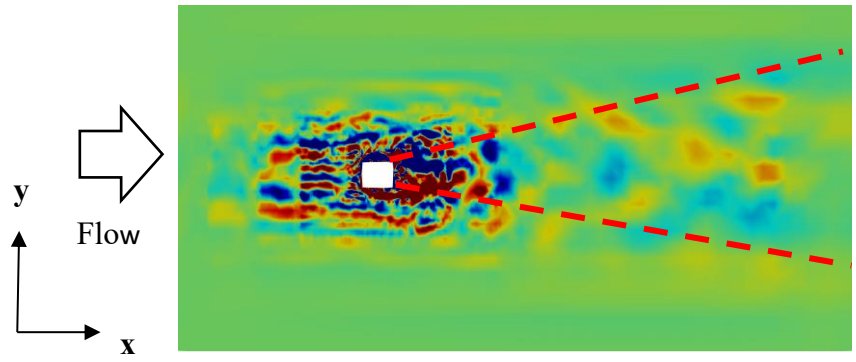

(a). z/b = 0.625 (Close to the ground)

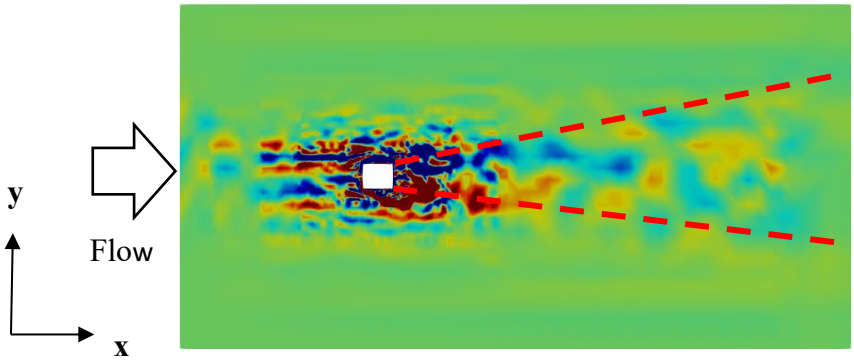

(b). z/b = 1 (Mid-span)

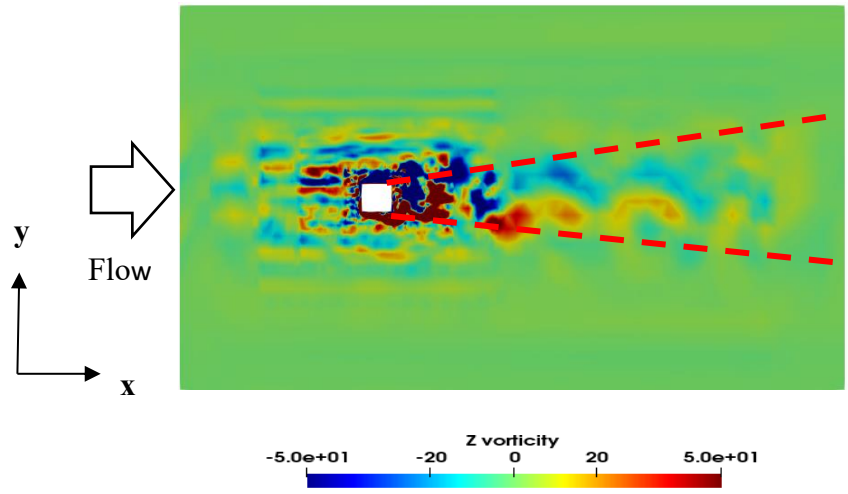

(c). z/b = 1.875 (Close to the tip)

Figure 4.11: Instantaneous Spanwise Vorticity at (a). z/b = 0.625, (b). z/b =1, and (c). z/b = 1.875.

Vortex shedding is asymmetric at all spanwise positions, except near the building's tip, when the separated shear layers are considered. In this region, vortex shedding is also more organized because the flow in that region is 3-dimensional. Strong vortex shedding is observed in all cases but was at its peak when z/b = 1.875. Higher magnitudes of spanwise vorticity components in the building's wake zone further downstream can cause larger streamline curvatures. This adds to the evidence of increased strong entrainment in the building's wake. For the building, the separated shear layer from the leading edge has a large vorticity magnitude. Flow entrainment occurs when the separated flow from the leading edge affects the wake structures. Because of the small aspect ratio of the building (AR = 2), the counter-rotating vortices on two sides of the building suggests that Kàrmàn type vortices are suppressed by the upwash and downwash flow.

It can be concluded that closer to the tip of the building (z/b = 1.875), the distance from the building at which the vortex shedding structure appears is reduced. Vortex shedding effects are minimal. The strength of vortex shedding is felt close to the bottom of the building, but as the distance from the ground is increased (the mid-section of the building), vortex shedding transforms from asymmetrical to symmetrical vortex shedding. The ground is also where horseshoe vortex spiral nodes were formed.

Considering the separated shear layers, vortex shedding at all spanwise locations, except close to the building's tip is asymmetric. The spanwise symmetric vortex-shedding becomes more visible at the mid-section height of the building (z/b = 1), and its strength continuously diminishes with the increase of the distance from the ground to the tip of the building.

Asymmetric and symmetric vortex shedding were observed simultaneously, but the probability of an asymmetrically arranged vortices is higher from the mid-height of the building to the top of the building. Due to ground effects, vortex shedding is asymmetrical closer to the ground of the building at z/b = 0.625. The chaotic structures are more spread out and visible further downstream of the building than the mid-span or close to the tip of the building where effects of vortex shedding dampen or reduce.

4.7 Transverse Vorticity

Figure 4.12 shows the transverse vorticity in the x-z plane at y/b = 0. This is used for the visualization of vorticity structure formation and depicts how vortex disappears quickly further downstream. It also shows how vorticity changes with time around the building and at the wake.

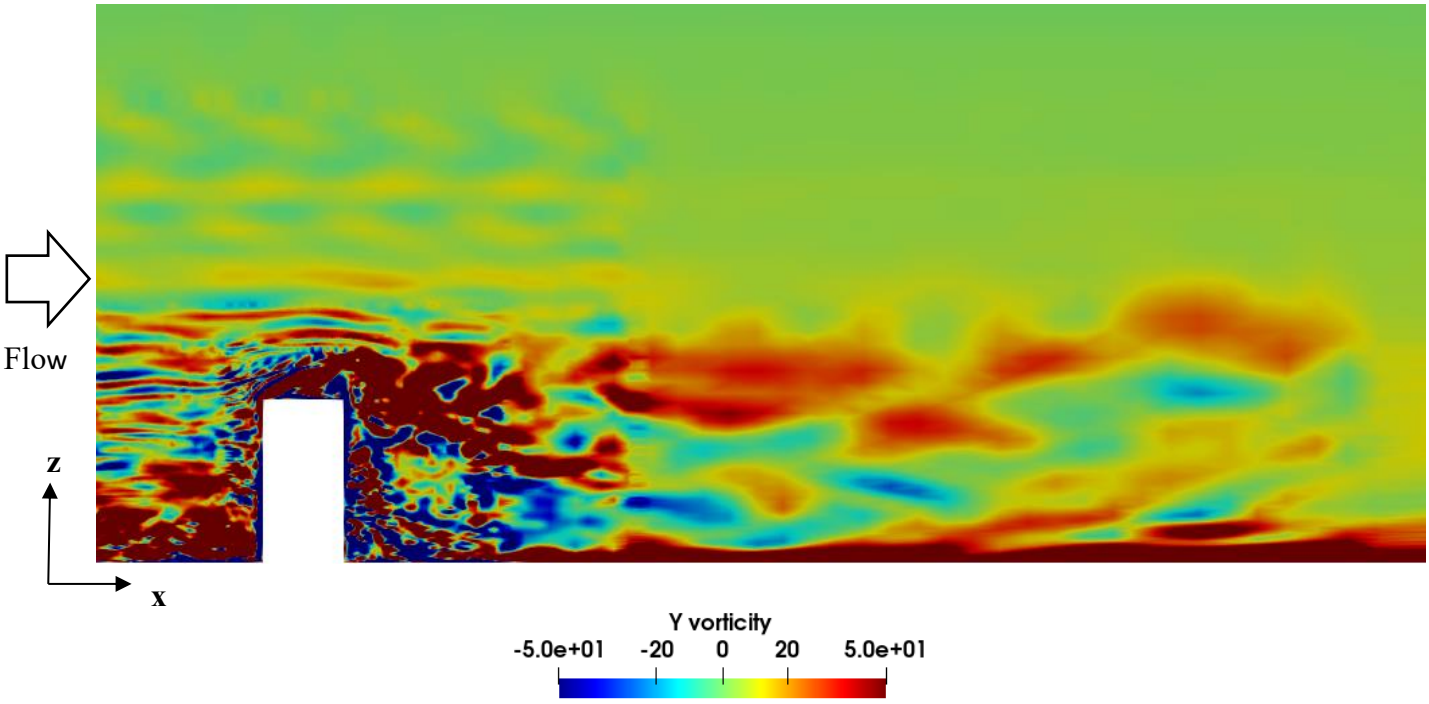

Figure 4.12: Transverse Vorticity (ω_y) at y/b = 0

Figure 4.12 shows that the wake flow is turbulent in the transverse direction of the flow. The wake velocity field and vorticity structures are identified. Small-scale chaotic structures are observed which shows that the flow is transient. At the high Reynolds number of 6.75 x 10^4, it is observed that vortex shedding is not organized. A weak downwash flow is observed showing an increase in vorticity after flow separation. But further downstream of the building, the downwash flow effects disappear.

4.8 Conclusion

Large eddy simulation is successfully used to study wind flow around a tall building. The fluid dynamics, wake dynamics, and flow structures around the building and the effects of vortex shedding at the near and far wakes are investigated. The LES results are further validated with wind tunnel results to ensure numerical accuracy. The wake dynamics is surveyed to identify

various flow features and structures that have the possibility of creating a dangerous environment for pedestrians in the proximity of a tall building. All wake features and flow structures are captured when compared with Wang et al. model [21]. Because of reversed flow close to the ground which gives rise to standing vortices at the windward wall of the building, as well as downwash effects and recirculation zone at the wake of the building, they create high changes in wind speed and thus could cause an injury to people and make them to be swept over by these accumulation of vortices at the near-wake. These are flow features associated with tall buildings. Therefore, the effects of vortex shedding which is illustrated using vorticity shows that at the far wake region, pedestrians would experience a better comfort due to wind flow being laminar further downstream.

Because the flow is highly turbulent, different flow structures are captured. A horseshoe vortex is formed which is inclined towards the wake and influences the wake dynamics. Spanwise vortices were also formed in the early stages of spanwise vortex development which transforms to Reverse-C shape and then to hairpin vortices. Base vortices and tip vortices are also observed at the near and far-wakes region when visualizing the evolution of vortex structures using mean streamlines. We noticed how the tip vortices disappear at the far-wake, which shows how the effects of downwash flow diminish further downstream, while base vortices continue growing primarily due to ground effects. The effects of vortex shedding using various spanwise locations along the tall building show how the effects of vortex shedding are minimal close to the tip of the building and strongest close to the ground of the building because of the three-dimensionality of flow in this region.

Chapter 5

WIND EFFECTS AROUND A TALL BUILDING WITH A SMALL BUILDING PRESENT DOWNSTREAM OR UPSTREAM

5.1 Introduction

This study focuses on investigating the impact a small building has on wind flow when placed in the aerodynamic wake (downstream) and upstream of a tall building using Large Eddy Simulations. The main aim of this chapter is to study the influence of building neighbors on wind flow around a tall building. The results obtained from this chapter will show how the fluid dynamics, wake dynamics and flow structures around a tall building change when a small building is present downstream and upstream of it. This study will show flow features around both buildings and how building neighbors affect the wake topology of a tall building. It is important to study the effects of building neighbors around a tall building because tall buildings are typically built-in clusters rather than alone in a real urban environment. The wake and flow structures of the tall building are expected to alter because of the presence of the small building downstream and upstream. This chapter addresses the main aim of the thesis on analyzing the fluid dynamics, wake flow structures, and flow structures around the tall building when the small building is downstream and upstream of it.

5.2: Numerical Validation for the Small Building Downstream Case

A grid independence study is conducted for the three grids using the tip of the tall building's mid-point to the top of the fluid domain. Table 5.1 shows the number of grids, simulation time, and time steps used to conduct the grid independence study for the small building downstream case.

Table 5.1: Validation and grid independence study for a small building placed downstream of a tall building

Mesh name	**Number of nodes (x 10^6)**	**CPU Hours**	**Time step (Δt)**
Level-1	**1.73**	**3 weeks**	**2e-5**
Level-2	**3.24**	**4 weeks**	**3e-4**
Level-3	**4.03**	**5 weeks 6 days**	**1e-4**

Figure 5.1 shows the velocity profiles at the mid-point of the tall building with the three grids for the small building downstream case.

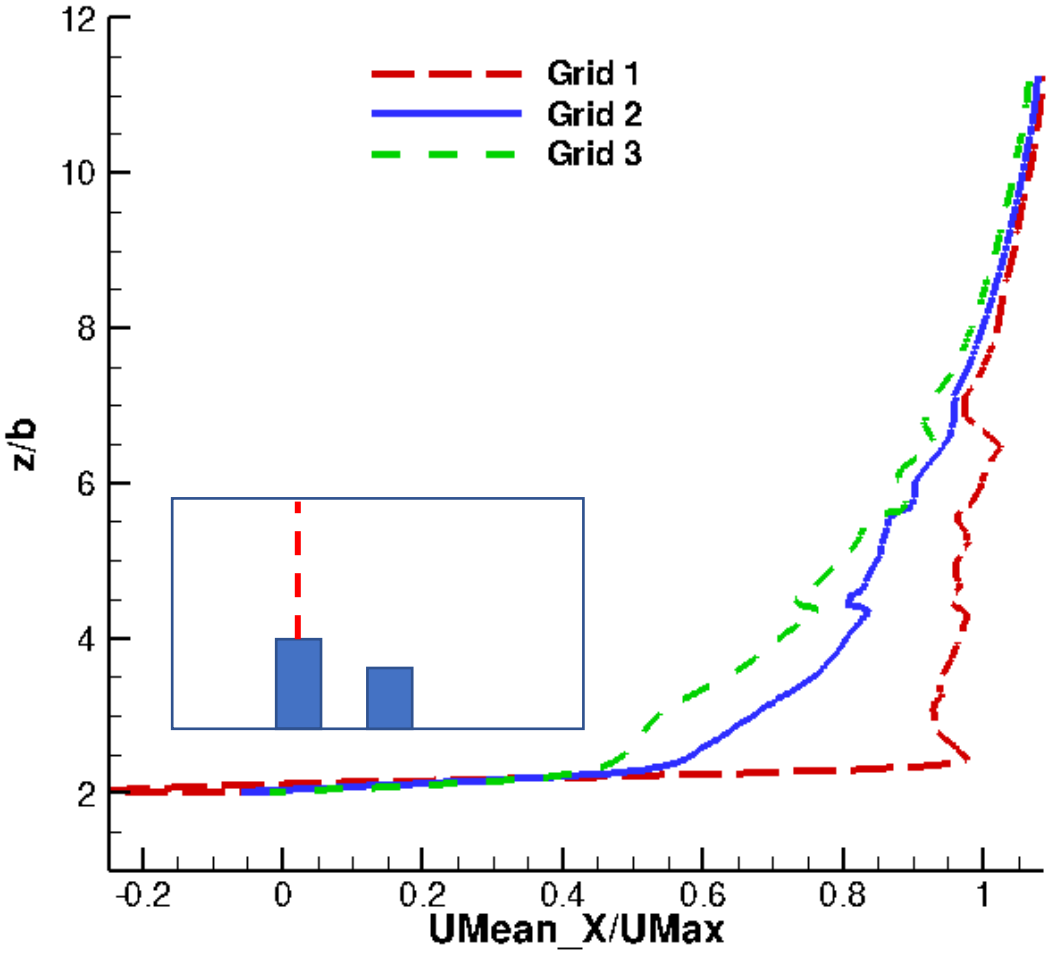

Figure 5.1: Velocity profiles showing grid independence study for the small building downstream case

5.3 Numerical Validation for the Small Building Upstream Case

A grid independence study is conducted for the three grids by using the tip of the tall building's mid-point to the top of the fluid domain. Table 5.2 shows the number of grids, simulation time and time step used to conduct grid independence study for the small building upstream case.

Table 5.2: Validation and grid independence study for a small building placed upstream of a tall building

Mesh name	Number of nodes (x 10^6)	CPU Hours	Time step (Δt)
Level-1	**1.72**	**3 weeks**	**1e-4**
Level-2	**3.19**	**4 weeks**	**1e-4**
Level-3	**4.03**	**5 weeks 4 days**	**1e-4**

Figure 5.2 shows the velocity profiles at the mid-point of the building with the three grids.

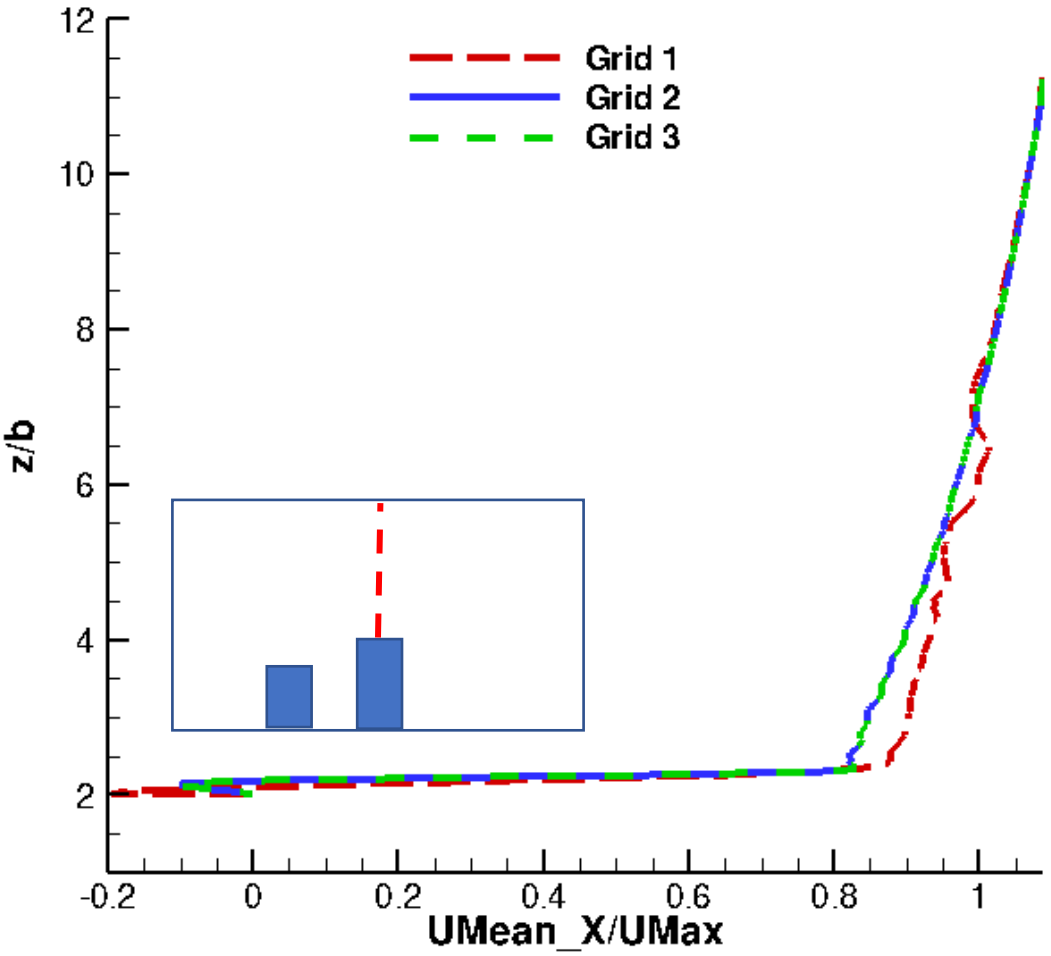

Figure 5.2: Velocity profiles showing grid independence study for the small building upstream case

5.4 Pressure and Velocity Distribution for the Small Building Downstream and Upstream Cases

Pressure and velocity fields are also used in visualizing the wind effects around the buildings. To further examine unsteady characteristics of the wake, instantaneous transverse vorticity is used in visualizing turbulent flow and the effects of vortex shedding in the wake regions.

5.4.1 Pressure and Velocity Distribution when the Small Building is Placed Downstream

Figure 5.3 shows the pressure distribution on the symmetry plane for a small building placed downstream of the tall building.

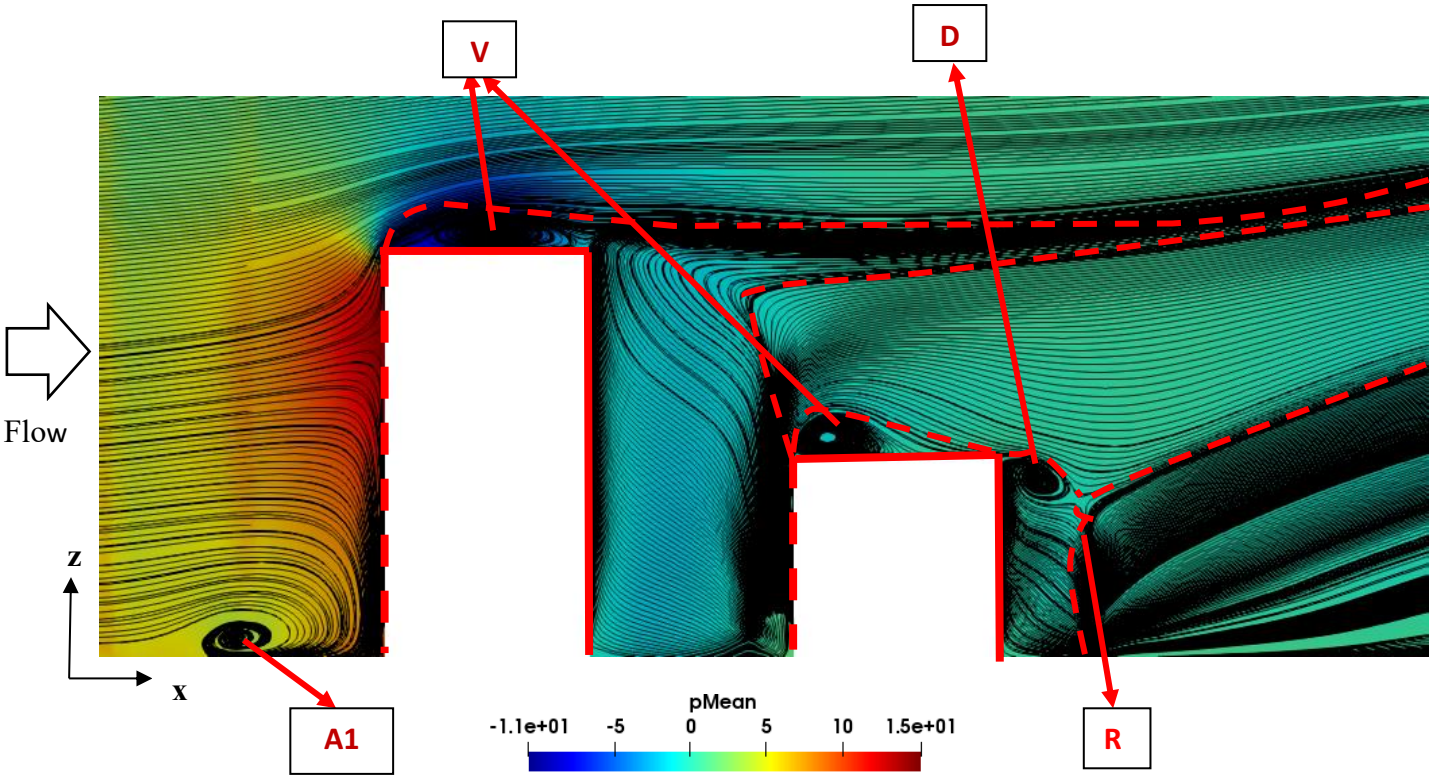

Figure 5.3: Pressure distribution on the symmetry plane for small building placed downstream of a tall building at y/b = 0 (V = Top face bubble, D = Side separation face bubble, A1 = Horseshoe vortex spiral node, R = Impingement point).

Stagnation point at the leading edge of the tall building is also observed and the stagnation point was similar to the single tall building case. In the symmetry plane at y/b = 0, one horseshoe vortex spiral node, A1 is formed as opposed to the single tall building where two horseshoe vortex spiral

nodes are formed. The horseshoe vortex spiral node, A1 emerges because of the flow separation caused by the high streamlines. The impingement point denoted by R is formed which occurs close to the tip of the small building as opposed to the single tall building case which occurred at the mid-plane of the tall building. The upwash flow clashes with the downwash along the X direction but is much stronger than the single tall building case. Reverse flow occurs on top of the tall and small building, but the recirculation was greater on the tall building. Downwash flow is also present in the wake of the tall and small building, but the strength of the downwash on the small building (as shown by the dotted line) is much weaker than when only the single tall building was considered. This is because of the shielding effects of the walls of the tall building and the windward wall of the small building. The upwash flow from the ground also superimposed the downwash flow giving rise to weak downwash and strong upwash flows in the wake of the small building. Side-bubbles denoted by D appear close to the tip of the small building in the symmetry plane (y/b = 0) as opposed to the single tall building case where the side-bubbles were close to the mid-plane of the building. This also illustrates how the presence of the tall building reduces the intensity of downwash flow in the wake of the small building. The re-circulation zone behind the building (leeward region of the tall building) which led to a strong accumulation of vortices at the leading edge of the small building (shown by the darker region) creates flow separation and directed flow upwards in the flow regime of the downwind region of the tall building. This effect contributed to insignificant downwash flow of the tall building. This shows how the presence of the small building reduces pressure significantly at the pedestrian level, and thus undesirable wind effects from the tall building as seen from the single tall building case.

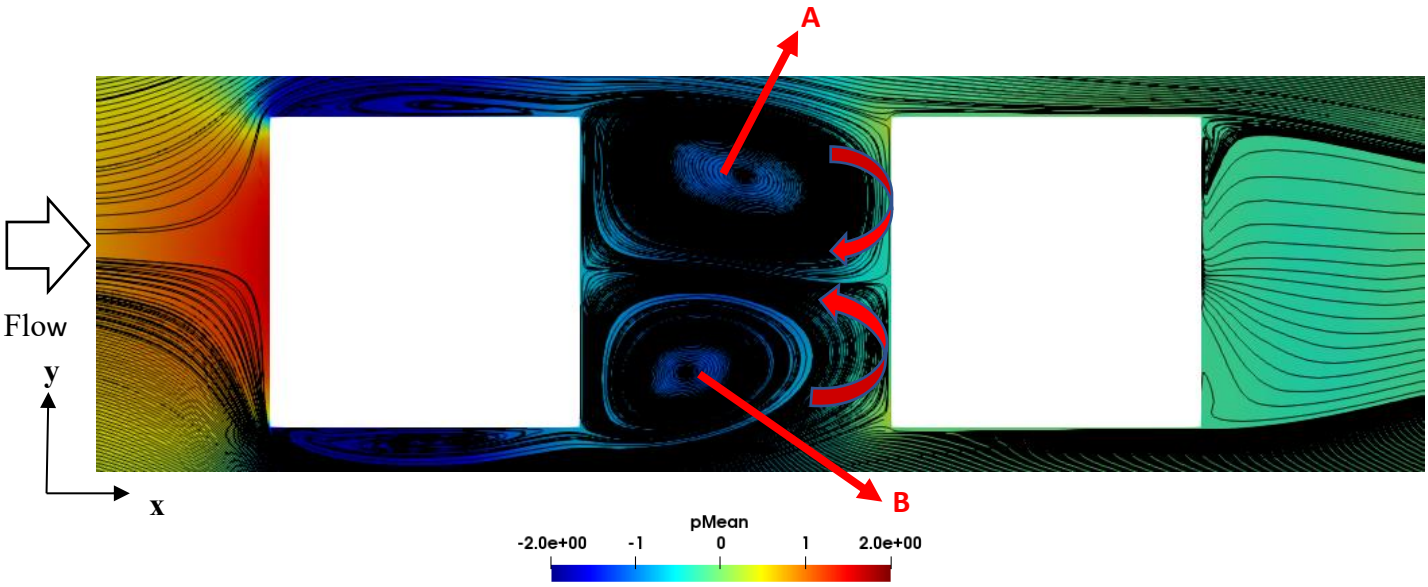

Figure 5.4: Pressure distribution on the mid-span plane for the small building placed downstream of a tall building at z/b = 1 (A and B = Spiral nodes).

Figure 5.4 shows the pressure distribution on the mid-span plane for the small building placed downstream of the tall building. Consistent with the single tall building case, two symmetrically distributed spiral nodes (A and B), also known as horseshoe vortex spiral nodes are formed. Horseshoe vortex spiral nodes are not present in the wake of the small building because of the accumulation of vortices downstream of the tall building and because of the leading edge of the small building. The pressure distribution is similar to the single tall building case.

The pressure distributions around the building match the pressure distribution of the single tall building. The placement of an adjacent shorter building downstream of the taller building reduce the pressure in the wake of the taller building and thus a negative pressure is formed at the pedestrian/ground level. Therefore, pressure at the ground level (interface between the tall and small building) was minimum (negative pressure), but pressure slightly increased positively. The distance at which the reduction in pressure occur is at a much shorter distance than when the tall building was isolated by about 67%. This is because of the presence of the small building being placed in the aerodynamic wake of the tall building. The streamlines at the leading edge of the tall building are similar to the streamlines of the single tall building case. However, downstream of the tall building, the streamlines are almost like a parallel wind flow from the top of the tall building because of the reverse flow turbulence effect from the tip of the small building. Wind flow from the tall building remains parallel/straight and directed upwards because of the shielding

effects of the small building. Streamlines from the top of the tall building collide with streamlines from the top of the small building which creates this parallel upward directed wind flow. Two arc-like separation lines are present on the small building but only one is observed in the tall building which was similar to the single tall building case. Also, the pressure on top of the first building is usually much lower than the pressure of the building further downstream.

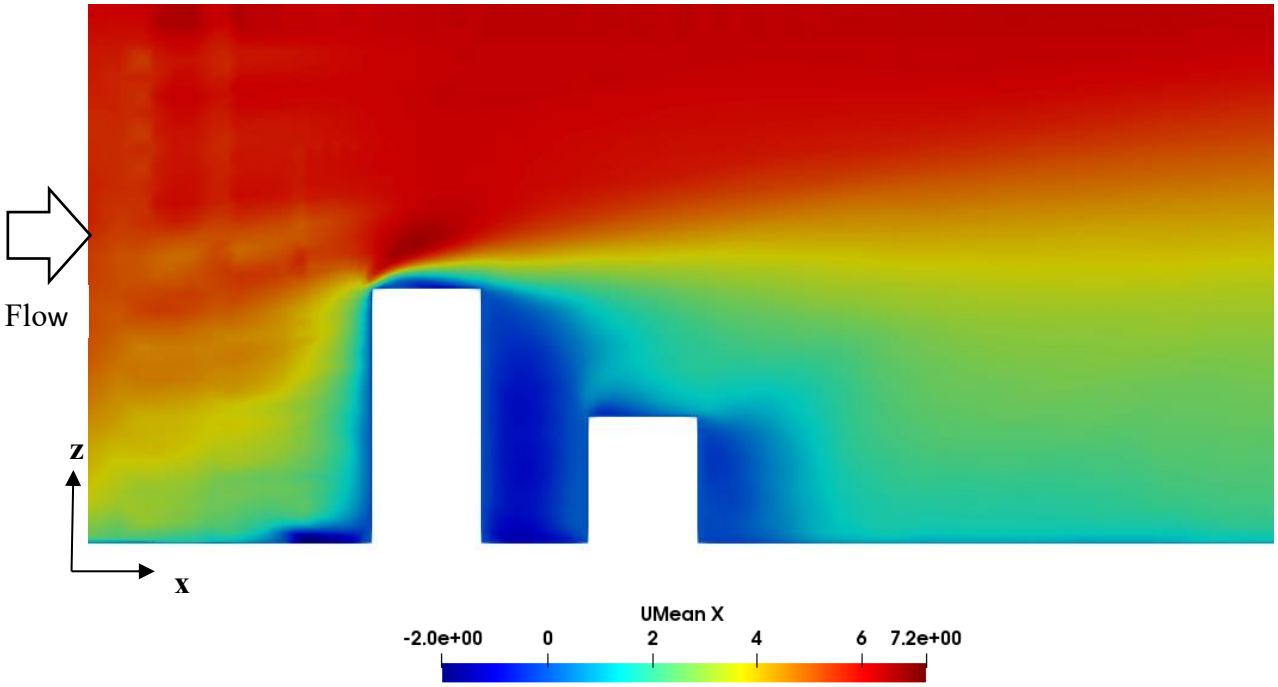

Figure 5.5: Mean streamwise velocity at y/b = 0 for the small building downstream case

Figure 5.5 shows the time-averaged (mean) streamwise velocities. The results revealed that reverse and reattachment flow on top of both buildings were not clearly replicated, and the recirculation zone behind the building is also underestimated. It is also difficult to estimate the peak velocities using averaged values as opposed to instantaneous values of velocity below which clearly show variation in velocity in the fluid domain.

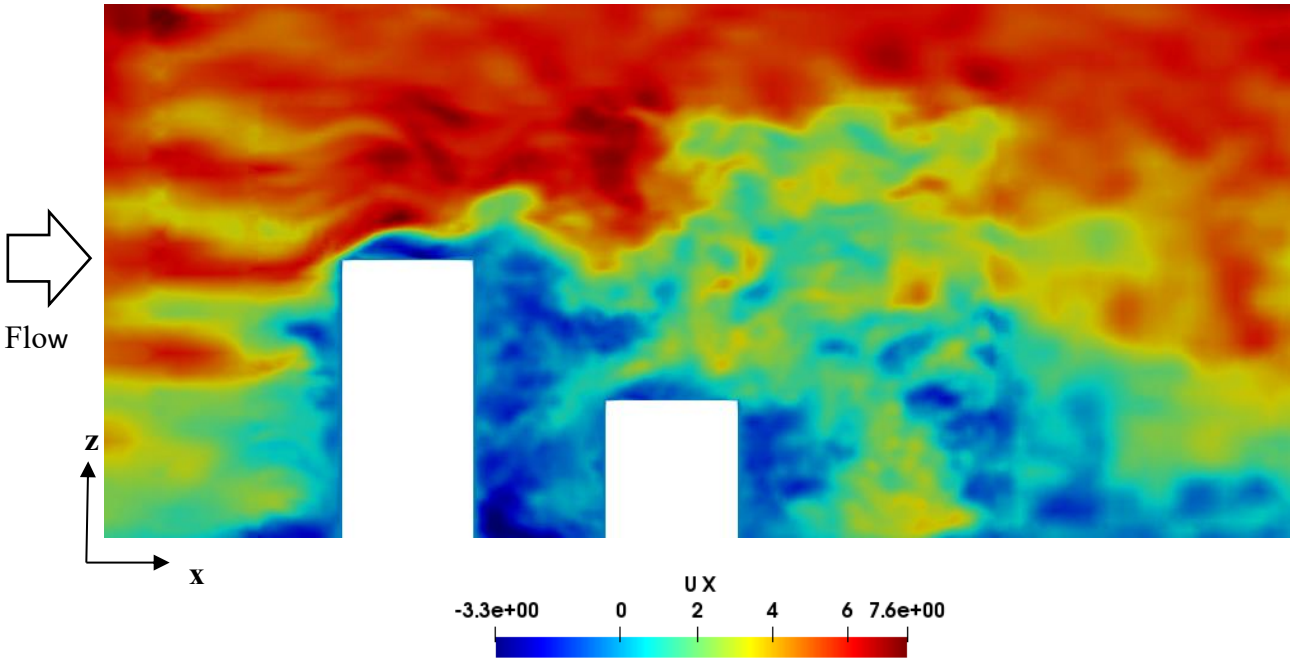

Figure 5.6: Instantaneous streamwise velocity at y/b = 0 for the small building downstream case

Figure 5.6 shows the instantaneous streamwise velocities. LES captures turbulence effects well as seen from the Figure 5.6. Changes in velocity can be visibly illustrated as shown in the far-wake region where vortex shedding occurs and velocity downstream of the small building reduces and then increases before reducing again. These changes cannot be illustrated using time-averaged values of streamwise velocity. The shielding effects of the small building downstream show a decrease in the mean wind velocity. Velocity distribution was also similar to the single tall building case. The instantaneous streamwise velocity shows how wind flow is turbulent and how it becomes disoriented and disorganized when it gets closer to the walls of a building.

5.4.2 Pressure and Velocity Distribution when the Small Building is Placed Upstream

Figure 5.7 shows pressure distribution on the symmetry plane for small building placed upstream of tall building at y/b = 0.

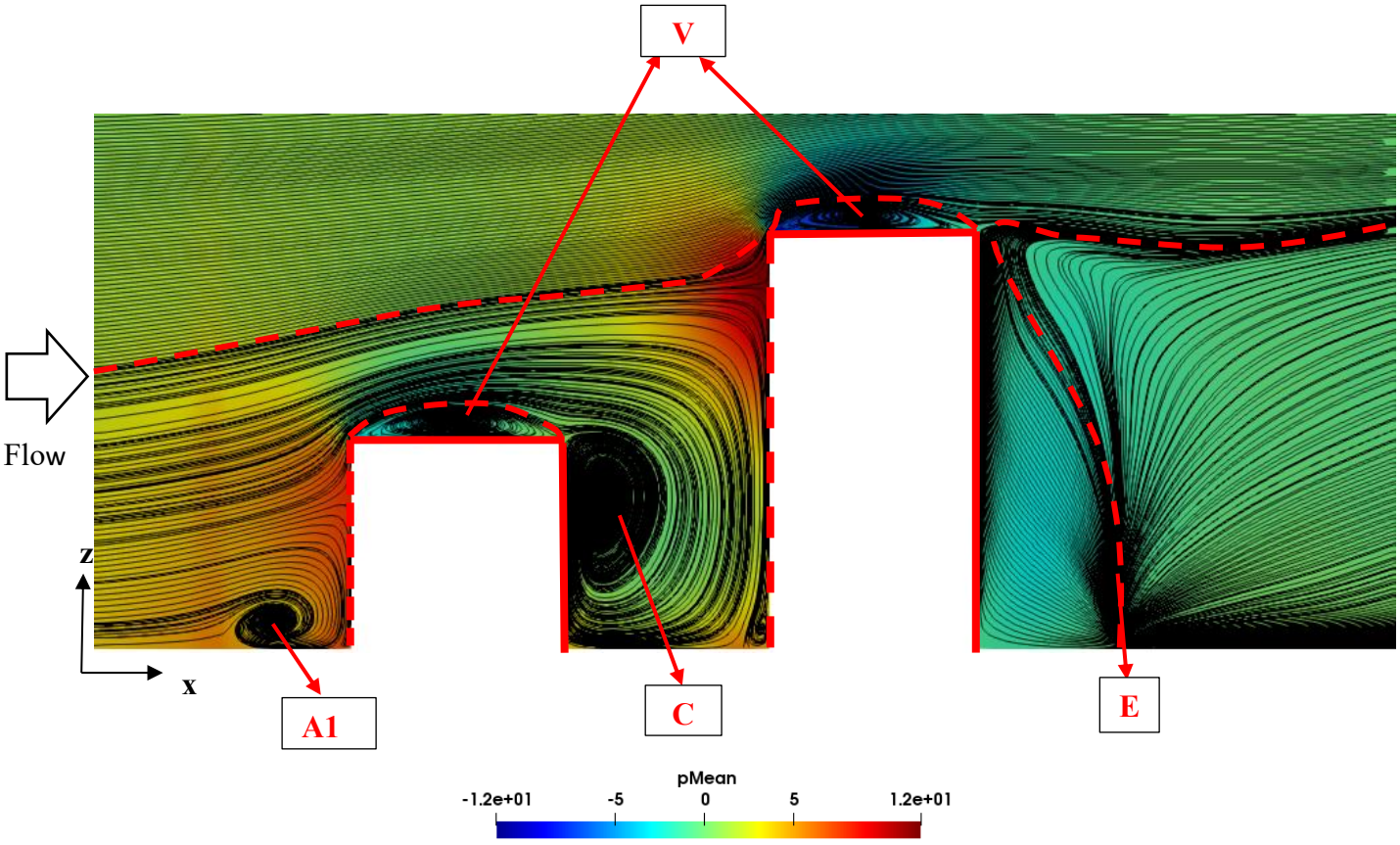

Figure 5.7: Pressure distribution on the symmetry plane for small building placed upstream of a tall building at y/b = 0 (V = Top face bubble, A1 = Horseshoe vortex spiral node, C = Recirculation zone, E = Induced upwash flow).

Reversed flow occur on both buildings which are consistent with the small building downstream case. Downwash flow is weak downstream of the tall building, superimposed by the strong upwash flow formed due to base vortices from the ground surface. This is consistent with the downwash flow from the tall building of the small building downstream case. The presence of the small building upstream of the tall building provides a shielding effect and reduces undesirable wind flow turbulence effects associated with the tall building. The upwash flow denoted by E clashes with the downwash along the X direction but is much stronger than the single tall building case and the small building downstream case. The significant turbulence effect formed in the wake of

the tall building is a strong upwash flow similar to when the small building was downstream of the tall building. One horseshoe vortex spiral node, A1 is also formed upstream of the small building. Because of the tall building further downstream of the small building, a dark line recirculation zone denoted by C is observed downstream of the small building. The walls from the leading edge of the tall building suppress the effects of flow separation from the small building giving rise to the strong recirculation zone. This zone provides undesirable wind effects to pedestrians on the ground level (i.e., interface between the small and tall building).

At the mid-span plane (z/b = 1) in Figure 5.8, similar to the single tall building case, two symmetrically distributed spiral nodes (A and B) are formed downstream of the tall building. However, these nodes are absent downstream of the small building. This illustrates how the presence of a tall building creates pedestrian discomfort. The small building upstream is not sufficient to reduce the unusual turbulent flow in the leeward direction of the building. At the interface between the two buildings, flow is better organized and symmetrically distributed from the trailing edge of the small building to the leading edge of the tall building. Due to flow separation, two vortices C and D are formed around the small building.

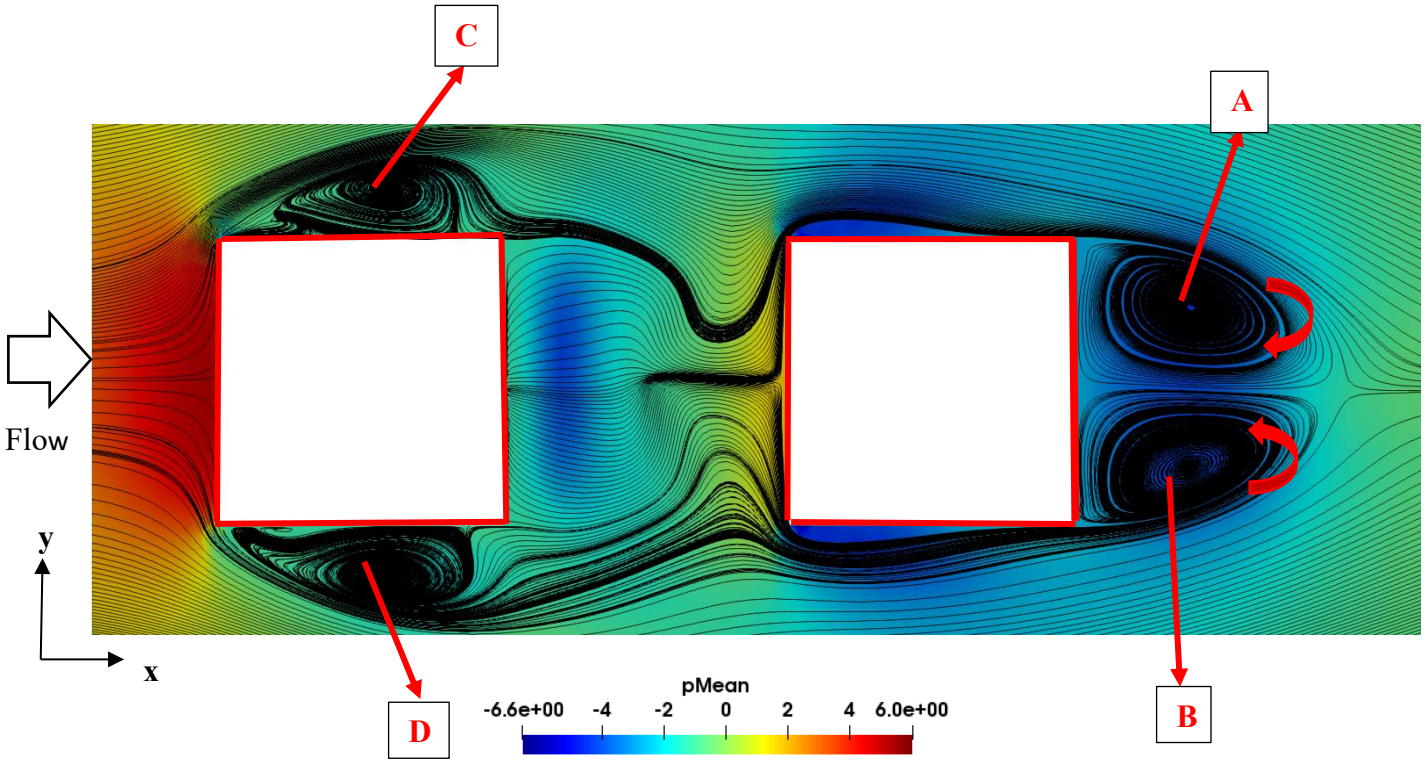

Figure 5.8: Pressure distribution on the mid-span plane for the small building placed upstream of a tall building at z/b = 1 (C and D = Vortices due to flow separation, A and B = Horseshoe vortex spiral nodes)

Figure 5.8 illustrates the pressure distribution on the mid-span plane for the small building placed upstream of the tall building. Here, pressure distribution is consistent with the single tall building case and when the small building was placed downstream of the tall building. Upstream of the small and tall buildings, the pressure was at its peak, and there were two stagnation points in these regions. Downstream of the tall building, the pressure became reduced (a negative pressure), however, this decrease in pressure was not as great as when the tall building was placed upstream of the small building. Therefore, placing a small building upstream of a tall building led to a lesser decrement in pressure downstream as opposed to when the small building is placed downstream of the tall building. The pressure decreased only, but when the small building was placed downstream of the tall building and in the single tall building case, the pressure decreased then increase slightly again downstream. The pressure was its minimum after flow separation occurred on the top of the small building (consistent with the single tall building case) and when the small building was placed downstream of the tall building.

Time-averaged or mean streamwise velocity at the symmetry plane is illustrated in Figure 5.9 to show how the mean velocity provides limited information on the effects of turbulence around the building walls. Features such as vortex shedding, flow separation cannot be captured using this phenomenon, but can be easily visualized using the instantaneous streamwise velocity obtained by LES. The instantaneous streamwise velocity is shown in Figure 5.10 also reveals how wind flow around two parallel buildings are turbulent due to sudden/sharp changes in wind flow when wind interacts with walls of buildings. When wind gets closer to the walls of the building, the velocity reduces and then increases further downstream of the 2nd building/tall building. Because of constant changes in wind speeds (increment and decrement) around two parallel buildings, wind effects become highly turbulent. The velocity remains at its peak in all regions further away from the building, but closer to the building walls, it becomes negative.

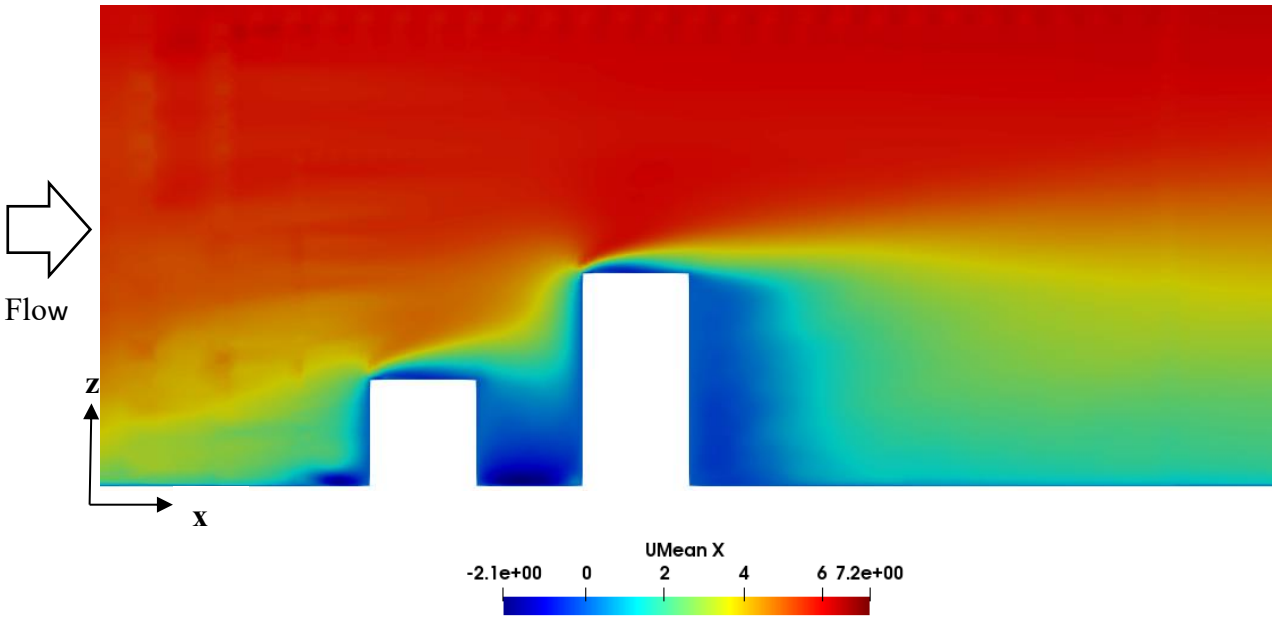

Figure 5.9: Mean streamwise velocity at y/b = 0 for the small building upstream case

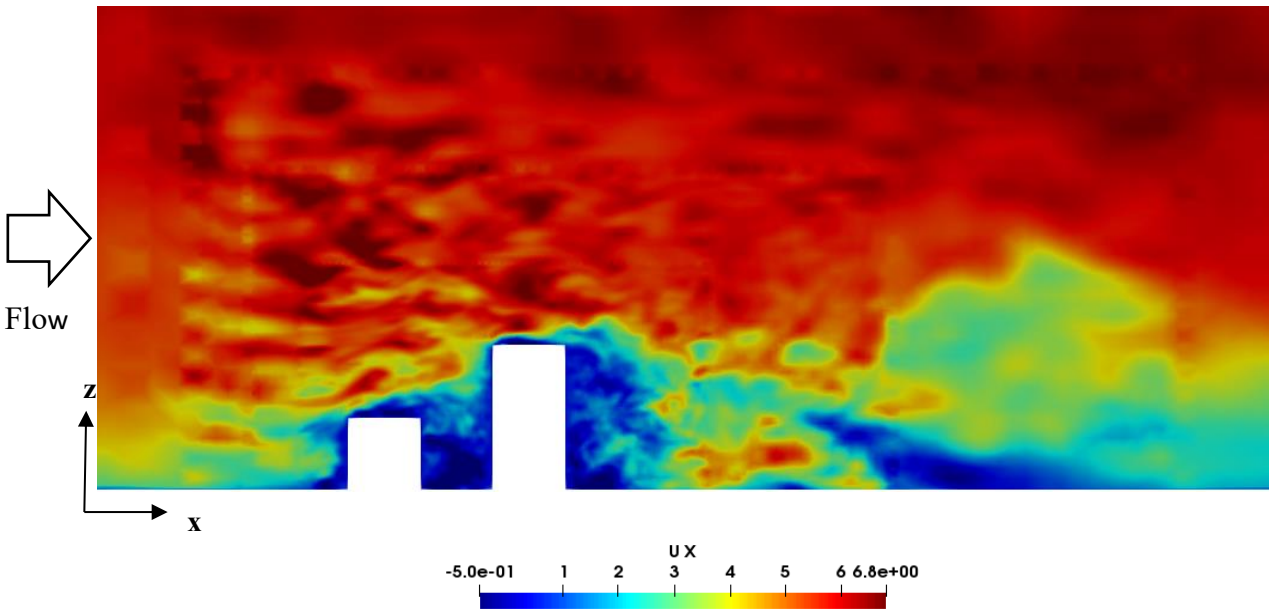

Figure 5.10: Instantaneous streamwise velocity at y/b = 0 for small building upstream case

5.5 Wake Flow Structures for the Twin-building Cases

Wake features and flow structures around the tall building because of the presence of the small buildings (building neighbors) downstream and upstream of the tall building are investigated in this section. The effect of wind flow from the single tall building case are compared with the case when the small building is placed downstream and upstream of the tall building. Q-criterion is then used to visualize wake flow structures formed around the buildings.

5.5.1 Wake Flow Structures for the Small Building Downstream Case

Figure 5.11 shows the isosurface of Q = 40,000 for the small building downstream case from the side and top faces of the two buildings.

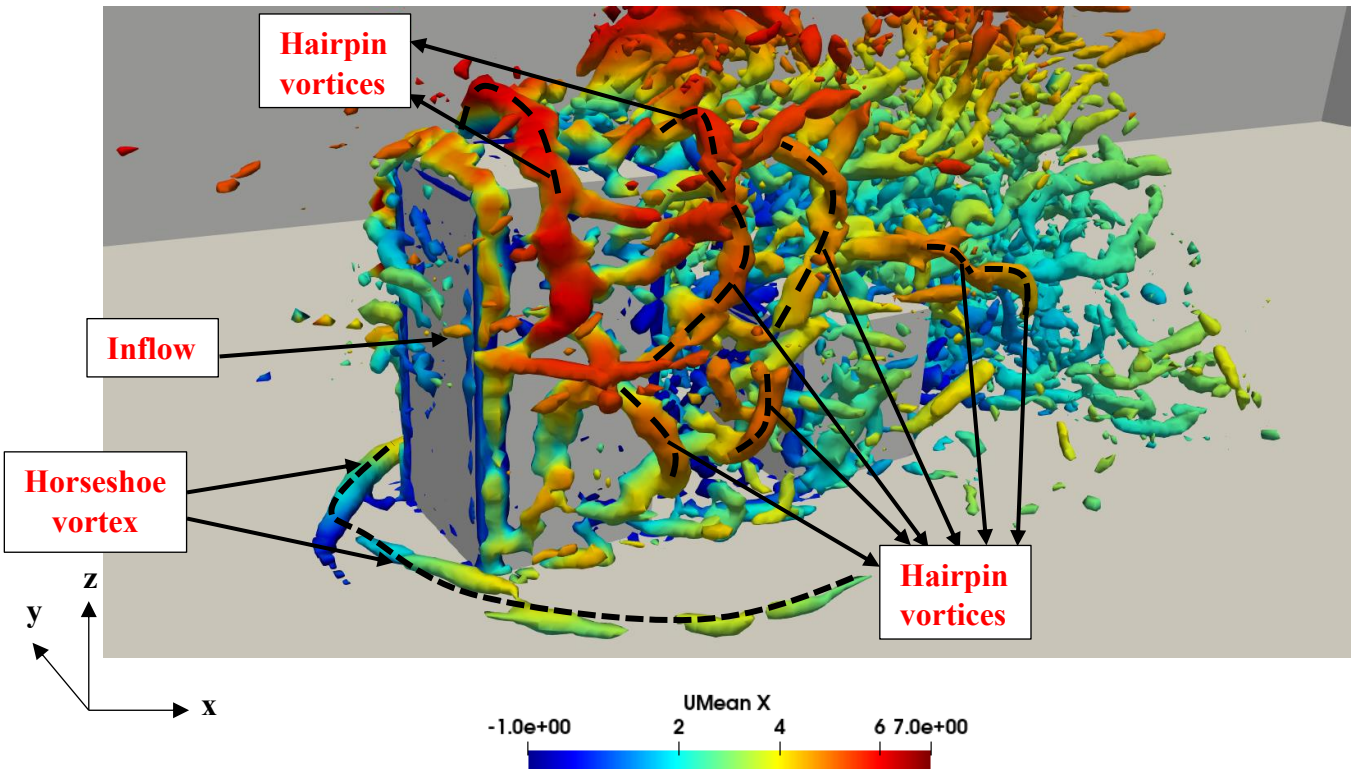

Figure 5.11: Isosurface of Q = 40,000 colored with mean streamwise velocity for the small building downstream case

The flow is unsteady and vortex shedding occurs. Horseshoe vortex is formed due to reverse flow and can be observed at the ground surface, which slightly extends into the wake. Hairpin vortices can also be observed around both buildings, the interface between the two buildings and at the wake region. However, the impact of vortex shedding is greatly reduced downstream of the small building, or the wake region as seen from the mean streamwise velocity being at its peak on the top face around the tall building. But at the interface between the two buildings, the mean streamwise velocity reduces due to interference effects of the walls of the small building from the leading edge. Consistent with the single tall building, the hairpin vortices transitions into the fragmentation of huge chunks of vortex structure in the further downstream region.

5.5.2 Wake Flow Structures for the Small Building Upstream Case

Figure 5.12 shows the isosurface of Q = 30,000 colored with the mean streamwise velocity for the small building upstream case.

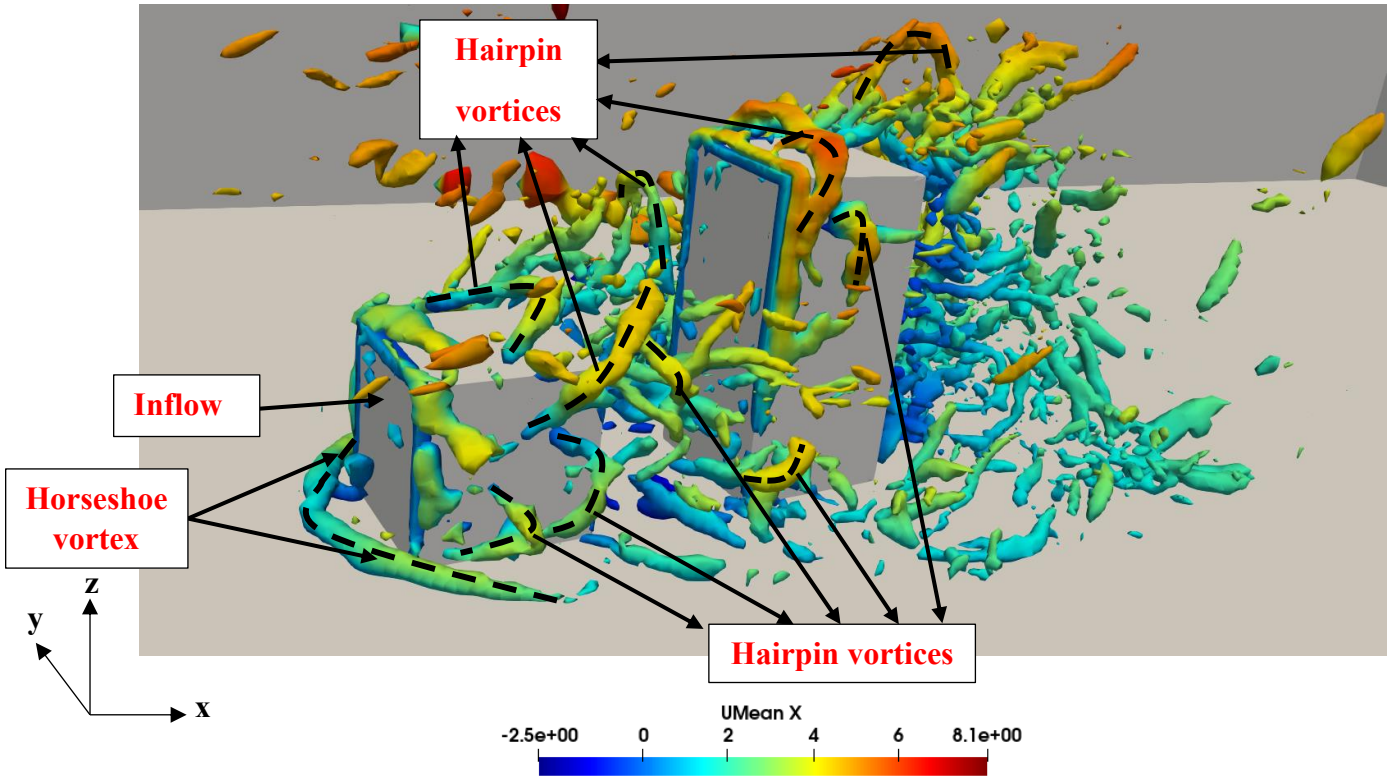

Figure 5.12: Isosurface of Q = 30,000 colored with mean streamwise velocity for the small building upstream case

Horseshoe vortex and hairpin vortices can be observed. It can be observed how the strength of vortex shedding is much weaker at the windward face of the small building which led to a decrement in the mean streamwise velocity at the windward face of the tall building. This is in contrast with the case when the small building was placed downstream of the tall building. Regions around the tall building have a much lower mean streamwise velocity due to the interference effects of the small building upstream.

5.6 Instantaneous Transverse Vorticity for the Small Building Downstream Case

Figure 5.13 shows the instantaneous transverse vorticity colored by y-vorticity for the small building downstream of the tall building case.

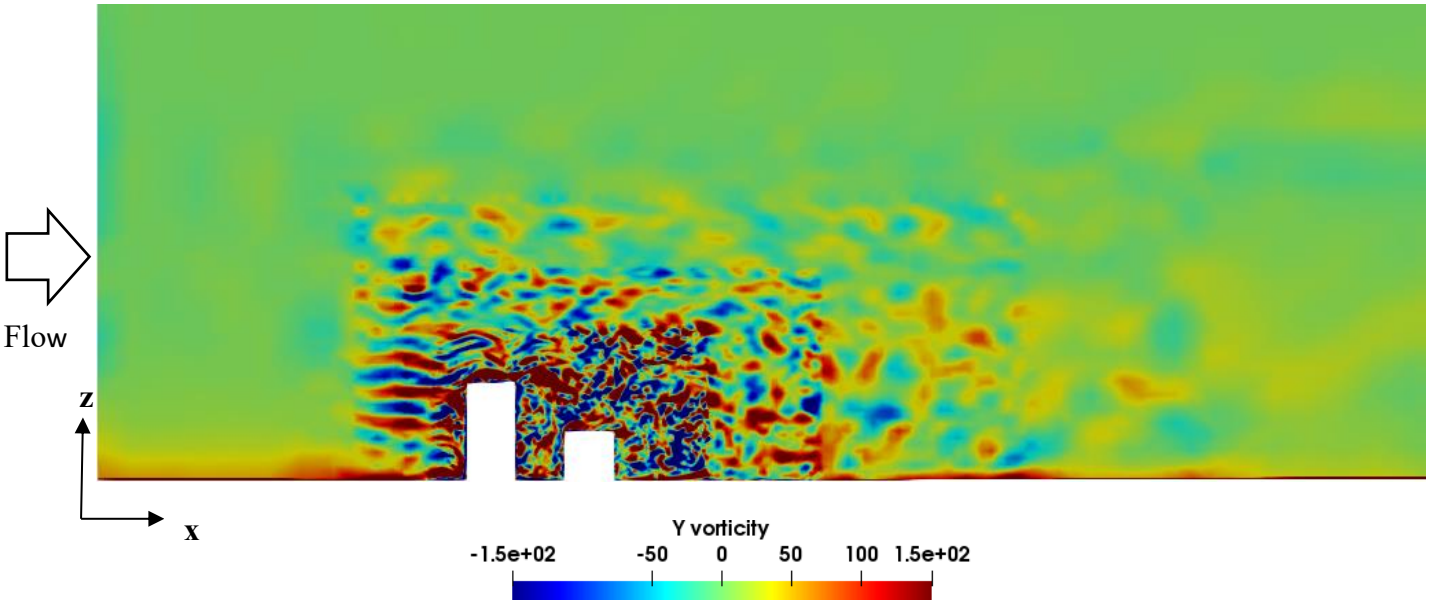

Figure 5.13: Instantaneous transverse vorticity at y/b = 0 for small building downstream case

The transverse vorticity is consistent with the single high-rise building case in which vorticity was maximum at the leading edge and the top of the tall building. Also, vorticity is maximum at the ground level due to ground effects when wind flows from the inlet to the outlet of our fluid domain. Consistent with the single tall building case, the separated shear layer from the leading edge has a large vorticity magnitude. Small-scale chaotic structures can be observed when the wind flow gets closer to the building but because of the twin-arrangement of buildings, chaotic structures are more visible/present downstream of the single tall building. Because of the small building downstream of the tall building, the strength of vorticity as seen from the downwash flow originating from the tall building is much weaker than the single tall building case. The unsteadiness in the flow can be seen from at the interface between the two buildings and the wake of the small building but further downstream of the small building this unsteadiness characterized by chaotic structures diminishes.

5.7 Instantaneous Transverse Vorticity for the Small Building Upstream Case

Figure 5.14 illustrates the instantaneous transverse vorticity for the small building upstream case colored by y-vorticity at y/b = 0.

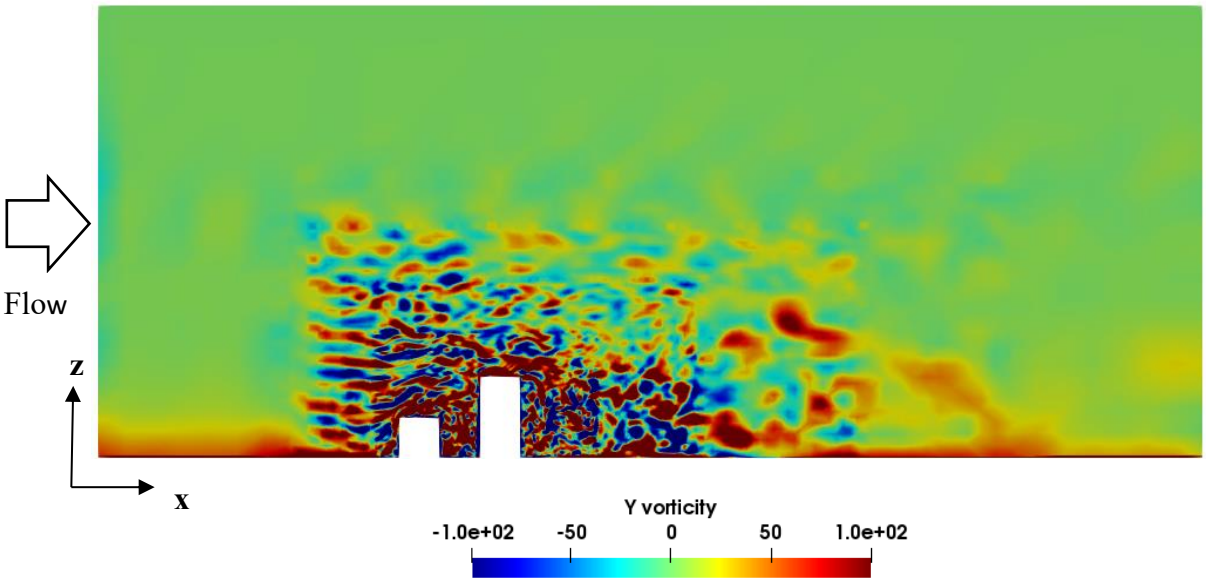

Figure 5.14: Instantaneous transverse vorticity at y/b = 0 for small building placed upstream case

Here, instantaneous transverse vorticity is maximum at the leading edge of the small building, which is consistent with the small building downstream case, where the first building being the tall building has the maximum vorticity. Vorticity is also maximum at the ground surface which is consistent with the single tall building and small building downstream cases. The separated shear layers from the small and tall buildings also have the highest vorticity. It can be observed how the strength of the downwash from the tall building is weak because of the presence of the small building. Further, vortex shedding effects decrease in the far wake region of the fluid domain. However, close to the buildings, the effects of vortex shedding are at their peak because of constant interaction of the wind with the building walls. Flow around the buildings is highly unsteady and thus turbulent. But the effects of unsteadiness diminish farther upstream and downstream of the buildings. This confirms the fact that flow in an urban environment is not only turbulent, but it is in the atmospheric boundary layer (ABL).

5.8 Mean Pressure Coefficients

The wind pressure distribution on a building is usually described by a dimensionless pressure coefficient. Also, the surface pressure on a body is stated as a unitless pressure coefficient, with the mean, root-mean-square fluctuation, maximum, and minimum values all being distinguished.

The mean or time-averaged pressure coefficient, $\overline{C_p}$ is expressed as:

$$\overline{C_p} = \frac{\bar{p} - \overline{p_0}}{\frac{1}{2}\rho U^2}$$

where $\bar{p}$ is the mean pressure at the wall, $\overline{p_0}$ is the reference mean static pressure, ρ is the air density and U is the reference wind velocity in undisturbed flow.

5.8.1 Numerical Results of Mean Pressure Coefficients for the Small Building Downstream Case

The numerical results of the mean pressure coefficients ($\overline{C_p}$) is compared with wind tunnel results from Holscher and Niemann [71] for validation purposes. In general, the numerical simulation results match well with the wind tunnel results. However, some discrepancies in ($\overline{C_p}$) are observed for the building neighbors (small buildings) due to the tall building, and because the wind tunnel results are for an isolated cubic building without the presence of building neighbors. At x/b = 0 and y/b = 0.5, the mean pressure coefficients ($\overline{C_p}$) on the windward faces of the tall building and small building (at x/b = 2 and y/b = 0.5) are presented in Figures 5.15 and 5.16 respectively, showing the contours of $\overline{C_p}$ and vertical distribution of $\overline{C_p}$ along the building height.

As seen from Figure 5.15 below, a positive value of $\overline{C_p}$ is observed from the ground of the domain across the height of the building and then close to the tip of the building, the $\overline{C_p}$ becomes negative. The mean pressure coefficient, $\overline{C_p}$ varies unsteadily from the ground of the domain to the tip of the building. Mean pressure coefficient ($\overline{C_p}$) at the windward face of the tall building (also known as the stagnation point region), is at its the peak with a value of $\overline{C_p} \approx 0.4$ (the tip of the building), across the height of the building. There are higher values of $\overline{C_p}$ at the windward face of the tall building upstream than other faces, particularly the windward face of the small building ($\overline{C_p} \approx 0.07$)

due to the incoming wind with undisturbed velocity field [46]. At the windward face of the small building in Figure 5.16, the low mean pressure coefficient at the tip shows how pressure significantly reduces after flow separation occurs. The taller the building, the higher the $\overline{C_p}$, but the mean pressure coefficient for the small building in this research were much lower (88.6% decrease) when compared to the wind tunnel results due to the wind sheltering effects of the tall building which influences the direction of wind flow. At the leeward faces, the mean pressure coefficient is expected to be much lower, and this is justified by a negative value of pressure in modern wind loading standards. With this analysis, it is simple to decide on pressure tap distribution on a building model if you know how much pressure is distributed on the sides of the building. For example, due to sharp pressure gradient, the windward side of the building requires more pressure taps at a higher level than the leeward side, which requires less pressure taps [72]. Thus, the gradual increase of mean pressure coefficient shows how mean wind load decreases downstream because of the presence of the small building and aerodynamic wake effects dampen or weaken much quickly when only a single tall building is present. In figure 4.5 above, we saw how the pressure also significantly reduced in the wake region because of the presence of the small building.

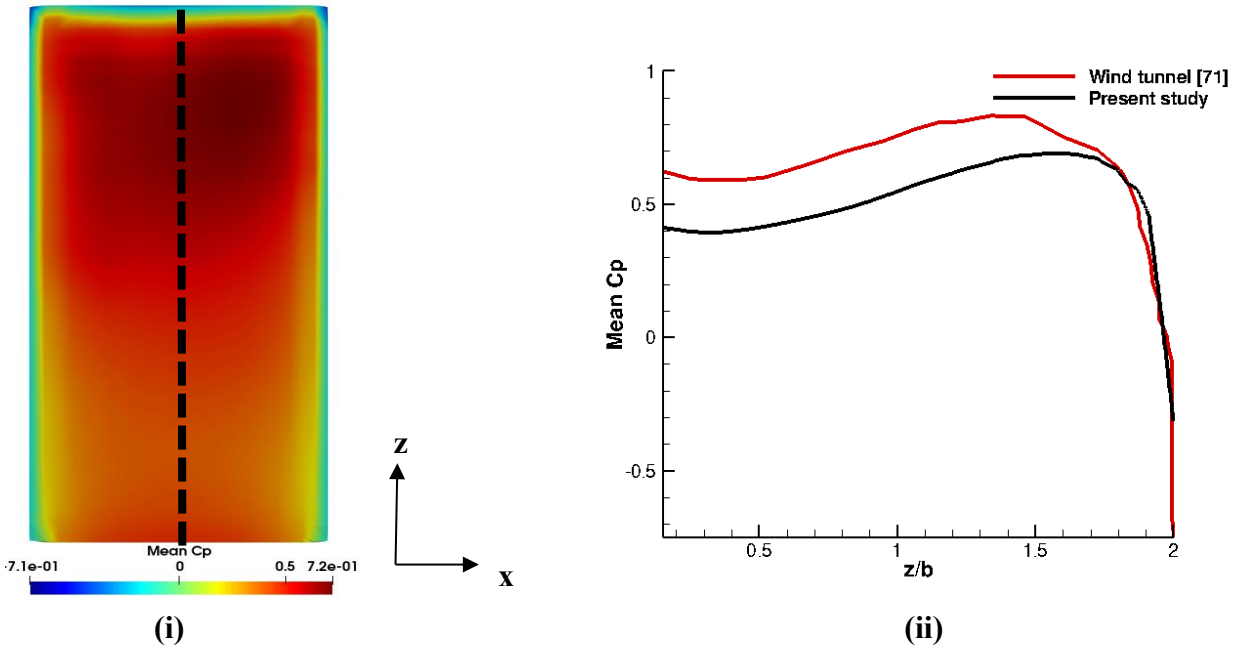

Figure 5.15: Mean pressure coefficient ($\overline{\overline{C_p}}$) at x/b = 0 and y/b = 0.5 for the windward wall of the tall building. (i) Contours of $\overline{C_p}$ (ii) Vertical distribution of $\overline{C_p}$ along the building height

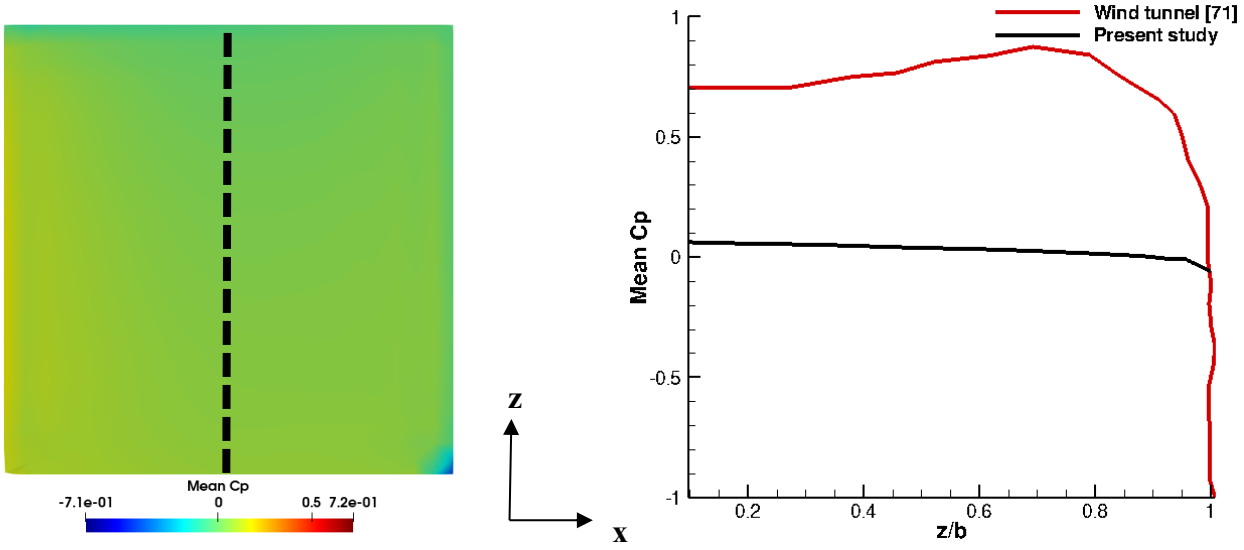

(i) **(ii)**

Figure 5.16: Mean pressure coefficient ($\overline{C_p}$) at x/b = 2 and y/b = 0.5 for the windward wall of the small building. (i) Contours of $\overline{C_p}$ (ii) Vertical distribution of $\overline{C_p}$ along the building height

5.8.2 Numerical Results of Mean Pressure Coefficients for the Small Building Upstream Case

Also, the mean pressure coefficients ($\overline{C_p}$) on the windward faces of the tall building (at x/b = 2 and y/b = 0.5), and small building (x/b = 0, y/b = 0.5) is also investigated for the small building upstream case. The mean pressure coefficients of the windward faces of the tall and small buildings are presented in Figure 5.17 and 5.18 respectively. The mean pressure coefficients showing the small building downstream is compared in this study with when the small building is placed upstream.

The contours of $\overline{C_p}$ and vertical distribution of $\overline{C_p}$ along the building height for the windward wall of the tall building and small building upstream are also depicted in Figures 5.17 and 5.18 respectively.

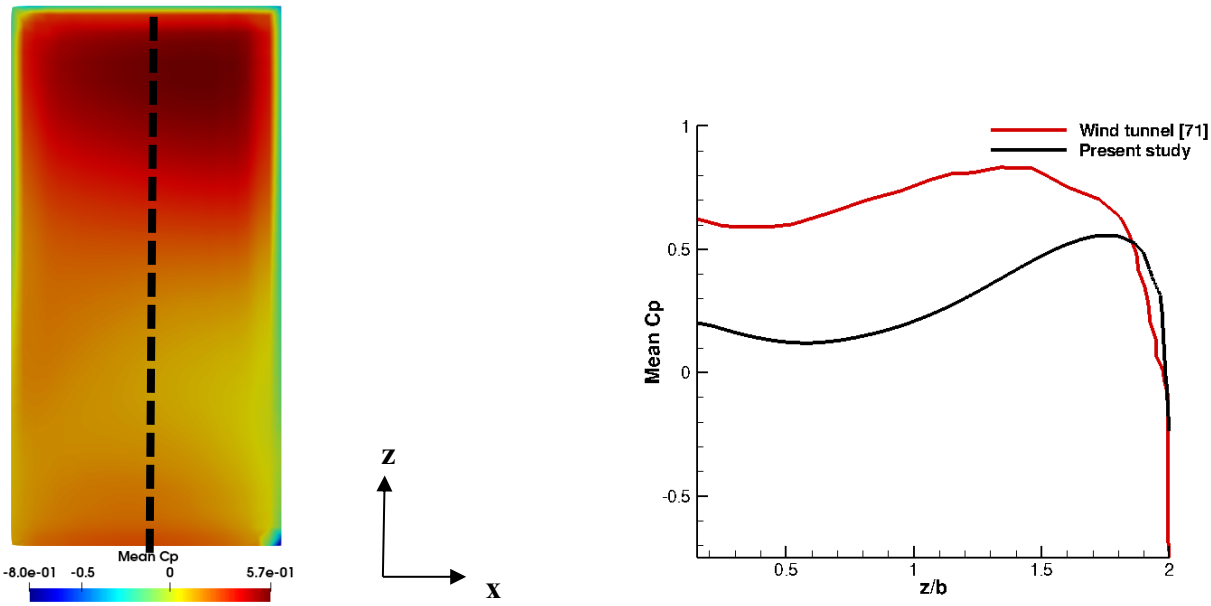

(i) **(ii)**

Figure 5.17: Mean pressure coefficient ($\overline{C_p}$) at x/b = 2 and y/b = 0.5 for the windward wall of the tall building. (i) Contours of $\overline{C_p}$ (ii) Vertical distribution of $\overline{C_p}$ along the building height

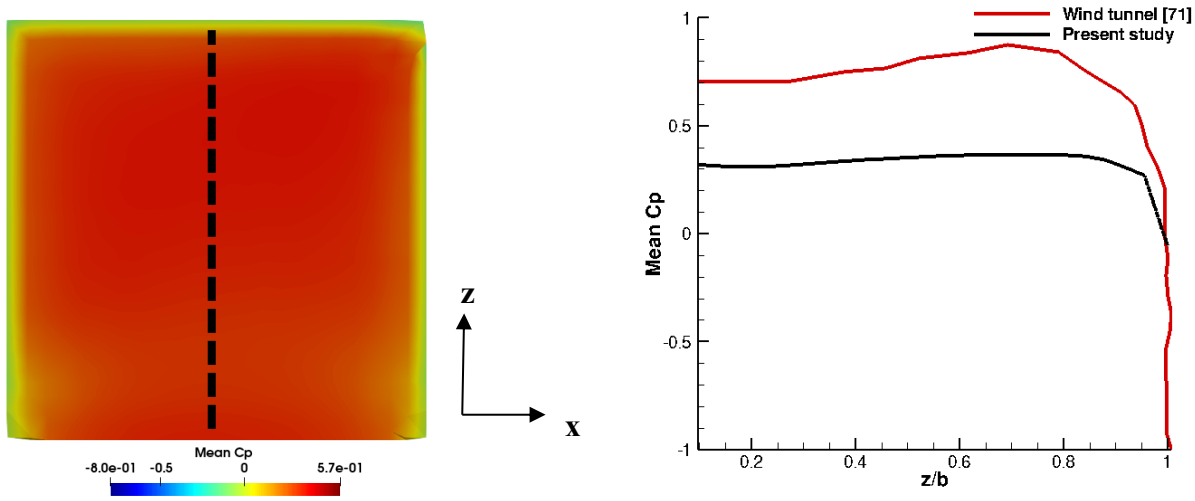

(i) **(ii)**

Figure 5.18: Mean pressure coefficient ($\overline{C_p}$) at x/b = 0 and y/b = 0.5 for the windward wall of the small building. (i) Contours of $\overline{C_p}$ (ii) Vertical distribution of $\overline{C_p}$ along the building height

As seen from Figure 5.17 above, the mean pressure coefficient, $\overline{C_p}$ of the tall building for the windward wall is similar with that from the small building downstream case in Figure 5.15. At the windward face of the tall building, the mean pressure coefficient decreases before increasing close to the ground, and then decreases slowly till it reaches the tip of the building. In addition, the mean pressure coefficient at the windward face of the small building upstream in Figure 5.18 is high at the tip ($\overline{C_p} \approx 0.31$), when compared with that of the tall building ($\overline{C_p} \approx 0.2$). This shows how the small building upstream provide a shielding effect to wind flow around the tall building causing a drop (35.5%) in pressure coefficient around the walls of the tall building as opposed to the small building downstream case. The change in $\overline{C_p}$ on the front or windward wall of the tall building downstream is caused by the wake formed behind the first building (small building upstream), in which the oscillation variations of velocity occur. In Figure 5.18, the discrepancy between the wind tunnel and numerical simulation results is a 55.7% decrease and much lower when compared with the small building downstream case. The mean pressure coefficients are much higher and closer to the wind tunnel results than the small building downstream case, because sheltering effects are not present upstream of the small building to cause an influence on wind flow.

The changing pressure load influences the tall building downstream, according to the study of unsteady flow. It necessitates the analysis of the load structure during the building design process. The dynamic response of the separating and reattaching flow, which periodically rolls up into the vortex, is thought to be the cause these high loads.

5.9 Conclusion

The influence that building neighbors have on wind flow around a tall building is investigated using large eddy simulation. The building neighbors considered are small buildings of the same size placed downstream and upstream of the tall building to study the influence of building neighbors on the tall building. There was significant variation in the wake topology when the building was present behind (downstream) and front (upstream) of the tall building. First, when the small building was placed downstream of the tall building, the downwash effects were much weaker at the wake region than when the single tall building was considered. This shows how the presence of building neighbors downstream or in the wake region of the tall building reduces the wake/turbulence effects from the tall building when the small building was in proximity of it. The small building provided shielding effects to wind flow from the tall building. Therefore,

pedestrians would experience comfort closer to the tall building. The windward wall of the small building suppressed the wake effects from the tall building. When the small building was is in front of the tall building, the downwash flow was much weaker than the small building downstream case, because the small building upstream provided an opposition to wind flow before it interacted with the walls of the tall building. The upwash flow resulted due to base vortices from the ground surface. Flow structures are more present when the small building was downstream than when upstream but the effects of vortex shedding further downstream is much minimal when the small building was downstream of the tall building.

Mean pressure coefficients on the windward walls of the tall and small buildings revealed that when the small building was placed downstream, the windward face of the small building which is in the region of the aerodynamic wake of the tall building gave rise to a decrement (82.5%) in the mean pressure coefficient (from $\overline{C_p} \approx 0.4$ to $\overline{C_p} \approx 0.07$). The presence of the tall building upstream led to this high decrement in mean pressure coefficient. Thus, the gradual decrease of mean pressure coefficient indicated how mean wind load decreases downstream due to the presence of the small building and the aerodynamic wake effects also dampened much quickly than when only a single tall building was present. Due to the wind sheltering effects of the tall building, which impacted the direction of wind flow, the mean pressure coefficient for the small building was substantially lower (88.6% lower) when compared with the wind tunnel results.

Wind flow surrounding the tall structure was shielded by the small building upstream, resulting in a minimal drop in mean pressure coefficient around the tall building's walls. This shows how the mean pressure coefficient at the tip, from the windward walls of the small building to the windward walls of the tall building decreased by about 35.5% (0.31 to 0.2). The decrease in mean pressure coefficient was much lower when compared with the small building downstream case. The effects of building neighbors therefore reduce surface pressure coefficients on the tall building. The presence of the small building upstream minimally reduced turbulence effects around the tall building. Because there were no shielding effects upstream of the small structure to influence the wind flow, the mean pressure coefficients were substantially higher and closer to the wind tunnel results than the small building downstream case.

Chapter 6

CONCLUSION

The influence of building neighbors on wind flow around a tall building using large eddy simulation has been investigated in this thesis in detail. Numerical results obtained from a single tall building were validated with wind tunnel results and it involves gaining an understanding of the wake flow structures and wind flow fields around the tall building. The main objective deals with studying the effects building neighbors have on wind flow around a tall building by analyzing pressure and velocity distribution, the wake topology and evolution, vortical structures, and mean pressure coefficients on the building walls. This provides knowledge of how wake effects change when another building of a small size is present behind and in front of a tall building.

For the twin-building layout (small building present downstream and upstream of a tall building), downwash and upwash flows were observed and demonstrated to be caused by the tip and base vortices. For the single tall building, flow is forced closer to the wall by the increasing downwash strength because of the significant change in upwash. The downwash has a penetration of 0.08 m along the height of the building. With respect to the downwash flows, the single tall building had the strongest downwash compared to when the building neighbors were introduced around the tall building. Therefore, downwash flow effects at the wake were weaker when building neighbors surrounded the tall building. Furthermore, the "Reverse-C" type of vortices was formed which transforms to the "Hairpin" type of vortices in the farther downstream region due to turbulence generated by interactions between the upwash, downwash, and shear layer which cause an increase in wake instabilities. The plane is also dominated by mean streamwise base vortices. The horseshoe vortex's legs extend into the wake, interacting with the wake structure formed behind the building. This has an immediate effect on the wake dynamics. Larger streamline curvatures can be produced by higher magnitudes of spanwise vorticity components in the building's wake zone further downstream. This adds to the evidence of stronger entrainment in the wake of the building. When the separated flow from the leading edge impacts with the wake structures, flow

entrainment occurs. Vortex shedding is asymmetric at all spanwise positions, except near the building's tip, due to the separated shear layers.

The presence of the small building downstream of the tall building reduced wake effects associated with the tall building, thereby giving rise to a much weaker downwash flow at the wake. This reduced turbulence effects coming from the wake of the tall building and created a laminar flow further downstream giving rise to base vortices due to ground effects. Pressure distributions around the two buildings were consistent with the pressure distribution of the single tall building. The presence of an adjacent shorter building downstream of the taller building reduced the pressure in the wake of the taller building and thus a negative pressure was formed at the pedestrian/ground level. Furthermore, the strength of vorticity as evident from the downwash flow originating from the tall building was much weaker than in the single tall building case due to the presence of the small building downstream of the tall building. The flow is unsteady at the interface between the two buildings and in the wake of the small building, but this unsteadiness, characterized by chaotic structures reduces further downstream of the small building. The mean pressure coefficient decreased even more at the windward face of the small building, which is in the aerodynamic wake of the tall building, reaching $\overline{C_p} \approx 0.07$. The progressive decrease in mean pressure coefficient demonstrates how mean wind load drops downstream due to the existence of the small building, and aerodynamic wake effects weaken much more quickly. The mean pressure coefficient for the small building was significantly lower (88.6% lower) than the wind tunnel results due to the wind sheltering effects of the tall building which influenced the direction of wind flow.

The presence of the small building upstream of the tall building created a shielding effect and reduced undesirable wind flow turbulence effects associated with the tall building. The upwash flow collided with the downwash flow along the x-axis, but this was much stronger than the small building downstream case. When the small building was downstream of the tall building, the significant turbulence effect generated was essentially a strong upwash flow. The small building upstream proved insufficient to attenuate the significant turbulent flow in the leeward direction of the tall building. From the trailing edge of the small building to the leading edge of the tall building, the flow is better organised and not perfectly symmetrically distributed due to the transient nature of the flow. A strong recirculation zone was formed due to the suppressing effects of flow separation from the small building. For pedestrians on the ground level, this zone provides

unfavourable wind conditions at this region (i.e., interface between the small and tall building). The strength of vortex shedding is substantially weaker on the small building's windward face, resulting in a decrease in mean streamwise velocity on the tall building's windward face. In contrast, when the small building was placed downstream of the tall building, this was not the case. At the interface between the two buildings, the mean streamwise velocity reduces due to interference effects of the windward walls of the small building. The small building upstream created a shielding effect to wind flow towards the tall building, resulting in a minimal drop (35.5%) in the pressure coefficient around the tall building's walls. The wake generated behind the first building (small building upstream) causes the change in $\overline{C_p}$ on the front wall of the tall building downstream. The mean pressure coefficients were significantly higher and closer to the wind tunnel results when compared with the small building downstream case, because there were no shielding effects upstream of the small building to influence wind flow.

6.1 Future Work

The results obtained from this research showed a small building placed behind and front of the tall building would have a different effect on wind flow around the tall building. More simulations need to be performed for a longer time to achieve a better understanding of the unsteady wake dynamics by determining velocity fluctuations at 10 or more locations in the wake when the small building is downstream and upstream of the tall building to capture the dominant frequencies associated with the horseshoe, hairpin-like vortex structures, and typical arc type structure formed behind the buildings. In addition, more simulations and research are needed to study the impact of changing the distance between the tall and small buildings to determine the optimal building separation that will allow for the avoidance of dangerous wind loads for pedestrians. The influence of trees and building neighbors can be further studied by placing two small buildings downstream and upstream of a tall building to study the effects of wind flow that two building neighbors (small buildings) would have on a tall building when they both surround it.

Bibliography

[1] X. Zhou, G. Zu, M. Gu, and J. Hu, "LES and wind tunnel test on friction velocity on roof surfaces," *Cold Reg. Sci. Technol.*, vol. 151, no. January, pp. 109–118, 2018, doi: 10.1016/j.coldregions.2018.03.005.

[2] B. Blocken and J. Carmeliet, "Pedestrian wind environment around buildings: Literature review and practical examples," *J. Therm. Envel. ad Build. Sci.*, vol. 28, no. 107, 2004.

[3] M. Morrison, T. Brown, and Z. Liu, "Comparison of field and full-scale laboratory peak pressures at the IBHS research center," *Adv. Hurric. Eng.*, pp. 1109–1124, 2012, [Online]. Available: http://dx.doi.org/10.1061/9780784412626.097.

[4] B. Baskaran, B. Murty, and J. Wu, "Calculating roof membrane deformation under simulated moderate wind uplift pressures," *Eng. Struct.*, vol. 31, no. 3, pp. 642–650, 2009, [Online]. Available: http://dx.doi.org/10.1016/j.engstruct.2008.10.013.

[5] T. Stathopoulos, "Wind loads on low-rise buildings: a review of the state of the art," *Eng. Struct.*, vol. 6, no. 2, pp. 119–135, 1984, [Online]. Available: http://dx.doi.org/10.1016/0141-0296(84)90005-1.

[6] A. . Davenport, "What makes a structure wind sensitive?," in *The Jubileum Conference on Wind Effects on Buildings and Structures*, 1998, pp. 1–14.

[7] M. Sutherland and J. Etele, "Urban wind field generation using LES for application to quadrotor flight," *29th Congr. Int. Counc. Aeronaut. Sci. ICAS 2014*, no. May, 2014.

[8] A. . Penwarden, "Acceptable wind speeds in towns," *Build. Sci.*, vol. 8, no. 259, 1973.

[9] M. Tutar and G. Oguz, "Large eddy simulation of wind flow around parallel buildings with varying configurations," *Fluid Dyn. Res.*, vol. 31, no. 5–6, pp. 289–315, 2002, doi: 10.1016/S0169-5983(02)00127-2.

[10] T. Tamura, "Towards practical use of LES in wind engineering," *J. Wind Eng. Ind. Aerodyn.*, pp. 1451–1471, 2008.

[11] J. Halitsky, “Gas diffusion near buildings,” *Meteorol. At. Energy*, p. 221, 1968.

[12] A. Hunt, “Scale effects on wind tunnel measurements of wind effects on prismatic buildings,” Cranfield Institute of Technology, 1981.

[13] M. . Nancoo, “A status report on low level turbulence and wind shear effects on aircraft,” vol. 35, no. 211, 1974.

[14] M. Tsuchiya, S. Murakami, A. Mochida, K. Kondo, and Y. Ishida, “Development of a new k-ε model for flow and pressure fields around bluff body,” *J. Wind Eng. Ind. Aerodyn.*, vol. 67–68, pp. 169–182, 1997, doi: 10.1016/S0167-6105(97)00071-8.

[15] P. Mendis, T. Ngo, N. Haritos, A. Hira, B. Samali, and J. Cheung, “Wind loading on tall buildings,” *Electron. J. Struct. Eng.*, vol. 7, pp. 41–54, 2007.

[16] M. Thordal-Christensen and C. G. Jorgensen, “Method on wind load investigation of high-rise buildings,” 2015.

[17] M. A. Mohamed and D. H. Wood, “Computational modeling of wind flow over the University of Calgary campus,” *Wind Eng.*, vol. 40, no. 3, pp. 228–249, 2016, doi: 10.1177/0309524X16642082.

[18] M. Ozdogan, B. Sungur, L. Namli, and A. Durmus, “Comparative study of turbulent flow around a bluff body by using two- and three-dimensional CFD,” *Wind Struct. An Int. J.*, vol. 25, no. 6, pp. 537–549, 2017, doi: 10.12989/was.2017.25.6.537.

[19] F. . White and I. Corfield, *Viscous fluid flow*. New York: McGraw-Hill, 1991.

[20] A. Kuethe, C. Chow, A. Vought, and B. . Helicopters, *Foundations of Aerodynmaics: Basics of Aerodynamic Design*, Fifth edit. John Wiley & Sons, Inc, 1998.

[21] H. F. Wang, Y. Zhou, C. K. Chan, and K. S. Lam, “Effect of initial conditions on interaction between a boundary layer and a wall-mounted finite-length-cylinder wake,” *Phys. Fluids*, vol. 18, no. 6, 2006, doi: 10.1063/1.2212329.

[22] J. C. R. Hunt, a a Wray, and P. Moin, “Eddies, streams, and convergence zones in turbulent flows,” *Cent. Turbul. Res. Proc. Summer Progr.*, no. 1970, pp. 193–208, 1988.

[23] S. Taneda, “An experimental study on the structure of the vortex street behind a circular

cylinder of finite length," 1952.

[24] H. Wang *et al.*, "Flow structure around a finite-length square prism," *15th Australas. Fluid Mech. Conf.*, no. March 2015, pp. 1–4, 2004, [Online]. Available: https://www.researchgate.net/publication/237307611.

[25] H. F. Wang and Y. Zhou, "The finite-length square cylinder near wake," *J. Fluid Mech.*, vol. 638, no. November, pp. 453–490, 2009, doi: 10.1017/S0022112009990693.

[26] M. R. Rastan, A. Sohankar, and M. M. Alam, "Low-Reynolds-number flow around a wall-mounted square cylinder: Flow structures and onset of vortex shedding," *Phys. Fluids*, vol. 29, no. 10, 2017, doi: 10.1063/1.4989745.

[27] A. Zargar, "Characterization of the wake of large depth - ratio cylinders at low," 2020.

[28] B. Wang, S. Sun, and M. Duan, "Impact of building form on the wake flow wind potential," *Energy Procedia*, vol. 153, pp. 383–388, 2018, doi: 10.1016/j.egypro.2018.10.070.

[29] R. Britter and S. Hanna, "Flow and Dispersion in Urban Areas," *Annu. Rev. Fluid Mech.*, vol. 35, no. 1, pp. 469–496, 2003.

[30] M. Bottema, "Urban roughness modelling in relation to pollutant dispersion," vol. 31, no. 18, pp. 3059–3075, 1997.

[31] B. Yan, "CFD modelling of atmospheric boundary layer flow and wind effects on high rise structures and tall buildings," City University of Hong Kong, 2014.

[32] W. Frank and H. Mauch, "Large-eddy-simulation of the flow around building models," *J. Wind Eng. Ind. Aerodyn.*, vol. 46–47, no. C, pp. 213–218, 1993, doi: 10.1016/0167-6105(93)90286-W.

[33] Y. Jiang, D. Alexander, H. Jenkins, R. Arthur, and Q. Chen, "Natural ventilation in buildings: Measurement in a wind tunnel and numerical simulation with large-eddy simulation," *J. Wind Eng. Ind. Aerodyn.*, vol. 91, no. 3, pp. 331–353, 2003, doi: 10.1016/S0167-6105(02)00380-X.

[34] A. Sohankar, "Flow over a bluff body from moderate to high Reynolds numbers using

large eddy simulation," *Comput. Fluids*, vol. 35, no. 10, pp. 1154–1168, 2006, doi: 10.1016/j.compfluid.2005.05.007.

[35] Y. H. Tseng, C. Meneveau, and M. B. Parlange, "Modeling flow around bluff bodies and predicting urban dispersion using large eddy simulation," *Environ. Sci. Technol.*, vol. 40, no. 8, pp. 2653–2662, 2006, doi: 10.1021/es051708m.

[36] O. Penttinen, "A pimpleFoam tutorial for channel flow, with respect to different LES models.," *Change*, pp. 1–23, 2011.

[37] T. Kono and T. Kogaki, "Numerical investigation of wind conditions over a rectangular prism-shaped building for mounting small wind turbines," *Wind Eng.*, vol. 36, no. 2, pp. 111–122, 2012, doi: 10.1260/0309-524X.36.2.111.

[38] F. Bazdidi-tehrani, A. Ghafouri, and M. Jadidi, "Journal of Wind Engineering Grid resolution assessment in large eddy simulation of dispersion around an isolated cubic building," *Jnl. Wind Eng. Ind. Aerodyn.*, vol. 121, pp. 1–15, 2013, doi: 10.1016/j.jweia.2013.07.003.

[39] W. C. Cheng and F. Porté-Agel, "Evaluation of subgrid-scale models in large-eddy simulation of flow past a two-dimensional block," *Int. J. Heat Fluid Flow*, vol. 44, pp. 301–311, 2013, doi: 10.1016/j.ijheatfluidflow.2013.06.007.

[40] P. Gousseau, B. Blocken, and G. J. F. Van Heijst, "Quality assessment of Large-Eddy Simulation of wind flow around a high-rise building: Validation and solution verification," *Comput. Fluids*, vol. 79, pp. 120–133, 2013, doi: 10.1016/j.compfluid.2013.03.006.

[41] D. Joseph, H. To, D. Hensel, and R. Sheikhi, "Large Eddy Simulation of Turbulent Flow Past a Bluff Body using OpenFOAM," no. August, 2014.

[42] Z. T. Ai and C. M. Mak, "Large-eddy Simulation of flow and dispersion around an isolated building: Analysis of influencing factors," *Comput. Fluids*, vol. 118, pp. 89–100, 2015, doi: 10.1016/j.compfluid.2015.06.006.

[43] T. Okaze *et al.*, "Large-eddy simulation of flow around buildings: Validation and sensitivity analysis," *9th Asia Pacific Conf. Wind Eng. APCWE 2017*, no. December, pp.

3–6, 2017.

[44] M. Ricci, L. Patruno, I. Kalkman, S. de Miranda, and B. Blocken, “Towards LES as a design tool: Wind loads assessment on a high-rise building,” *J. Wind Eng. Ind. Aerodyn.*, vol. 180, no. 2018, pp. 1–18, 2018, doi: 10.1016/j.jweia.2018.07.009.

[45] A. K. Dagnew, G. T. Bitsuamalk, and R. Merrick, “Computational evaluation of wind pressures on tall buildings,” *11th Am. Conf. Wind Eng.*, pp. 1–17, 2009.

[46] R. Gnatowska, “Wind-induced pressure loads on buildings in tandem arrangement in urban environment,” *Environ. Fluid Mech.*, vol. 19, no. 3, pp. 699–718, 2019, doi: 10.1007/s10652-018-9646-0.

[47] J. Gandemer, “Wind Environment Around Buildings: Aerodynamic Concepts.,” in *Proceedings of the Wind Effects on Buildings and Structures*, 1975, no. (SEPTEMBER 8-12, 1975).

[48] H. Ishizaki and I. . Sung, “Influence of adjacent buildings to wind,” in *Proceedings of the Third International Conference on Wind Effects on Buildings and Structures*, 1971, pp. 145–152.

[49] W. H. Melbourne and P. N. Joubert, “Problems of wind flow at the base of tall buildings,” 1971.

[50] B. . Wiren, “A wind tunnel study of wind velocities in passages and through buildings,” in *Proceedings of the Fourth International Conference on Wind Effects on Buildings and Structures*, 1975, pp. 465–475.

[51] T. Stathopoulos and D. Storms, “Wind environmental conditions in passages between buildings,” *J. Wind Eng. Ind. Aerodyn.*, vol. 24, pp. 19–31, 1986.

[52] P. . Bailey and K. C. . Kwok, “Interference excitation of twin tall buildings,” *J. Wind Eng. Ind. Aerodyn.*, vol. 21, pp. 323–338, 1985.

[53] H. Sakamoto and H. Haniu, “Aerodynamic forces acting on two square prisms placed vertically in a turbulent boundary layer,” *J. Wind Eng. Ind. Aerodyn.*, vol. 31, pp. 41–66, 1988.

[54] B. H. . Gowda and M. . Sitheeq, “Interference effects on the wind pressure distribution on prismatic bodies in tandem arrangement,” *Indian J. Technol.*, vol. 31, pp. 485–495, 1993.

[55] Y. Hui, Y. Tamura, A. Yoshida, and H. Kikuchi, “Pressure and flow field investigation of interference effects on external pressures between high-rise buildings.,” *J. Wind Eng. Ind. Aerodyn.*, vol. 115, pp. 150–161, 2013.

[56] D. Alexander, H. Jenkins, and P. Jones, “A comparison of wind tunnel and CFD methods applied to natural ventilation design,” *Proc. Build. Simul.*, pp. 321–326, 1997.

[57] T. Mukha and M. Liefvendahl, “Large-Eddy Simulation of Turbulent Channel Flow,” *J. Soc. Nav. Archit. Japan*, vol. 2015, no. 163, pp. 23–30, 2015, doi: 10.2534/jjasnaoe1968.1988.23.

[58] W. Rodi, “Comparison of LES and RANS calculations of the flow around bluff bodies,” *J. Wind Eng. Ind. Aerodyn.*, vol. 69–71, pp. 55–75, 1997, doi: 10.1016/S0167-6105(97)00147-5.

[59] G. Vita, S. Salvadori, D. A. Misul, and H. Hemida, “Effects of Inflow Condition on RANS and LES Predictions of the Flow around a High-Rise Building,” *Fluids*, vol. 5, no. 4, p. 233, 2020, doi: 10.3390/fluids5040233.

[60] L. Davidson, “Fluid mechanics, turbulent flow and turbulence modeling,” p. 348, 2021.

[61] Y. Meng and K. Hibi, “Turbulent measurements of the flow field around a high-rise building (in Japanese),” *J. Wind Eng.*, vol. 76, pp. 55–64, 1998.

[62] T. A. Adedipe, “Impact of forest types on wind power,” 2018.

[63] U. Guide, “Open ∇ FOAM,” no. June, 2020.

[64] A. K. Roy and P. K. Bhargava, “CFD Modelling of Wind Flow around Buildings for Wind Energy Conversion,” *Natl. Conf. Emerg. trends energy Conserv. Build.*, no. November, pp. 370–379, 2012.

[65] B. Yan and Q. Li, “Large-eddy simulation of wind effects on a super-tall building in urban environment conditions,” *Struct. Infrastruct. Eng.*, vol. 12, no. 6, pp. 765–785, 2016, doi: 10.1080/15732479.2015.1051997.

[66] M. A. Mohamed and D. H. Wood, “Modifications to Reynolds-averaged Navier–Stokes turbulence models for the wind flow over buildings,” *Int. J. Sustain. Energy*, vol. 36, no. 3, pp. 225–241, 2017, doi: 10.1080/14786451.2015.1014903.

[67] G. Lamberti, C. García-Sánchez, J. Sousa, and C. Gorlé, “Optimizing turbulent inflow conditions for large-eddy simulations of the atmospheric boundary layer,” *J. Wind Eng. Ind. Aerodyn.*, vol. 177, no. November 2017, pp. 32–44, 2018, doi: 10.1016/j.jweia.2018.04.004.

[68] M. Grosso, “Wind pressure distribution around buildings: a parametrical model,” *Energy Build.*, vol. 18, no. 2, pp. 101–131, 1992, doi: 10.1016/0378-7788(92)90041-E.

[69] A. Jarza and R. Gnatowska, “Interference of unsteady phenomena in wind flow around bluff-bodies arrangement.,” vol. 27, pp. 721–735, 2006.

[70] D. Zhang, L. Cheng, H. An, and M. Zhao, “Direct numerical simulation of flow around a surface-mounted finite square cylinder at low Reynolds numbers,” *Phys. Fluids*, vol. 29, no. 4, 2017, doi: 10.1063/1.4979479.

[71] N. Holscher and H. . Niemann, “Towards quality assurance for wind tunnel tests: A comparative testing program of the Windtechnologische Gesellschaft,” *J. Wind Eng. Ind. Aerodyn.*, vol. 74, pp. 599–608, 1998.

[72] A. U. Weerasuriya, “Computational Fluid Dynamic (CFD) simulation of flow around tall buildings,” *Eng. J. Inst. Eng. Sri Lanka*, vol. 46, no. 3, p. 43, 2013, doi: 10.4038/engineer.v46i3.6784.